

eman ta zabal zazu



Universidad
del País Vasco

Euskal Herriko
Unibertsitatea

Lia Sotorríos Manrique

Computational Methods Applied to Transition Metal Catalysis and Pericyclic Reactions

Doctoral Thesis supervised by:

Prof. Enrique Gómez-Bengoa

2020

List of publications

Related with this thesis:

- [1] Mora-Radó, H.; Sotorríos, L.; Ball-Jones, M. P.; Bialy, L.; Czechtizky, W.; Méndez, M.; Gómez-Bengoa, E.; Harrity, J. P. A. Synthetic and Mechanistic Investigation of an Oxime Ether Electrocyclization Approach to Heteroaromatic Boronic Acid Derivatives. *Chem. Eur. J.* **2018**, *24*, 9530-9534.
- [2] Sotorríos, L.; Harrity, J. P. A.; Gómez-Bengoa, E. Aromaticity Studies on the Electrocyclization of Imines and Oxime Ethers (Provisional title). *Manuscript in preparation*.
- [3] Carral-Menoyo, A.; Sotorríos, L.; Ortiz-de-Elguea, V.; Diaz-Andrés, A.; Sotomayor, N.; Gómez-Bengoa, E.; Lete, E. Intramolecular Palladium(II)-Catalyzed 6-*endo* C-H Alkenylation Directed by the Remote *N*-Protecting Group. Mechanistic Insight and Application to the Synthesis of Dihydroquinolines. *J. Org. Chem.* **2020**, *85*, 2486-2503.
- [4] Sotorríos, L.; Demertzidou, V. P.; Zografos, A. L.; Gómez-Bengoa, E. DFT Studies on Metal-Catalyzed Cycloisomerization of *Trans*-1,5-enynes to Cyclopropane Sesquiterpenoids. *Org. Biomol. Chem.* **2019**, *17*, 5112-5120.

Not present in this thesis:

- [5] Bernar, I.; Blanco-Ania, D.; Stok, S. J.; Sotorríos, L.; Gómez-Bengoa, E.; Rutjes, F. P. J. T. Synthesis of 3-Amino-1-benzothiophene-1,1-diones by Alkyne Directed Hydroarylation and 1/N \rightarrow 3/C-Sulfonyl Migration. *Eur. J. Org. Chem.* **2018**, 5435-5444.
- [6] Gómez-Palomino, A.; Pérez-Palau, M.; Romea, P.; Urpí, F.; del Olmo, M.; Hesse, T.; Fleckenstein, S.; Gómez-Bengoa, E.; Sotorríos, L.; Font-Bardia, M. Stereoselective Decarboxylative Alkylation of Titanium(IV) Enolates with Diacyl Peroxides. *Org. Lett.* **2020**, *22*, 199-203.
- [7] Sanz-Vidal, A.; Gaviña, D.; Sotorríos, L.; Gómez-Bengoa, E.; López-Ortiz, F.; Sánchez-Roselló, M.; del Pozo, C. Unexpected Metal-Free Synthesis of Trifluoroarenes Via Tandem Coupling of Dicyanoalkenes and Conjugated Fluorinated Sulfinylimines. *Manuscript in preparation*.

List of abbreviations

Abbreviation	Description
ACID (or AICD)	Anisotropy of the induced current density
C-C	Carbon-carbon
CFTR	Cystic fibrosis transmembrane conductance regulator
C-H	Carbon-hydrogen
DFT	Density functional theory
DHQ	Dihydroquinoline
ECP	Effective core potential
GGA	Generalized gradient approximation
GTO	Gaussian-type orbitals
HOMO	Highest occupied molecular orbital
IRC	Intrinsic reaction coordinate
IEFPCM	Integral equation formalism variant of PCM
LC-MS	Liquid chromatography-mass spectrometry
LDA	Local density approximation
LUMO	Lowest unoccupied molecular orbital
NICS	Nucleus-independent chemical shift
NLMO	Natural localized molecular orbital
NMR	Nuclear magnetic resonance
PCM	Polarized continuum model
PES	Potential energy surface
STAT	Signal transducer and activator of transcription
STO	Slater-type orbitals
TS	Transition state
TST	Transition state theory

Abstract

Computational chemistry is an essential tool for the study of chemical reactions. Using the power of computers, we are able to apply theoretical models to chemical systems increasingly complex. By means of computational tools, the properties of molecules can be analyzed and their reactivity can be comprehended.

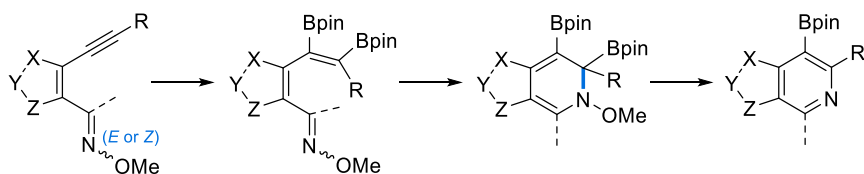
In the present thesis one of the most popular computational methods has been employed; Density Functional Theory (DFT). This method is suitable for the simulation of systems containing *ca.* 100 atoms and is thus widely applied to the study of organic and organometallic reactions. Through the optimization of the geometry and calculation of the energy of substrates, intermediates, products and transition states, the mechanisms of diverse chemical reactions can be investigated.

The synergy between experimental and computational chemists is key to achieve a good understanding of chemical systems. This thesis is based on collaborations with three different experimental research groups. The aim of the performed calculations is to rationalize the results obtained in the laboratory. The examined reactions range from purely organic reactions, such as an apparently simple pericyclic reaction, to complex cycloisomerizations catalyzed by metal complexes.

The thesis has been divided in five chapters. The first chapter introduces the topic of density functional theory and describes the principles and methodology applied during the following chapters. The successive chapters correspond to each of the conducted investigations; the objectives and state of the art are introduced and the results are exposed and discussed.

Chapter 2

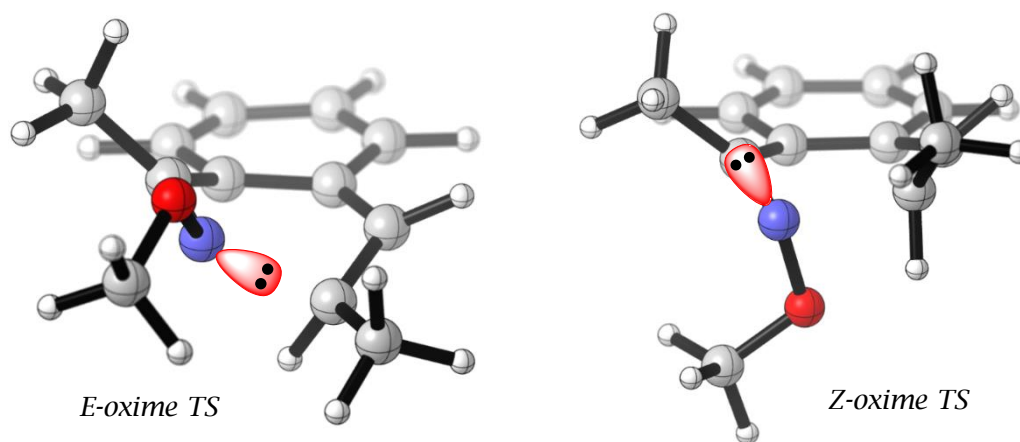
This chapter is based on a collaboration with the group of Prof. Joseph Harrity, from the University of Sheffield and the department of Integrated Drug Discovery at Sanofi-Aventis Deutschland GmbH, Frankfurt. They carried out some cascade reactions for the synthesis of isoquinolines and azole-fused pyridines. The reaction consisted on the platinum-catalyzed diboration of an alkyne, followed by a 6π -electrocyclization to provide the desired products after an elimination step.



The results relied heavily on the configuration of the starting oxime ether. *E*-oximes achieved the desired output, while *Z*-oximes provided exclusively the diboration product, as they were inert to the electrocyclization

In view of these results, a computational study was carried out in order to rationalize the divergent reactivity of oxime ethers. Transition states were computed and activation barriers of *ca.* 60 kcal/mol were found in the case of *Z*-oximes. Although *E*-oximes provided feasible activation barriers, of around 30 kcal/mol, the structural features of *E* and *Z*-transition states showed no significant differences at first sight.

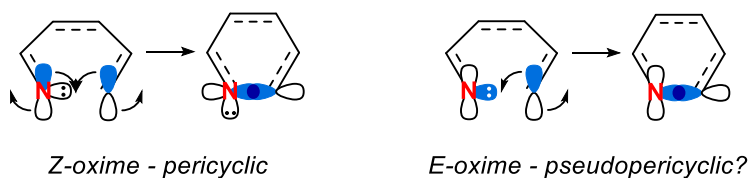
After plotting the electrostatic potential map of each transition state, the next hypothesis is presented. The mechanism of the *Z*-oximes corresponds to that of a pericyclic reaction, as the new σ bond is generated by the constructive overlap of two π -orbitals. On the other hand, *E*-oximes undergo a different mechanism, as the lone pair of the nitrogen atoms seems to be embedded in the new σ bond and is therefore actively participating in the reaction.



Chapter 3

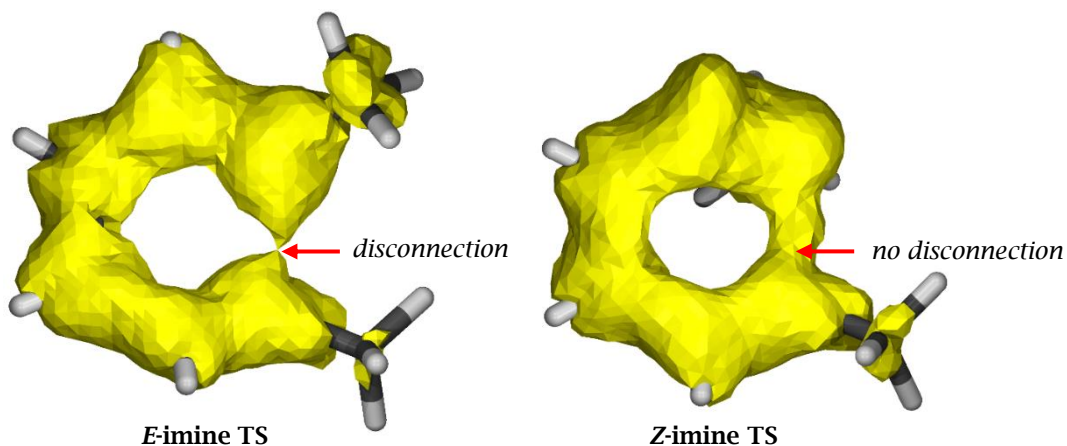
This chapter further analyzes the key role of the lone pair of the nitrogen in the reactivity of *E*-oxime ethers. Simple models of oximes and imines were built and the participation of the lone pair was assessed by computing the Natural Localized Molecular Orbitals (NLMO). The results demonstrated that, in the case of *E*-imines and oximes, the lone pair was partially delocalized on the carbon opposing the nitrogen, while *Z*-imines and oximes were barely delocalized. What is more, the little delocalization that could be detected was centered on the atoms adjacent to the nitrogen.

Once the key role of the lone pair had been assessed, the possibility of the reaction being pseudopericyclic instead of pericyclic was considered. In pseudopericyclic reactions, at least one of the participating orbitals is orthogonal to the π -system. Because of this, the delocalized electron density due to the π -orbitals is interrupted, causing the transition state to be non-aromatic. Two different techniques were used to investigate this issue.



Nucleus Independent Chemical Shifts (NICS) indexes were calculated in the center of the ring along the reaction coordinate. The results revealed that *Z*-imines and *Z*-oximes follow a mechanism identical to that of a purely pericyclic reaction, as their transition states displayed a strong aromaticity. *E*-imines were much less aromatic, which would favour our hypothesis of a pseudopericyclic mechanism. On the other hand, *E*-oximes showed a mixed behavior.

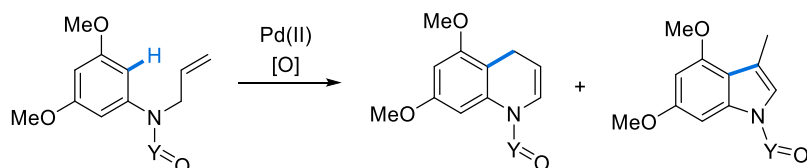
Finally, the software ACID (Anisotropy of the Induced Current Density) was used to observe the delocalized electron density. Besides, a magnetic field perpendicular to the plane of the ring was applied in order to visualize the aromatic ring current of the transition states. The results proved that the delocalized electron density was indeed interrupted in the case of *E*-imines, while *Z*-imines showed no disconnection (vide infra).



This suggests that the mechanism of *E*-imines is pseudopericyclic, while *Z*-imines follow the mechanism of a purely pericyclic reaction. The results for *E*-oximes were not that evident and the reaction was considered pericyclic with a strong pseudopericyclic character.

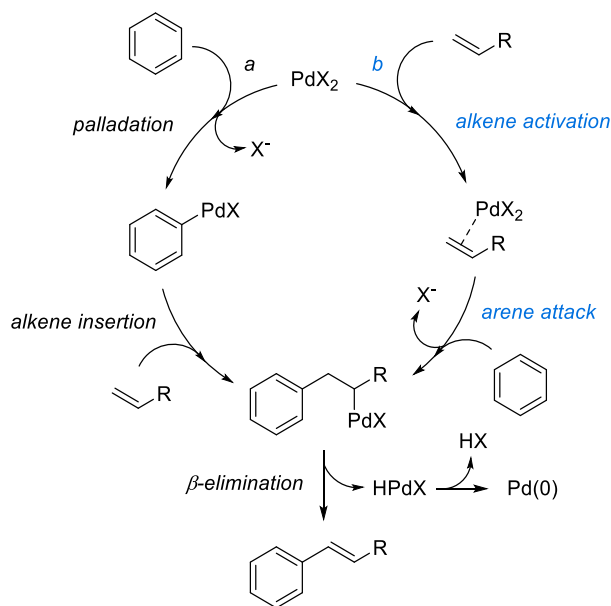
Chapter 4

This chapter is based on a collaboration carried out with the group of Prof. Esther Lete and Prof. Nuria Sotomayor from the University of the Basque Country. They performed a series of intramolecular Fujiwara-Moritani reactions for the synthesis of 1,4-dihydroquinolines. They observed that the reaction relied heavily on the *N*-protecting group of the anilines (Y), as different ratios of the two possible cyclization products were obtained.



The Fujiwara-Moritani reaction consists on the generation of a C-C bond from the C-H bond of an arene and the C-H of an alkene. In this particular case, as the reaction is intramolecular, 6-*endo* and 5-*exo* cyclizations are possible. Besides, two different mechanisms are possible:

The first mechanism consists on a typical C-H activation mechanism (*a*), which involves the palladation of the arene, followed by the insertion of the olefin and final β -elimination that provides the final alkenylated arene. Although it is generally accepted that the reactions proceed through mechanism *a*), the activation of the alkene and consecutive electrophilic aromatic substitution can also occur (*b*). Knowing which of the two mechanism is active during our particular reaction will be key to understand the reactivity.

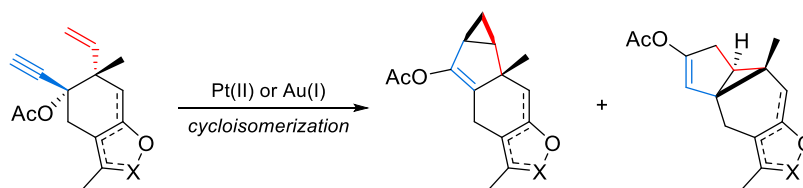


Both mechanisms were studied by means of DFT, optimizing and calculating the energies of intermediates and transition states. The energy profile of mechanism *a*) predicted total selectivity towards the product arisen from a 5-*exo* cyclization, which contradicted the experimental results where total selectivity towards the opposite product was encountered. Mechanism *b*) provided the right selectivity; during the transition state, the coordination between the *N*-protecting group and the palladium atom was observed. This caused a great strain in the 5-*exo* transition state, as a 7-membered ring was

formed, while in the 6-*endo* transition state a stabilizing 6-membered ring was generated. This way, the 6-*endo* product was favored, which concurs with the experiments.

Chapter 5

This final chapter is based on a collaboration with the group of Prof. Alexandros Zografos from the Aristotle University of Thessaloniki. Our collaborators conducted gold and platinum-catalyzed cycloisomerizations of 1,5-enynes for the construction of lindenane-type sesquiterpenoids. However, the formation of a different sesquiterpenoid scaffold was also detected (*vide infra*, product on the right).



The first thing we looked into was the reaction mechanism. The two encounter products arise from the two-step 1,2 or 1,3-migration of the acetate and following cyclization to generate the [3.1.0] bicyclic systems. The resulting Gibbs free energy profile showed feasible activation barriers in the case of both furan and lactone-containing substrates.

With the mechanisms in hand, we tried to explain the isomeric ratios observed in the products. The substrate bearing a furan ring provided the lindenane-type structure in a 3:2 ratio. Rationalizing this result by means of DFT is complicated, as such poor selectivity would correspond to an energy difference of the order of decimals of kcal/mol.

In the beginning, the resulting Gibbs free energy profiles predicted the major formation of the opposite isomer, since the pathway leading to it presented a lower in energy key transition state. A functional screening was performed and, tuning the dielectric constant of the solvent, a model that predicted the right selectivity was achieved.

Substrates bearing a lactone-ring delivered the desired product with total selectivity. Using the aforementioned model, these results could also be simulated with our calculations.

Resumen

En los últimos años, la química computacional se ha convertido en un instrumento fundamental para el estudio de las reacciones químicas. Los avances en el campo de la informática nos permiten aplicar modelos teóricos a sistemas químicos cada vez más complejos. Cuando se trata de explicar qué ocurre en un matraz o en un sistema biológico, los métodos computacionales son de gran ayuda a la hora de entender la reactividad y las propiedades de las moléculas implicadas.

En la presente tesis se ha aplicado una de las teorías más populares dentro de la química computacional; la teoría del funcional de la densidad (DFT). Esta teoría es ideal para el estudio de sistemas que contienen aproximadamente 100 átomos, por lo que es comúnmente utilizada en reacciones tanto orgánicas como organometálicas. Mediante la optimización y cálculo de energías de substratos, intermedios, productos y estados de transición, es posible conocer y profundizar en los mecanismos que gobiernan dichas reacciones.

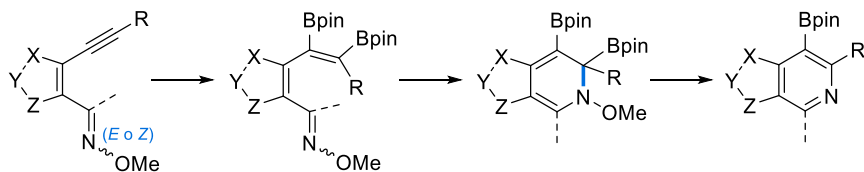
Para poder aplicar los métodos computacionales a sistemas reales, es indispensable la colaboración entre la química computacional y la química experimental. En esta tesis se han llevado a cabo colaboraciones con tres grupos de investigación diferentes con el fin de comprender qué mecanismos son responsables de los resultados obtenidos en el laboratorio. Las reacciones estudiadas son muy diferentes entre sí; desde aparentemente sencillas reacciones pericíclicas puramente orgánicas, hasta complejas ciclaciones catalizadas por metales.

Así, esta tesis se ha dividido en cinco capítulos. El primer capítulo consiste en una introducción en la que se describen brevemente los fundamentos de los conceptos y teorías utilizadas durante el desarrollo del trabajo, así como la metodología aplicada y el software empleado. Los siguientes capítulos se corresponden con cada una de las colaboraciones llevadas a cabo, en los que se comienza introduciendo los objetivos y el estado del arte, para después exponer y discutir los resultados obtenidos mediante métodos computacionales.

Capítulo 2

Este capítulo está basado en una colaboración con el grupo del profesor Joseph Harrity de University of Sheffield (Reino Unido) y el departamento Integrated Drug Discovery de la farmacéutica Sanofi-Aventis Deutschland GmbH, en Frankfurt (Alemania).

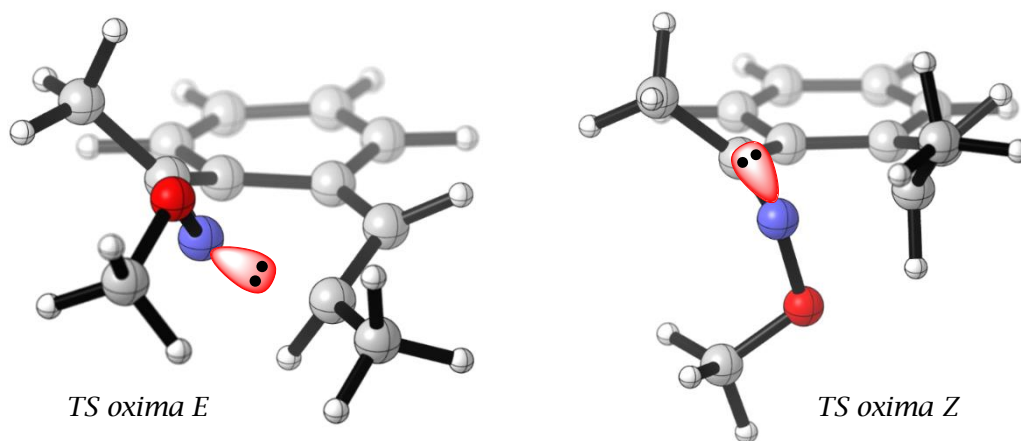
Nuestros colaboradores llevaron a cabo una serie de reacciones cascada para la síntesis de isoquinolinas y azol-piridinas. La reacción consta de tres pasos: una diborilación catalizada por platino, una 6π -electrociclación y finalmente una eliminación para formar el producto aromático (*vide infra*).



Los resultados de la reacción fueron distintos dependiendo de la configuración *E* o *Z* del éter de oxima de partida. Las *E*-oximas produjeron el producto deseado, mientras que las *Z*-oximas rindieron solamente el producto de diborilación, pues resultaron inertes a la reacción de electrociclación.

En vista de estos resultados, realizamos un estudio computacional de la reacción de electrociclación con el fin de explicar la reactividad de los éteres de oxima. Los estados de transición de las oximas *E* y *Z* fueron calculados, y las energías resultantes confirmaron lo observado experimentalmente. Las *Z*-oximas presentaron, en todos los casos analizados, energías de activación extremadamente altas, de hasta 60 kcal/mol. Por otro lado, las *E*-oximas presentaron energías de activación factibles, de alrededor de 30 kcal/mol. Sin embargo, la razón para esta diferencia entre estados de transición no fue obvia a simple vista.

Tras visualizar los mapas de potencial electrostático de ambos estados de transición, presentamos la siguiente hipótesis. El mecanismo de la ciclación de las *Z*-oximas se corresponde con el de una 6π -electrociclación al uso, en la que la interacción constructiva de dos orbitales π forma el nuevo enlace σ . Sin embargo, las *E*-oximas transcurren mediante un mecanismo ligeramente distinto. El par de electrones no compartidos del nitrógeno está embebido en el enlace que se está formando, y de alguna manera contribuye a su formación. Durante el siguiente capítulo, esta interacción será estudiada en profundidad.

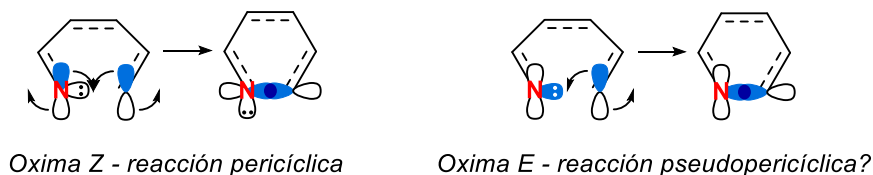


Capítulo 3

Este capítulo continúa profundizando en los estudios realizados en el capítulo que le precede. Con este fin, se propusieron unos modelos de moléculas sencillas con diferentes funcionalidades. Se comienza intentando aclarar el papel del par electrónico no compartido del nitrógeno calculando su parcial deslocalización a lo largo de la molécula.

Para ello, se realizó un análisis de su orbital molecular natural localizado (NLMO). Los resultados mostraron que, en el caso de las *E*-iminas y *E*-oximas, el par electrónico no enlazante se encontraba parcialmente deslocalizado en el carbono con el que se estaba formando el nuevo enlace σ . Por otro lado, cuando las iminas y oximas presentaban configuración *Z*, el par electrónico se encontraba mucho menos deslocalizado. Además, la poca deslocalización detectada estaba situada en los carbonos adyacentes al átomo de nitrógeno.

Una vez confirmado el papel activo del par no compartido, se planteó la posibilidad de que la reacción fuera pseudopericíclica y no un electrociclación al uso. De ser así, el orbital del nitrógeno que se encontraría participando en el estado de transición no sería un orbital π , sino un orbital no enlazante ortogonal al sistema π . En este caso, ese orbital no podría ser otro que el par de electrones no compartidos. De este modo, se observaría una interrupción en la deslocalización de densidad electrónica, lo que conllevaría cierta pérdida de aromaticidad durante el estado de transición. Para comprobar esta hipótesis se utilizaron dos técnicas.



Oxima *Z* - reacción pericíclica

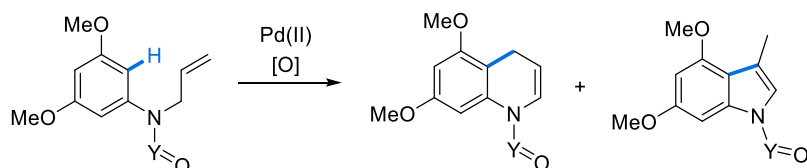
Oxima *E* - reacción pseudopericíclica?

Mediante el cálculo de los índices NICS en el centro del anillo a lo largo de la coordenada de reacción se pudo demostrar que la aromaticidad de las *E*-iminas era distinta a la de las *Z*-iminas. El perfil de la reacción de las iminas *Z* era idéntico a aquel de una reacción completamente pericíclica, en la que en estado de transición presenta una gran aromaticidad, mientras que las *E*-iminas presentaban una aromaticidad mucho menor.

Por último, se utilizó el software ACID para estudiar la densidad electrónica deslocalizada de los estados de transición. Aplicando un campo magnético perpendicular al plano del anillo se pudo también observar la corriente anular. Los resultados demostraron que, en el caso de las *E*-iminas, la densidad se veía interrumpida, mientras que en las iminas con configuración *Z* no presentaban dicha interrupción. Esto indicaría que las iminas *E* transcurren probablemente a través de un mecanismo pseudopericíclico. Los resultados con las oximas no fueron tan claros, por lo que se concluyó que su mecanismo era pericíclico con un fuerte carácter pseudopericíclico.

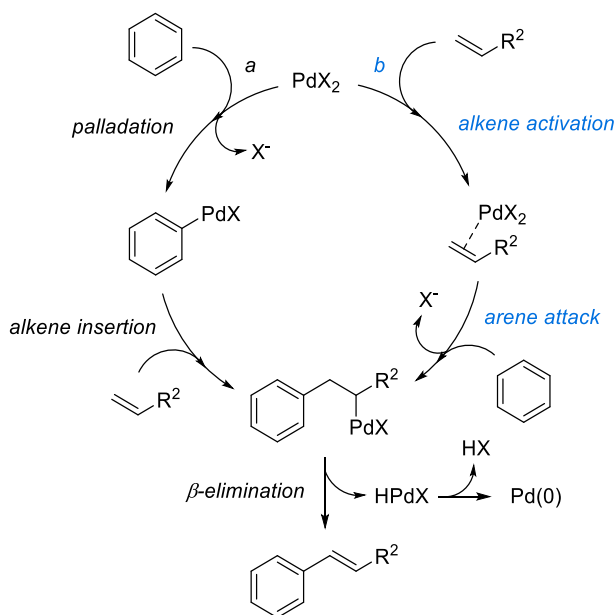
Capítulo 4

Los cálculos llevados a cabo en este capítulo forman parte de la colaboración con un grupo de investigación de esta misma universidad; el grupo de Organometálicos en Síntesis, liderado por Nuria Sotomayor y Esther Lete. En dicho grupo se realizaron una serie de reacciones de Fujiwara-Moritani intramoleculares con el objetivo de sintetizar 1,4-dihidroquinolinas. Nuestros colaboradores observaron que, dependiendo el grupo protector (Y) de la anilina de partida, se obtenían distintos isómeros (*vide infra*).



La reacción de Fujiwara-Moritani utiliza catalizadores de paladio(II) para formar enlaces carbono-carbono utilizando un areno y un alqueno. En este caso, al ser una reacción intramolecular, el producto de la ciclación podrá ser 6-*endo* o 5-*exo*.

Esta reacción puede proceder mediante dos mecanismos. El primero y mayormente aceptado es la paladación del anillo seguido por la inserción del alqueno, para finalmente dar lugar al producto mediante β -eliminación (*a*). Sin embargo, se ha demostrado que en algunos casos el mecanismo se asemeja a la reacción de Friedel-Crafts (*b*), en la que el paladio activa el alqueno para atacar al areno y formar el producto final tras una β -eliminación. Discernir entre ambos mecanismos es esencial para comprender la reacción.

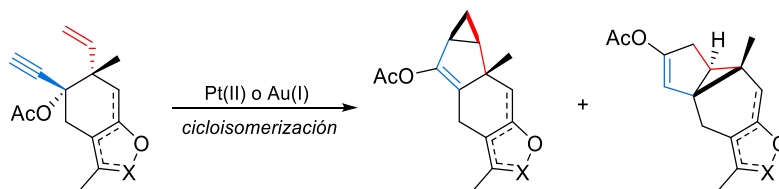


Ambos mecanismos fueron tratados computacionalmente mediante el la optimización y cálculo de la energía libre de Gibbs de los intermedios y estados de transición. Cuando el mecanismo *a*) fue evaluado, nuestros resultados indicaban que el isómero mayoritario debía ser el producto de la reacción 5-*exo*, mientras que los resultados experimentales indicaban lo contrario. Al principio, el mecanismo *b*) proporcionó resultados similares. Sin embargo, modificando los ligandos unidos al paladio, se observó un nuevo enlace de coordinación entre el carbonilo del grupo protector de la anilina y el átomo de paladio. Esto creó una tensión en el caso del estado de transición 5-*exo*, desestabilizándolo, y haciendo por tanto que el producto mayoritario fuera el 6-*endo*, tal y

como indicaban los resultados experimentales. De este modo, se pudo explicar el papel crucial del grupo protector en la reacción.

Capítulo 5

Este capítulo está basado en una colaboración con el grupo de investigación del profesor Alexandros Zografos de Aristotle University of Thessaloniki (Grecia). Nuestros colaboradores llevaron a cabo unas reacciones de cicloisomerización catalizadas por oro y platino. Partiendo de 1,5-eninos, fueron capaces de sintetizar compuestos policíclicos derivados del lindenano, un sesquiterpeno natural (esquema inferior, producto izqdo.). Sin embargo, también se observó la aparición de otro tipo de sesquiterpenoide, producto de una cicloisomerización alternativa (esquema inferior, drcha.).



Utilizando métodos computacionales estudiamos primeramente el mecanismo de la reacción. Este consistió en una primera migración 1,2 o 1,3 del acetato para dar lugar a dos intermedios distintos que posteriormente cicloisomerizan para dar los productos mostrados arriba.

Los resultados variaban según la naturaleza del sustrato de partida y el tipo de catalizador. La reacción con cloruro de oro (I) dio lugar al aleno resultante de la migración 1,3, el cual parecía inerte a la cicloisomerización. El estudio de los perfiles de energía libre de Gibbs de la reacción catalizada no arrojó luz sobre este asunto y, debido a la escasez de reacciones llevadas a cabo con oro, centramos nuestra atención en las reacciones catalizadas por cloruro de platino (II).

Cuando el producto de partida contenía un anillo furano, se obtenían mezclas de ambos productos. Los ratios eran de aproximadamente 3:2 a favor del producto del mecanismo 1,2, lo cual es muy difícil de explicar mediante DFT, ya que una selectividad tan pobre se corresponde con una diferencia de energía del orden de décimas de kcal/mol. Los perfiles energéticos de la reacción parecían indicar el caso contrario, ya que la cicloisomerización del mecanismo 1,3 estaba ligeramente favorecida. Tras realizar un screening de funcionales y variar la constante dieléctrica del disolvente, se encontró un modelo capaz de replicar los resultados experimentales.

Los sustratos tipo lactona produjeron exclusivamente el producto de la migración 1,2 y posterior cicloisomerización. Utilizando el modelo previamente mencionado, se consiguieron simular los resultados también para este sustrato.

Contents

List of publications	i
List of abbreviations	iii
Abstract	v
Resumen	xi
Chapter 1. Introduction and methodology	1
1.1 Computational chemistry.....	3
1.2 Density Functional Theory.....	5
1.2.1 Introduction	5
1.2.2 Density functional theory	5
1.2.3 Jacob's ladder	6
1.2.4 Functionals employed.....	7
1.2.5 The role of the basis set	8
1.2.6 Effective core potential.....	10
1.2.7 Solvent models	10
1.3 Methodology and software	11
1.3.1 DFT calculations with Gaussian.....	11
1.3.2 Molecule editors and visualization tools.....	11
1.3.3 Natural orbitals	12
1.3.4 Aromaticity descriptors	13
1.3.5 Reaction kinetics	16
1.3.6 Curtin-Hammett principle.....	17
1.4 References	19
Chapter 2. Reactivity of <i>E</i> and <i>Z</i> -Oxime Ethers in 6π -Electrocyclization Reactions ..	23
2.1 Context	25
2.1.1 Objective	25
2.1.2 State of the art.....	27
2.1.3 Experimental.....	28

2.2 Computational approach	33
2.2.1 Objective	33
2.2.2 General methods	33
2.3 Results and discussion	35
2.3.1 Mechanism	35
2.3.2 Origin of the selectivity	38
2.4 Conclusions	45
2.5 References	47
Chapter 3. 6π -Electrocyclizations of Oxime Ethers: Mechanistic Insights	49
3.1 Context	51
3.1.1 Introduction	51
3.1.2 Pseudopericyclicity	51
3.1.3 Electrocyclization of allenes and ketenes	52
3.1.4 6π -electrocyclization of nitrogen containing hexatrienes; pericyclic or pseudopericyclic?	54
3.2 Computational approach	57
3.2.1 Objective	57
3.2.2 Computational methods	57
3.3 Results and discussion	61
3.3.1 Preliminary studies	61
3.3.2 NLMO	62
3.3.3 NICS	64
3.3.4 ACID	68
3.4 Conclusions	75
3.5 References	77
Chapter 4. Regioselectivity of a Palladium-Catalyzed Intramolecular Fujiwara-Moritani Reaction	79
4.1 Context	81
4.1.1 Objective	81
4.1.2 State of the art	82
4.1.3 Experimental	84

4.2 Computational approach	89
4.2.1 Objective	89
4.2.2 General methods	89
4.3 Results and discussion	91
4.3.1 Path a. Classic Fujiwara-Moritani mechanism	91
4.3.2 Path b. Friedel-Crafts type mechanism	98
4.3.3 Elimination step	103
4.4 Conclusions	105
4.5 References	107
Chapter 5. Platinum and Gold-Catalyzed cycloisomerization of 1,5-enynes	111
5.1 Context	113
5.1.1 Objective	113
5.1.2 State of the art	115
5.1.3 Experimental	118
5.2 Computational approach	121
5.2.1 Objectives	121
5.2.2 General methods	122
5.3 Results and discussion	123
5.3.1 Mechanism of the reaction	123
5.3.2 Difference between gold and platinum catalysis	134
5.3.3 Path selectivity with platinum	138
5.3.4 Difference between furan and lactone	139
5.3.5 Path selectivity of 1 and 5	142
5.3.6 <i>Syn</i> / <i>anti</i> selectivity	149
5.4 Conclusions	151
5.5 References	153
Appendix	155
ACID figures	155
Publications	156

Chapter 1.

Introduction and methodology

The aim of this chapter is to briefly introduce the main aspects of computational chemistry, focusing on the density functional theory. The basic concepts, theories and principles employed in this thesis will be described, as well as the adopted methodology and software.

1.1 Computational chemistry

Computational chemistry is a branch of chemistry aimed to solve chemically related problem with the aid of computers.¹ Modern computers are able to carry out large amounts of mathematical operations in increasingly shorter times, making them perfect tools for solving the complex mathematical systems originated from the theoretical chemistry field.

The main properties computational chemists can measure and predict are structure, energy and chemical properties.² Given a certain number of atoms, we can study the relative position of each atom and how they are bonded. Calculating the Potential Energy Surface (PES), we can determine which of all the possible atomic arrangements is more probable, as well as predict the reactivity of each structure. Finally, different chemical properties can be assessed, from experimental observables such as spectra (nuclear magnetic resonance, electron paramagnetic resonance, vibrational, etc.) to more conceptual properties, such as aromaticity, bond order, steric behavior and others.

There are different computational methods available to computational chemists: from *ab initio* calculations, based on the Schrödinger's equation, to molecular mechanics, based on classical mechanics. Choosing a suitable model is key to obtain accurate results in a reasonable time span and at an affordable cost. The method chosen to carry out all the calculations in the present thesis was Density Functional Theory (DFT), one of the most widely used models in applied quantum chemistry and perfect for the systems object of this study, consisting of 50-100 atoms.³

1.2 Density Functional Theory

1.2.1 Introduction

The aim of quantum-based computational models is to solve the time-independent Schrödinger equation:⁴

$$\hat{H}\psi = E\psi \quad (1.1)$$

where \hat{H} is the time-independent Hamiltonian operator, ψ is the wave function and E is the total energy of the system. The extreme complexity of the Hamiltonian operator requires the use of approximations, mainly the Born-Oppenheimer approximation.⁵ According to this approximation, the nuclei of a system can be considered static because they are much larger than the electrons.

Even with the use of the Born-Oppenheimer approximation, solving the Schrödinger equation is still too difficult for systems having more than two electrons.⁶ Therefore, further approximations are required to describe complex multi-electronic systems. One of the most popular approaches, and the one discussed in this thesis, is the density functional theory modeling.

1.2.2 Density functional theory

Density Functional Theory (DFT) is a quantum mechanical model based on using the electron density, instead of the wave function, to describe its properties.² The electron density function, $\rho(\vec{r})$, depends only on three spatial coordinates ($r = x, y, z$), while the wave function depends on $3N$ variables, being N the number of electrons. This is the main advantage of DFT; the complexity of the equations is greatly reduced, and with it, the computational cost.

Although first approaches to this theory started in 1927, the foundation was established in 1964 with the Hohenberg-Kohn theorems.⁷ These two theorems state that: *a)* the ground state electronic energy can be calculated as functional of the electron density and *b)* the electron density follows the variational principle, thus the calculated electronic energy must be greater or equal to the true ground state value:

$$E_0 = \underbrace{E[\rho_{exact}]}_a \leq \underbrace{E[\rho]}_b \quad (1.2)$$

This way, we know that the energy of the system can be calculated using the electron density functional (a function of the density function, ρ), although we do not know the form of this functional.

Roughly one year later, Kohn and Sham⁸ realized that the functional would be much simpler if we considered a system with non-interacting electrons. The functional can then be divided into specific components as follows:

$$E[\rho] = T_{ni}[\rho] + V_{ne}[\rho] + V_{ee}[\rho] + \Delta T[\rho] + \Delta V_{ee}[\rho] \quad (1.3)$$

each term referring to: the kinetic energy of the non-interacting electrons $T_{ni}[\rho]$, the potential energies due to nuclear-electron interaction $V_{ne}[\rho]$ and electron-electron repulsion $V_{ee}[\rho]$, the correction to the kinetic energy due to electronic interactions $\Delta T[\rho]$ and the non-classical corrections to the electron-electron repulsion energy $\Delta V_{ee}[\rho]$. This way, the first three terms of the equation, which are not taking into account the electron-electron interaction, can receive a classical treatment (using the electron density as variable). The last two terms can be combined as $E_{xc}[\rho]$ or exchange-correlation energy and are the actual challenge of the DFT model.

1.2.3 Jacob's ladder

The difference between the different DFT functionals lies in the nature of the approximation for the exchange-correlation functional.⁹ These functionals can be ordered according to their approximation method using Jacob's ladder, as illustrated by Perdew and Schmidt.¹⁰ The ladder starts in the Hartree world and climbs up to the "heaven" of chemical accuracy (Figure 1.1).

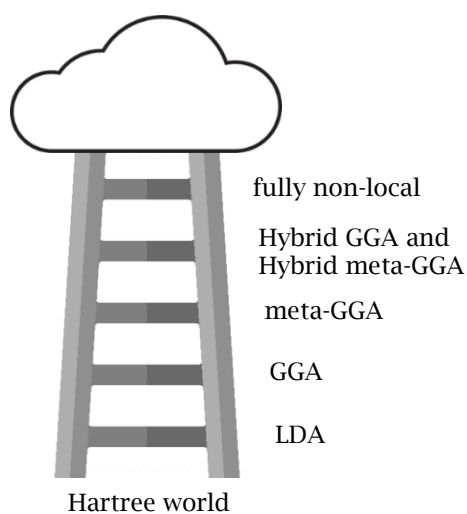


Figure 1.1. Jacob's ladder of density functional theory

The first and most basic developed approximation was the Local Density Approximation (LDA).³ This approximation calculates the energy and properties of the system based exclusively on the electron density, whereas approximations above in the ladder use the gradient of electron density. The second step of the ladder corresponds to Generalized Gradient Approximation (GGA) and is based on the electron density gradient in a given position; hence, it is considered a semi-local approximation. The next step on the ladder consists of meta-GGA methods, which also include the Laplacian (or second derivative) of the density. Higher order approximations (non-local) become much more accurate, but also more complicated and therefore, expensive. Hybrid GGA and hybrid meta-GGA methods include a functional for the exchange (based on the Hartree-Fock exchange), while fully non-local methods add the unoccupied (virtual) orbitals to the functional.

The choice of the functional will affect both the quality of the results and the time spent on the calculations. Next, the functionals used in the present thesis will be introduced.

1.2.4 Functionals employed

Most of the structure optimizations of this thesis have been performed with the hybrid GGA functional B3LYP. This functional, which uses the Becke 88 exchange functional¹¹ and the Lee, Yang and Parr correlation functional,¹² has been for years the most popular DFT functional,¹³ mainly due to his good accuracy/cost ratio.¹⁴ Nevertheless, this functional does not properly describe non-covalent interactions, such as van der Waals interactions, weak hydrogen bonds and π - π stacking interactions. In order to provide a more accurate description of the structures treated in this thesis, a set of dispersion corrected functionals were also employed.

The dispersion corrected hybrid meta-GGA Minnesota functionals developed by Truhlar and coworkers¹⁵ have gained popularity during the last years. The functional M06-2X draws special attention, as it is heavily parametrized and provides excellent results for structures with strong non-covalent interactions.¹⁶ When structures contained metal atoms, the M06 functional (from the same functional family) was employed, as M06-2X is parametrized only for non-metals.

In chapter 5, a functional screening was performed, testing a few more functionals. The ω B97X-D functional developed by Head-Gordon and coworkers¹⁷ was tested, as it includes long-range corrections and Grimme's D2 correction.^{18a} We also tried adding Grimme's D3 dispersion^{18b} to two hybrid functionals: the already mentioned B3LYP and the B3PW91 functional, formed by Becke 88 exchange functional and Perdew and Wang

91¹⁹ correlation functional. Finally, a pure meta-GGA functional, the M11-L functional,²⁰ was also tested.

1.2.5 The role of the basis set

The basis set is a set of mathematical functions used to construct the wave function.² Molecular orbitals (φ_i) are formed by linear combination of these functions (χ_p), usually atomic orbitals, as showed below:

$$\varphi_i = \sum_{p=1}^m C_{ip} \chi_p \quad (1.4)$$

where C_{ip} is a scalar. Theoretically, an optimal representation of the orbitals can be achieved with an infinite number (m) of functions. In practice, this is not possible in actual calculations, and a finite number of functions must be used. The accuracy of the molecular orbital description will depend on the number of functions, but also on the “quality” of the atomic orbitals.

There are two types of atomic orbitals; the Slater-type orbitals (STO) and the Gaussian-type orbitals (GTO). The STO accurately describe the shape of atomic orbitals, but their analytical solution is too complex for large molecules. Therefore, they are exclusively applied to atomic and diatomic systems. On the other hand, GTO are computationally feasible, although fairly less accurate than STO. These GTO can be called primitives, while their linear combination gives place to contracted GTO, having a very similar behavior to STO. Thus, contracted GTO are more commonly used, as they can provide similar results to STO at an affordable computational cost.

The different basis sets can be classified as follows:²

- **Minimum basis set:** The smallest number of possible functions are employed, providing qualitative results. For example, in the case of hydrogen and helium a single s -function would be employed, while second row atoms would contain two s -functions (1S and 2S) and one p -function (2P_x, 2P_y and 2P_z).
- **Extended basis sets:** Two, three or N -functions are used per atomic orbital, making double, triple and N -zeta basis sets. A hydrogen atom with a double zeta basis set uses two s -functions (1S and 1S'), while a triple zeta basis set employs three (1S, 2S' and 1S''). The most commonly used variation of this basis sets are:
 - **Split valence sets:** they use a different number of functions for the core orbitals and the valence orbitals. Since bonds are formed by valence orbitals,

we can reduce the computational cost by using a high number of functions only in the valence orbitals.

- **Polarization functions**: A basis can be augmented with polarization functions, this is, functions with a higher angular momentum than those of occupied orbitals. Without polarization functions, the basis sets are centered on the atom, and thus cannot properly describe systems where electronic charges are altering the shape of the orbitals. With polarization functions, a hydrogen atom would consist not only on s -functions but also on p -functions, more accurately describing the shape of the orbital.
- **Diffuse functions**: These functions allow electrons to move on a more ample space. They are essential for systems with loosely bound electrons, like anions or excited states. The method to add diffuse functions varies depending on the basis set family.

1.2.5.1 Selected basis sets

The basis sets developed by Pople and coworkers are amongst the most used split valence sets, which allow the addition of polarization and diffuse functions. For the optimization of structures, we typically used the 6-31G(d,p) basis set.²¹ Following Pople's notations, this basis sets uses: one contracted GTO formed by six primitive GTO for the core electrons, two contracted GTO (formed by three and one primitive GTO) for the valence atoms, and adds polarization functions to all atoms (p -functions to the hydrogen atoms and d or higher functions to the rest of the atoms).^{21b} It is therefore a double zeta basis set which takes polarization into account.

When final energies where computed, a triple zeta split basis set of the same family was employed; 6-311G(d,p).^{22,23} Polarization functions where employed and, when necessary, diffuse functions where added to non-hydrogen atoms, using the notation '+', forming the basis set 6-311+G(d,p).²⁴

The aforementioned basis sets are not suitable for 5th and 6th row atoms such as Pd, Pt and Au (included in this thesis). For the structure optimization of systems containing these atoms, two different basis sets were used: LANL2DZ²⁵ (developed in Los Alamos National Laboratory) and SDD²⁶ (Stuttgart-Dresden). They are both double zeta basis sets and do not include polarization or diffuse functions. They are also effective core potentials basis sets (see next section).

Final energies of metal containing systems where computed using Def2TZVPP as basis set. Developed by Ahlrichs and coworkers,²⁷ it is a redefined version (Def2) of the triple zeta valence (TZV) basis set which includes many polarization functions (PP).

1.2.6 Effective core potential

Systems containing heavy atoms, such as transition metals, possess a large number of core electrons. Although they are not important in chemical reactivity, an extensive number of basis functions is needed in order to expand the orbitals. Failing to do so will cause a poor estimation of the electron-electron repulsion, and will ultimately affect the description of valence orbitals.²

As firstly proposed by Hellman in 1935,²⁸ the combined nuclear-electronic core can be accurately represented by replacing core electrons with analytical functions, while valence electrons can be treated explicitly. This modelling of the core electrons, known as pseudopotential or Effective Core Potential (ECP), provides good results at a much lower cost than calculations involving all the electrons. Therefore, this methodology was applied to the computation of palladium, gold and platinum atoms (chapters 4 and 5).

1.2.7 Solvent models

During the optimization of the conditions of a reaction, it is crucial to test different solvents, as they have great impact in the reactivity. The polarity of the solvent can, not only enhance the solubility of the reactants, but can also lower the energy barrier of a reaction by, for example, stabilizing the charges present on its transition state. It is therefore essential to have these effects taken into account during the calculations.

In the early years of DFT, the simulations were carried out in vacuum, as the introduction of thousands of molecules of solvent was not feasible with the available computation power. Nowadays, the explicit solvent models can be achieved with the use of molecular mechanics, but DFT calculations generally use an alternative approach.²

DFT calculations usually use implicit solvation models, such as the Polarized Continuum Model (PCM)²⁹ employed in this thesis. In this method, the solute is placed inside a cavity formed by a polarizable uniform medium with a dielectric constant, ϵ . The solvation free energy, ΔG_{solv} , can be calculated as follows:

$$\Delta G_{solv} = \Delta G_{cav} + \Delta G_{disp} + \Delta G_{rep} + \Delta G_{elec} \quad (1.5)$$

where ΔG_{cav} is the energy needed to form the cavity, ΔG_{disp} is the dispersion energy between the solute and the solvent, ΔG_{rep} stands for the repulsive interaction between solute and solvent and finally ΔG_{elec} is the electrostatic term caused by the charge distribution.

1.3 Methodology and software

1.3.1 DFT calculations with Gaussian

The fundamental calculations of the present thesis were carried out using the Gaussian package, originally developed by John Pople. This software can perform a variety of calculations, ranging from molecular mechanics to multi-configurational self-consistent field. The version 09³⁰ of this software was used to perform all the DFT calculations present in this thesis.

The Gaussian software was employed to optimize the geometry of reactants, intermediates and products by locating the structures with minimum potential energies. The Gibbs free energy of the optimized structures was obtained either from the resulting thermodynamics from the calculation of vibrational frequencies or by the addition of potential energies and corrections to the Gibbs free energy (when the optimization was performed on a different theory level than the one used to obtain the final energies).

This same strategy was utilized for the location of transition states and the calculation of their energies. In order to check whether each transition state was connecting the intended intermediates, Intrinsic Reaction Coordinate (IRC) calculations were often performed.

After the vibrational frequencies of intermediates and transition states were computed, the number of imaginary frequencies (negative frequencies) was checked in order to verify that there were none, in the case of reactants, intermediates and products (minimums) and only one in the case of transition states (saddle points).

1.3.2 Molecule editors and visualization tools

- Avogadro:³¹ The initial sketch of the analyzed structures was performed with the free and open-source software Avogadro. The Universal Force Field (UFF)³² was used to approximate the geometry by means of molecular mechanics.
- Molden:³³ The pre and post-processing tool Molden (free for academic purposes) was used for the visualization of most of the output produced by Gaussian, due to the simplicity and rapidness of the program. The optimization processes and frequencies were monitored using this software.

- GaussView:³⁴ This graphical interface included in the Gaussian package was used for the visualization of contours, mainly for obtaining the electrostatic potential surfaces mapped over the total density (chapter 2).
- CYLview:³⁵ This freeware was used to render the figures of three-dimensional structures displayed through the thesis, using the geometries of Gaussian outputs as input. This software uses POV-ray (*vide infra*).
- POV-Ray:³⁶ The ray-tracing program POV-Ray is a freeware tool for creating three-dimensional graphics. Its standalone version was employed for rendering the output generated by the software ACID.

1.3.3 Natural orbitals

Studying the properties of a particular bond can provide interesting information, as the nature of the bond may be key for the reactivity of the molecule. For this, orbitals centered on individual bonds or partially delocalized orbitals can be computed.

To put it simply, we can define atomic orbitals (AO) as mathematical functions that describe the behavior of electrons on an atom, while molecular orbitals (MO) refer to the behavior of electrons in a molecule. While atomic orbitals are completely centered in atoms, canonical molecular orbitals are completely delocalized through the molecule. Considering the algorithmic sequence showed in Figure 1.2, between AO and MO, we find a set of “natural” orbitals: natural atomic orbitals (NAOs), natural hybrid orbitals (NHOs), natural bond orbitals (NBOs) and natural semi-localized orbitals (NLMOs).^{37,38}

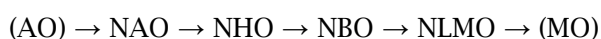


Figure 1.2. Algorithmic sequence of different type of orbitals, adapted from ref. 38.

Natural bond orbitals are localized, as the name suggests, in bonds. With NBOs, we can determine the contribution of each atom to the bond as well as the hybridization (*s*-, *p*-, or *d*-character) of each atom. NLMOs allow the partial delocalization of the NBOs, calculating the electronic density distribution through the rest of the atoms in the molecule. This can be extremely useful to understand the delocalization of each bond through the molecule, for example, in cases with strong conjugation.

In our particular case, we computed a NLMO to observe the delocalization of an NBO formed by the lone pair of a nitrogen atom (chapter 3). This way, we could study how the lone electron pair is distributed along the molecule and its effect on the reactivity.

The concepts and methods for computing NBOs³⁹ and NLMOs⁴⁰ were established by Weinhold and coworkers during the 80s. The software they developed to perform this

calculations is also named NBO,⁴¹ and its 3.1 version available in Gaussian09 was used in the aforementioned study.

1.3.4 Aromaticity descriptors

Aromaticity is a stabilizing effect occurring in conjugated systems whose configuration allows the delocalization of the electrons in the π -system of the molecule. It is difficult to characterize, as there is no individual property that can directly measure aromaticity. It is common to evaluate aromaticity by measuring different descriptors, usually based on the measurement of structural, magnetic, energetic, electronic, and reactivity-based properties.⁴² In this thesis, we focused on descriptors based on magnetic properties.

Aromatic compounds can be characterized by the study of their magnetic properties, such as diamagnetic susceptibility exaltation (Λ^m) or ¹H NMR shifts.⁴³ Λ^m is the difference between the experimentally measured magnetic susceptibility (χ_M) and the estimated magnetic susceptibility (χ_M'), calculated from the atomic and bond susceptibility contributions. Λ^m provides positive values for aromatic compounds, close to zero values for non-aromatic molecules and negative values for antiaromatic compounds.⁴⁴ Nevertheless, this technique has certain drawbacks, such as the dependence on a non-unique reference system and the size of the ring, which complicates the direct comparison of different molecules.⁴³

The chemical shifts observed in ¹H NMR have also been employed as aromaticity criterion. Outer aromatic hydrogens usually appear in the region of 7-9 ppm, a downfield shift from typical alkenes. For molecules big enough to have hydrogens inside the ring, this effect is more dramatic as inner hydrogens can have negative values, as low as -3 ppm in the case of [18]annulene. Nonetheless, this criterion is not absolute, as there are reported cases of non-aromatic compounds presenting similar downfield shifts. For example, pyrrole, furan and cyclopentadiene have very similar proton shifts (Figure 1.3), although cyclopentadiene is not an aromatic compound.⁴⁵

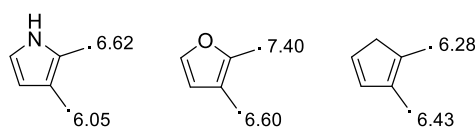


Figure 1.3. ¹H NMR shifts (ppm) of pyrrole, furan and cyclopentadiene, adapted from ref. 45.

The power of computational chemistry can also be applied to the study of aromaticity through magnetic properties. In the following paragraphs, we present two techniques: the nucleus-independent chemical shifts (NICS) and the anisotropy of the

induced current density (AICD or ACID). The data needed for these two methods can be obtained by calculating the NMR shielding tensor with the software Gaussian.

1.3.4.1 Nucleus-independent chemical shift

The nucleus-independent chemical shift (NICS) is an aromaticity measure proposed by Schleyer in 1996.⁴⁶ NICS represents the value of the absolute magnetic shielding computed at an arbitrary point. Originally, this point was the center of the ring, NICS(0). Shortly after, computing NICS at 1 Å above the ring (NICS(1)), where the NICS value usually reaches a maximum, was proposed.⁴⁷

The results of NICS, whose sign is reversed due to NMR convention, fall in three categories. Negative NICS values correspond to aromatic molecules, such as benzene, while antiaromatic molecules, such as cyclooctatetraene, have positive NICS values. Molecules with non-aromatic behavior usually have NICS values close to 0 ppm.

The initially NICS values were based on the total isotropic shielding, this is, on the average of the xx , yy and zz elements of the shielding tensor. Nevertheless, ring currents formed due to the electron delocalization in aromatic molecules are induced when an external magnetic field is applied perpendicular to the plane of the ring (the z direction). With this in mind, Fowler and Steiner⁴⁸ suggested the use of NICS_{zz} , based on the contribution of the out-of-plane component of the tensor. We can therefore refer to the previously described methods as $\text{NICS}(0)_{\text{iso}}$ and $\text{NICS}(1)_{\text{iso}}$, while the new anisotropic indexes are named $\text{NICS}(0)_{zz}$ and $\text{NICS}(1)_{zz}$.⁴⁹

It is worth mentioning that NICS indexes are usually employed in a qualitative manner, as the comparison of rings of different sizes provides poor results in some cases.⁵⁰ In the same way, there is no NICS value above or below which we can state whether a molecule is aromatic or not.

In the chapter 3 of this thesis, $\text{NICS}(0)_{\text{iso}}$ values were computed for the transition state of a set of reactions. These transition states were not completely planar, and therefore the definition of the z axis was a difficult matter. Because of this, the isotropic value of the tensor was employed in order to compare our results with the literature (as explained in the chapter's computational methods section).

1.3.4.2 Anisotropy of the induced current density (ACID)

In 2005, Herges and collaborators developed a method for visualizing the electron delocalization in a three-dimensional way.⁵¹ For this purpose, they computed the anisotropy of the induced current density (ΔT_s) parameter. ΔT_s is a scalar field similar to the

electron density that can be represented as an isosurface, but depends exclusively on the delocalized electrons (instead of electron density as a whole). Using POV-Ray, the isosurface (independent of the direction and magnitude of the external magnetic field) can be displayed (Figure 1.4).

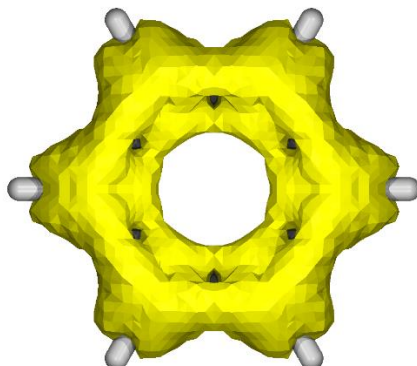
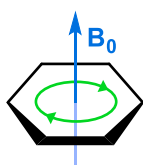


Figure 1.4. ACID isosurface of benzene (isosurface value = 0.05).

In order to classify a molecule as aromatic or antiaromatic, the direction of the current density must also be visualized. Aromatic molecules are associated to diatropic ring



currents, and should follow the “left hand rule” (see left). When a magnetic field perpendicular to the ring is applied in the shown direction, a clockwise pattern will be observed in aromatic molecules, while antiaromatic molecules will display an anticlockwise pattern due to the paratropic ring currents.

In ACID, the current density vectors are plotted onto the isosurface. They are plotted as green arrows with red arrowheads, whose length indicates the absolute value of the current density at the point of origin. Figure 1.5 shows the current density vectors of benzene and, since it is an aromatic molecule, a clockwise pattern is observed through the molecule.

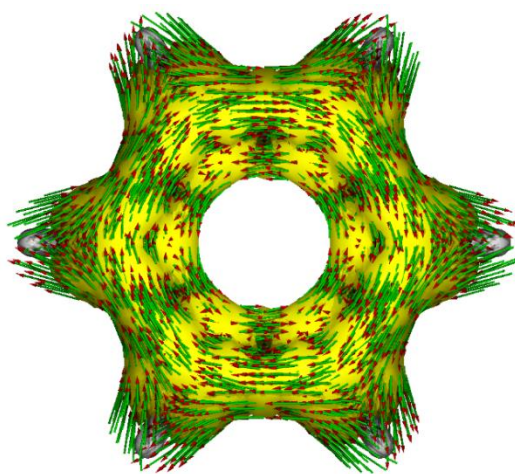


Figure 1.5. Current density vectors plotted onto the ACID surface of the benzene molecule.

This methodology is suitable for the study of the transition states computed in the chapter 3 of this thesis, whose aromaticity is key to understand the mechanism of the reaction.

1.3.5 Reaction kinetics

Most of the DFT calculations in this thesis are aimed to calculate the Gibbs free energy of different molecules: substrates, intermediates, products and transition states. Although this thesis is not centered in the study of reaction kinetics, using activation energies to estimate rate constants and visualize reaction rates can be very informative. This way, reaction times can be approximated, and when several reaction paths compete, the product ratio can be predicted.

1.3.5.1 Transition state theory

The transition state theory (TST) was developed in the 1930s by Eyring, Evans and Polanyi.⁵² TST is an approximate approach to calculate the rate constant of a reaction. The calculation of this rate constant depends exclusively on the potential energy in the saddle-point region, this is, the transition state.⁵³

Since our studies require the calculation of the Gibbs free activation energies, we used the expression of the rate constant based on this parameter:

$$k_{TST} = \frac{k_B T}{h} e^{\left(\frac{-\Delta G^\ddagger}{RT}\right)} \quad (1.6)$$

where k_B is Boltzmann's constant and h is Plack's constant. With this formula, the rate constants were calculated in order to give an approximation of the reaction time needed for the studied reactions to proceed. Since the calculation performed in this thesis were mostly based on experimental results, an approximation to the reaction time would allow us to evaluate the quality of the computed activation energies.

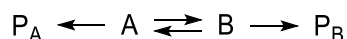
1.3.5.2 COPASI

COPASI (COMplex PATHway Simulator) is an open-source software for the simulation and analysis of biological network models.⁵⁴ These models are based on complex multi-component reactions, but the study of simpler reaction such as the ones performed in this thesis is also available.

COPASI was used to visualize reaction rates in chapter 5. When different reaction paths are available, calculating the product ratios and comparing them with experimental data can be very useful. Providing the rate constants calculated using TST for each transition state of each pathway, COPASI can use a simple mass action law to simulate the transformation of starting materials into intermediates and products over time. This tool can help us understand how reactions proceed, which intermediates accumulate or the final product ratios, all according to the energy barriers computed with DFT methods.

1.3.6 Curtin-Hammett principle

The Curtin-Hammett principle is used to predict the ratio of products on reactions that meet certain conditions.⁵⁵ It is usually applied to systems in which two conformers in equilibrium react, each forming a different product. While the conformers must be able to rapidly interconvert, the product formation must be irreversible.



Under these conditions, the Curtin-Hammett principle states that the ratio of products will depend exclusively on the energy difference between the two highest energy transition states ($\Delta\Delta G^\ddagger$).⁵⁶ In Figure 1.6, we can see a study case in which the principle can be applied; the transition state that goes from **A** to **B** is very low in energy, while the transition states leading to the products, **P_A** and **P_B**, are much higher in energy.

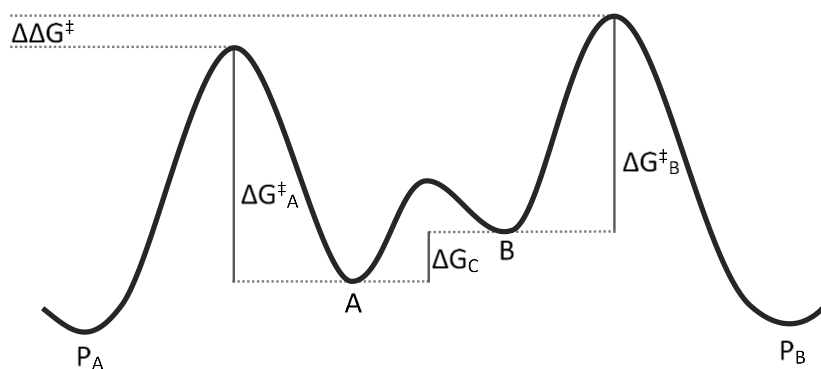


Figure 1.6. Representation of a reaction under Curtin-Hammett control.

Looking at the study case, it appears that the energy will depend on which reaction has the highest activation barrier, this is, ΔG^\ddagger_A or ΔG^\ddagger_B . Nevertheless, because the transformation from **A** to **B** is an equilibrium, energy difference between the two isomers (ΔG_C) has to be taken into account. In order to overcome the barrier leading to **P_B**, the substrate must first change from conformer **A** (the most stable isomer) to conformer **B**,

so the actual energy barrier will correspond to addition of ΔG_B^\ddagger and ΔG_C . This way, the mayor product will be **P_A**, as the transition state leading to it has a lower barrier, while the exact ratio will depend on the $\Delta\Delta G^\ddagger$ value.

According to the transition state theory previously described, the product ratio of this particular reaction would be calculated as follows:⁵⁵

$$k_r = \frac{k_B T}{h} e^{-\Delta G^\ddagger/RT} \quad \text{and} \quad K_c = e^{\Delta G_C/RT}$$

$$\text{Product ratio} = \frac{(k_B T/h) e^{-\Delta G_A^\ddagger/RT} e^{+\Delta G_C/RT}}{(k_B T/h) e^{-\Delta G_B^\ddagger/RT}} = e^{(-\Delta G_A^\ddagger + \Delta G_B^\ddagger + \Delta G_C)/RT}$$

Looking at Figure 1.6, we can make the final association:

$$(-\Delta G_A^\ddagger + \Delta G_B^\ddagger + \Delta G_C) = \Delta\Delta G^\ddagger = G_B - G_A$$

$$\text{Product ratio} = e^{(G_B - G_A)/RT}$$

During chapter 5, it was considered that the studied reaction met the conditions required for the Curtin-Hammett principle to apply. Therefore, the above-mentioned expressions were employed to estimate the final product ratios.

1.4 References

- (1) Lewars, E. G. *Computational Chemistry. Introduction to the Theory and Applications of Molecular and Quantum Mechanics*, 2nd ed.; Springer, 2011.
- (2) Cramer, C. J. *Essentials of Computational Chemistry: Theories and Models*, 2nd ed.; Wiley: Hoboken, NJ, 2004.
- (3) Leszczynski, J. *Handbook of Computational Chemistry*; Springer International Publishing: Cham, 2017.
- (4) Schrödinger, E. An Undulatory Theory of the Mechanics of Atoms and Molecules. *Phys. Rev.* **1926**, *28*, 1049–1070.
- (5) Born, M.; Oppenheimer, R. Zur Quantentheorie der Molekeln. *Ann. Phys.* **1927**, *389*, 457–484.
- (6) Dykstra, C. E.; Frenking, G.; Kim, K. S.; Scuseria, G. *Theory and Applications of Computational Chemistry: The First Forty Years*; Elsevier, 2005
- (7) Hohenberg, P.; Kohn, W. Inhomogeneous Electron Gas. *Phys. Rev.* **1964**, *136*, B864–B871.
- (8) Kohn, W.; Sham, L. J. Self-Consistent Equations Including Exchange and Correlation Effects. *Phys. Rev.* **1965**, *140*, A1133–A1138.
- (9) Jensen, F. *Introduction to Computational Chemistry*, 2nd ed.; John Wiley & Sons: Hoboken, NJ, 2007.
- (10) Perdew, J. P.; Schmidt, K. Jacob's Ladder of Density Functional Approximations for the Exchange-Correlation Energy. In *AIP Conference Proceedings*; AIP: Antwerp (Belgium), 2001; Vol. 577, pp 1–20.
- (11) (a) Becke, A. D. Density-Functional Exchange-Energy Approximation with Correct Asymptotic Behavior. *Phys. Rev. A* **1988**, *38*, 3098–3100. (b) Becke, A. D. Density-functional Thermochemistry. III. The Role of Exact Exchange. *J. Chem. Phys.* **1993**, *98*, 5648–5652.
- (12) Lee, C.; Yang, W.; Parr, R. G. Development of the Colle-Salvetti Correlation-Energy Formula into a Functional of the Electron Density. *Phys. Rev. B* **1988**, *37*, 785–789.
- (13) Sousa, S. F.; Fernandes, P. A.; Ramos, M. J. General Performance of Density Functionals. *J. Phys. Chem. A* **2007**, *111*, 10439–10452.
- (14) Koch, W.; Holthausen, M. C. *A Chemist's Guide to Density Functional Theory*, 2nd ed.; Wiley: Weinheim, 2001.
- (15) Zhao, Y.; Truhlar, D. G. The M06 Suite of Density Functionals for Main Group Thermochemistry, Thermochemical Kinetics, Noncovalent Interactions, Excited States, and Transition Elements: Two New Functionals and Systematic Testing of Four M06-Class Functionals and 12 Other Functionals. *Theor. Chem. Acc.* **2008**, *120*, 215–241.
- (16) Steinmann, S. N.; Piemontesi, C.; Delachat, A.; Corminboeuf, C. Why Are the Interaction Energies of Charge-Transfer Complexes Challenging for DFT? *J. Chem. Theory Comput.* **2012**, *8*, 1629–1640.
- (17) Chai, J.-D.; Head-Gordon, M. Long-Range Corrected Hybrid Density Functionals with Damped Atom-Atom Dispersion Corrections. *Phys. Chem. Chem. Phys.* **2008**, *10*, 6615.

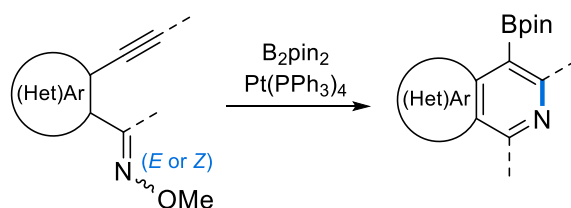
- (18) (a) Grimme, S. Semiempirical GGA-Type Density Functional Constructed with a Long-Range Dispersion Correction. *J. Comput. Chem.* **2006**, *27*, 1787–1799. (b) Grimme, S.; Antony, J.; Ehrlich, S.; Krieg, H. A Consistent and Accurate *Ab Initio* Parametrization of Density Functional Dispersion Correction (DFT-D) for the 94 Elements H-Pu. *J. Chem. Phys.* **2010**, *132*, 154104.
- (19) (a) Perdew, J. P. *Electronic Structure of Solids' 91*; Ziesche, P., Eschrig, H., Eds.; Akademie Verlag: Berlin, 1991. (b) Perdew, J. P.; Chevary, J. A.; Vosko, S. H.; Jackson, K. A.; Pederson, M. R.; Singh, D. J.; Fiolhais, C. Atoms, Molecules, Solids, and Surfaces: Applications of the Generalized Gradient Approximation for Exchange and Correlation. *Phys. Rev. B* **1992**, *46*, 6671–6687.
- (20) Peverati, R.; Truhlar, D. G. M11-L: A Local Density Functional That Provides Improved Accuracy for Electronic Structure Calculations in Chemistry and Physics. *J. Phys. Chem. Lett.* **2012**, *3*, 117–124.
- (21) (a) Hehre, W. J.; Ditchfield, R.; Pople, J. A. Self-Consistent Molecular Orbital Methods. XII. Further Extensions of Gaussian-Type Basis Sets for Use in Molecular Orbital Studies of Organic Molecules. *J. Chem. Phys.* **1972**, *56*, 2257–2261. (b) Francl, M. M.; Pietro, W. J.; Hehre, W. J.; Binkley, J. S.; Gordon, M. S.; DeFrees, D. J.; Pople, J. A. Self-consistent Molecular Orbital Methods. XXIII. A Polarization-type Basis Set for Second-row Elements. *J. Chem. Phys.* **1982**, *77*, 3654–3665.
- (22) McLean, A. D.; Chandler, G. S. Contracted Gaussian Basis Sets for Molecular Calculations. I. Second Row Atoms, $Z=11-18$. *J. Chem. Phys.* **1980**, *72*, 5639–5648.
- (23) Krishnan, R.; Binkley, J. S.; Seeger, R.; Pople, J. A. Self-consistent Molecular Orbital Methods. XX. A Basis Set for Correlated Wave Functions. *J. Chem. Phys.* **1980**, *72*, 650–654.
- (24) Clark, T.; Chandrasekhar, J.; Spitznagel, G. W.; Schleyer, P. v. R. Efficient Diffuse Function-augmented Basis Sets for Anion Calculations. III. The 3-21+G Basis Set for First-row Elements, Li-F. *J. Comput. Chem.* **1983**, *4*, 294–301.
- (25) (a) Wadt, W. R.; Hay, P. J. *Ab Initio* Effective Core Potentials for Molecular Calculations. Potentials for Main Group Elements Na to Bi. *J. Chem. Phys.* **1985**, *82*, 284–298. (b) Hay, P. J.; Wadt, W. R. *Ab Initio* Effective Core Potentials for Molecular Calculations. Potentials for the Transition Metal Atoms Sc to Hg. *J. Chem. Phys.* **1985**, *82*, 270–283. (c) Hay, P. J.; Wadt, W. R. *Ab Initio* Effective Core Potentials for Molecular Calculations. Potentials for K to Au Including the Outermost Core Orbitals. *J. Chem. Phys.* **1985**, *82*, 299–310.
- (26) (a) Igel-Mann, G.; Stoll, H.; Preuss, H. Pseudopotentials for Main Group Elements (IIIa through VIIa). *Mol. Phys.* **1988**, *65*, 1321–1328. (b) Schwerdtfeger, P.; Dolg, M.; Schwarz, W. H. E.; Bowmaker, G. A.; Boyd, P. D. W. Relativistic Effects in Gold Chemistry. I. Diatomic Gold Compounds. *J. Chem. Phys.* **1989**, *91*, 1762–1774. (c) Andrae, D.; Häußermann, U.; Dolg, M.; Stoll, H.; Preuß, H. Energy-Adjusted *Ab Initio* Pseudopotentials for the Second and Third Row Transition Elements. *Theor. Chim. Acta* **1990**, *77*, 123–141.
- (27) Weigend, F.; Ahlrichs, R. Balanced Basis Sets of Split Valence, Triple Zeta Valence and Quadruple Zeta Valence Quality for H to Rn: Design and Assessment of Accuracy. *Phys. Chem. Chem. Phys.* **2005**, *7*, 3297–3305.
- (28) Hellmann, H. A New Approximation Method in the Problem of Many Electrons. *J. Chem. Phys.* **1935**, *3*, 61.
- (29) Miertuš, S.; Scrocco, E.; Tomasi, J. Electrostatic Interaction of a Solute with a Continuum. A Direct Utilization of *Ab Initio* Molecular Potentials for the Prevision of Solvent Effects. *Chem. Phys.* **1981**, *55*, 117–129.

- (30) Gaussian 09, Revision D.01; Frisch, M. J.; Trucks, G. W.; Schlegel, H. B.; Scuseria, G. E.; Robb, M. A.; Cheeseman, J. R.; Scalmani, G.; Barone, V.; Mennucci, B.; Petersson, G. A.; Nakatsuji, H.; Caricato, M.; Li, X.; Hratchian, H. P.; Izmaylov, A. F.; Bloino, J.; Zheng, G.; Sonnenberg, J. L.; Hada, M.; Ehara, M.; Toyota, K.; Fukuda, R.; Hasegawa, J.; Ishida, M.; Nakajima, T.; Honda, Y.; Kitao, O.; Nakai, H.; Vreven, T.; Montgomery, J. A.; Peralta, J. E.; Ogliaro, F.; Bearpark, M.; Heyd, J. J.; Brothers, E.; Kudin, K. N.; Staroverov, V. N.; Keith, T.; Kobayashi, R.; Normand, J.; Raghavachari, K.; Rendell, A.; Burant, J. C.; Iyengar, S. S.; Tomasi, J.; Cossi, M.; Rega, N.; Millam, J. M.; Klene, M.; Knox, J. E.; Cross, J. B.; Bakken, V.; Adamo, C.; Jaramillo, J.; Gomperts, R.; Stratmann, R. E.; Yazyev, O.; Austin, A. J.; Cammi, R.; Pomelli, C.; Ochterski, J. W.; Martin, R. L.; Morokuma, K.; Zakrzewski, V. G.; Voth, G. A.; Salvador, P.; Dannenberg, J. J.; Dapprich, S.; Daniels, A. D.; Farkas, O.; Foresman, J. B.; Ortiz, J. V.; Cioslowski, J.; Fox, D. J. Gaussian, Inc., Wallingford CT, 2013.
- (31) Hanwell, M. D.; Curtis, D. E.; Lonie, D. C.; Vandermeersch, T.; Zurek, E.; Hutchison, G. R. Avogadro: An Advanced Semantic Chemical Editor, Visualization, and Analysis Platform. *J. Cheminformatics* **2012**, *4*, 17.
- (32) Rappé, A. K.; Casewit, C. J.; Colwell, K. S.; Goddard, W. A.; Skiff, W. M. UFF, a Full Periodic Table Force Field for Molecular Mechanics and Molecular Dynamics Simulations. *J. Am. Chem. Soc.* **1992**, *114*, 10024-10035.
- (33) Schaftenaar, G.; Noordik, J. H. Molden: A Pre- and Post-Processing Program for Molecular and Electronic Structures. *J. Comput.-Aided Mol. Des.* **2000**, *14*, 123-134.
- (34) Dennington, R.; Keith, T.; Millam, J. *GaussView 5.0*; Semichem Inc.: Shawnee Mission, KS, 2009.
- (35) Legault, C. Y. *CYLview 1.0b*; Université de Sherbrooke: (<http://www.cylview.org>), 2009.
- (36) Persistence of Vision Pty. Ltd. (2004). Persistence of Vision (TM) Raytracer. Persistence of Vision Pty. Ltd., Williamstown, Victoria, Australia. <http://www.pov-ray.org/>.
- (37) Frenking, G.; Shaik, S. *The Chemical Bond: Fundamental Aspects of Chemical Bonding*; Wiley-VCH: Weinheim, 2014.
- (38) Weinhold, F.; Landis, C. R.; Glendening, E. D. What Is NBO Analysis and How Is It Useful? *Int. Rev. Phys. Chem.* **2016**, *35*, 399-440.
- (39) (a) Foster, J. P.; Weinhold, F. Natural Hybrid Orbitals. *J. Am. Chem. Soc.* **1980**, *102*, 7211-7218. (b) Reed, A. E.; Curtiss, L. A.; Weinhold, F. Intermolecular Interactions from a Natural Bond Orbital, Donor-Acceptor Viewpoint. *Chem. Rev.* **1988**, *88*, 899-926.
- (40) Reed, A. E.; Weinhold, F. Natural Localized Molecular Orbitals. *J. Chem. Phys.* **1985**, *83*, 1736-1740.
- (41) Glendening, E. D.; Reed, A. E.; Carpenter, J. E.; Weinhold, F. *NBO 3.1*; Theoretical Chemistry Institute, University of Wisconsin: Madison, WI, 1998.
- (42) Solà, M. Why Aromaticity Is a Suspicious Concept? Why? *Front. Chem.* **2017**, *5*, 22.
- (43) Bachrach, S. M. *Computational Organic Chemistry*; Wiley-Interscience: Hoboken, N.J., 2007.
- (44) Dauben, H. J. Jr.; Wilson, J. D.; Laity, J. L. Diamagnetic Susceptibility Exaltation as a Criterion of Aromaticity. *J. Am. Chem. Soc.* **1968**, *90*, 811-813.
- (45) Wannere, C. S.; Corminboeuf, C.; Allen, W. D.; Schaefer, H. F.; Schleyer, P. von R. Downfield Proton Chemical Shifts Are Not Reliable Aromaticity Indicators. *Org. Lett.* **2005**, *7*, 1457-1460.

- (46) Schleyer, P. von R.; Maerker, C.; Dransfeld, A.; Jiao, H.; van Eikema Hommes, N. J. R. Nucleus-Independent Chemical Shifts: A Simple and Efficient Aromaticity Probe. *J. Am. Chem. Soc.* **1996**, *118*, 6317–6318.
- (47) Schleyer, P. von R.; Jiao, H.; Hommes, N. J. R. van E.; Malkin, V. G.; Malkina, O. L. An Evaluation of the Aromaticity of Inorganic Rings: Refined Evidence from Magnetic Properties. *J. Am. Chem. Soc.* **1997**, *119*, 12669–12670.
- (48) Černušák, I.; Fowler, P. W.; Steiner, E. Ring Currents in Six-Membered Heterocycles: The Diazaborinines (CH)₂B₂N₂. *Mol. Phys.* **2000**, *98*, 945–953.
- (49) Fallah-Bagher-Shaidaei, H.; Wannere, C. S.; Corminboeuf, C.; Puchta, R.; Schleyer, P. von R. Which NICS Aromaticity Index for Planar π Rings Is Best? *Org. Lett.* **2005**, *8*, 863–866.
- (50) Feixas, F.; Matito, E.; Poater, J.; Solà, M. On the Performance of Some Aromaticity Indices: A Critical Assessment Using a Test Set. *J. Comput. Chem.* **2008**, *29*, 1543–1554.
- (51) Geuenich, D.; Hess, K.; Köhler, F.; Herges, R. Anisotropy of the Induced Current Density (ACID), a General Method To Quantify and Visualize Electronic Delocalization. *Chem. Rev.* **2005**, *105*, 3758–3772.
- (52) (a) Eyring, H. The Activated Complex in Chemical Reactions. *J. Chem. Phys.* **1935**, *3*, 107–115. (b) Evans, M. G.; Polanyi, M. Some Applications of the Transition State Method to the Calculation of Reaction Velocities, Especially in Solution. *Trans. Faraday Soc.* **1935**, *31*, 875–894. (c) Laidler, K. J.; King, M. C. The Development of Transition-State Theory. *J. Phys. Chem.* **1983**, *87*, 2657–2664.
- (53) Henriksen, N. E.; Hansen, F. Y. *Theories of Molecular Reaction Dynamics: The Microscopic Foundation of Chemical Kinetics*; Oxford University Press: Oxford; New York, 2008.
- (54) Hoops, S.; Sahle, S.; Gauges, R.; Lee, C.; Pahle, J.; Simus, N.; Singhal, M.; Xu, L.; Mendes, P.; Kummer, U. COPASI—a COMplex PATHway Simulator. *Bioinformatics* **2006**, *22*, 3067–3074.
- (55) Carey, F. A.; Sundberg, R. J. *Advanced Organic Chemistry. Part A: Structure and Mechanisms*, 5th ed.; Springer: New York, 2007.
- (56) (a) Curtin, D. Y. Stereochemical Control of Organic Reactions; Differences in Behaviour of Diastereoisomers. *Rec. Chem. Prog.* **1954**, 111–128. (b) Hammett, L. P. *Physical Organic Chemistry*, 2nd ed.; McGraw-Hill, 1970.

Chapter 2.

Reactivity of *E* and *Z*-Oxime Ethers in 6π -Electrocyclization Reactions



In the present chapter, we have studied the mechanism of 6π -electrocyclizations of oxime ethers. A comprehensive computational study was conducted in view of the experimental results obtained by our collaborators at the University of Sheffield and the pharmaceutical company Sanofi-Aventis. They synthesized functionalized isoquinolines and azole-fused pyridines through diboration and later 6π -electrocyclization of oxime ethers, whose *E/Z* configuration was essential for the outcome of the reaction. We studied the mechanism of the reaction by means of DFT, focusing on the divergent reactivity of the different oxime isomers.

Chapter based on the publication:

[1] Mora-Radó, H.; Sotorríos, L.; Ball-Jones, M. P.; Bialy, L.; Czechtizky, W.; Méndez, M.; Gómez-Bengoa, E.; Harrity, J. P. A. Synthetic and Mechanistic Investigation of an Oxime Ether Electrocyclization Approach to Heteroaromatic Boronic Acid Derivatives. *Chem. Eur. J.* **2018**, *24*, 9530-9534.

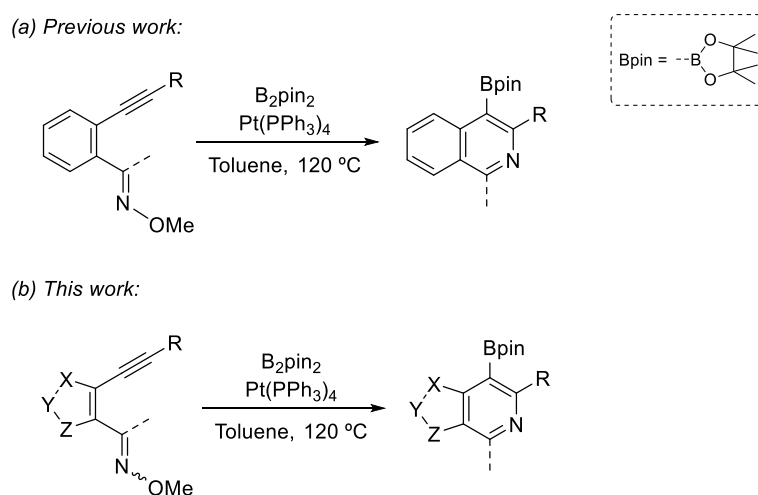
2.1 Context

This chapter of the thesis is based on a collaboration carried out with experimental researchers. The experimental reactions were performed in Prof. Joseph Harrity's group, from the University of Sheffield and in the department of Integrated Drug Discovery at Sanofi-Aventis Deutschland GmbH, Frankfurt. For more information, please see the full article available in the appendix.

The investigations carried out by the author of this thesis are exclusively computational and will be presented in the *results and discussion* section. The aim of this section is to provide a context for these investigations by introducing the nature of the chemistry, as well as briefly discussing the aim, procedures and results of the experimental studies.

2.1.1 Objective

The aim of the experimental study conducted by our colleagues was the synthesis ofazole-fused pyridines bearing a boronic ester moiety. The applied strategy, which they had previously reported for the synthesis of isoquinolines,¹ consisted of a cascade reaction usingazole-containing oxime ethers bearing an *ortho*-alkyne group. The key step of this cascade reaction is the 6 π -azaelectrocyclization that constructs the six membered ring.



Scheme 2.1. Heteroaromatic boronic ester synthesis.

2.1.1.1 Azole-fused pyridines

Nitrogen-based heterocyclic compounds constitute important building blocks for organic synthesis, as they are present in numerous alkaloids and biologically active compounds. Among them, azole-fused pyridines stand out, as numerous compounds displaying a wide range of biological effects have been developed.

The imidazopyridine sulmazole,² for example, is an A1 adenosine receptor antagonist utilized as cardiostimulant agent for the improvement of the contraction of the heart. A different imidazopyridine, miransertib, has recently shown promising effects in patients suffering from Proteus syndrome,³ a deadly disease that causes the progressive overgrowth of any region of the body.

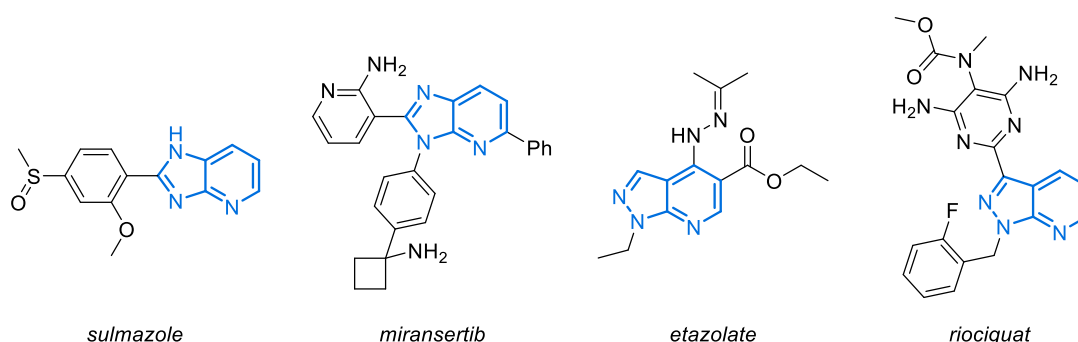


Figure 2.1. Examples of azole-fused pyridine containing biologically active compounds.

Several drugs bearing a pyrazole-fused pyridine have been described. Etazolate⁴ is a phosphodiesterase IV inhibitor with antidepressant and anxiolytic properties. The pyrazolopyridine riociguat is a stimulator of the guanylate cyclase used for the treatment of pulmonary arterial hypertension.⁵

The aforementioned structures cannot be synthesized through the approach reported in this chapter, as the relative position of the nitrogen is different. Nonetheless, biologically active molecules with a suitable scaffold can also be found. For example, the oxazolopyridine shown in Figure 2.2 is an antagonist of the histamine H₃-receptors.⁶ Also, a set of thiazole and isothiazole-fused pyridines have shown inhibitory effects over the spleen tyrosine kinase,⁷ involved in autoimmune diseases.

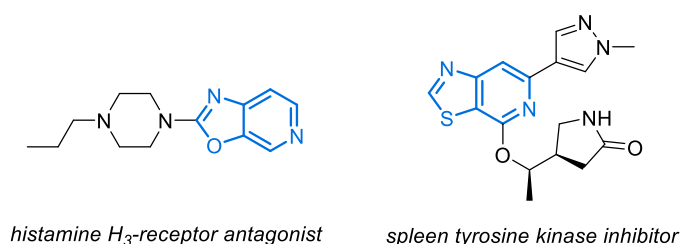


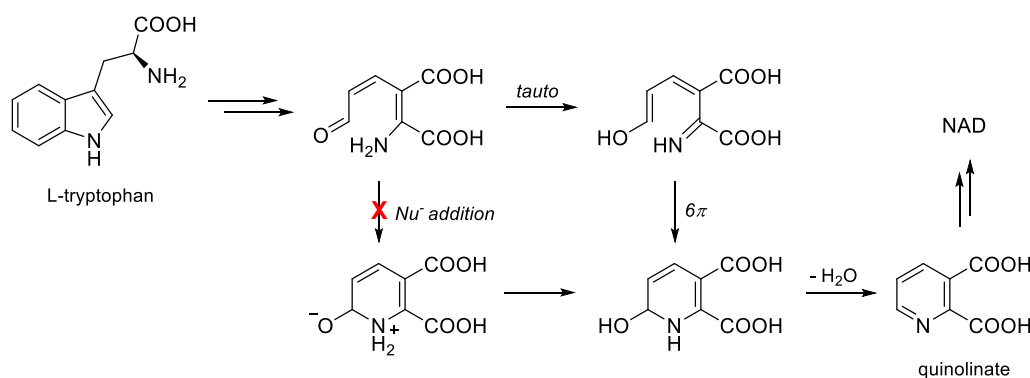
Figure 2.2. Further examples of azole-fused pyridine containing biologically active compounds.

2.1.2 State of the art

Electrocyclizations are powerful bond-forming processes for the synthesis of complex molecules. Unlike cycloadditions or sigmatropic rearrangements, electrocyclizations remain relatively unexplored; the need of considerably high temperatures prevents their application to highly functionalized substrates.⁸ This inconvenience can be tackled by introducing suitable functional groups that lower the activation energy of the reaction. Another common approach is the introduction of heteroatoms to the backbone of the π -system, such as nitrogen or oxygen. The use of nitrogen in 6 π -system is remarkably appealing, as it leads to the synthesis of valuable dihydropyridines and pyridines (after oxidation, elimination or dehydrogenation).⁹

2.1.2.1 6 π -Azaelectrocyclizations

6 π -Electrocyclizations of 1-azahexatrienes play an important role in nature. The most remarkable example is that of nicotinamide adenine dinucleotide, NAD. One of the two main routes for its biosynthesis, named *de novo* pathway, includes a 6 π -azaelectrocyclization reaction. Colabroy and Begley¹⁰ found that the synthesis of the pyridine containing quinolinate proceeds through a non-enzymatic 6 π -azaelectrocyclization reaction (Scheme 2.2).



Scheme 2.2. Mechanistic proposal of Colabroy and Begley of the *de novo* route for the biosynthesis of NAD from L-tryptophan.

The 6 π -electrocyclization of 1-azahexatrienes has been employed for the total synthesis of around 20 natural products.⁹ Most of this synthesis were aimed to the construction of heteropolyaromatic systems, such as scorpinone¹¹ and flavocarpine¹² (Figure 2.3). A few isoquinolines have been synthesized (e.g. cassiarin C¹³ and aspergillitine¹⁴), while only twoazole-fused pyridines (imidazole-fused) have been achieved: ageladine A¹⁵ and grossularine 1.¹⁶ The synthesis of enantiopure saturated heterocycles such as (-)-hippodamine¹⁷ was also accomplished.

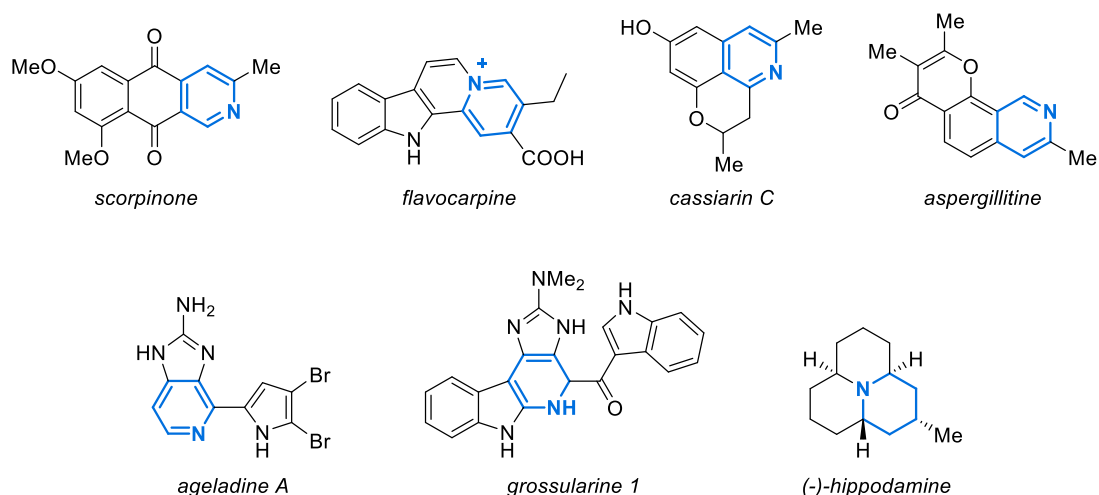


Figure 2.3. Natural products synthesized via 6π -electrocyclization of 1-azahexatrienes. In blue, rings assembled using this reaction.

Most of the syntheses used oxime ethers as substrates for the electrocyclizations. Nevertheless, the *E/Z*-configuration of the oximes was never a matter of study. Usually, *E*-oximes were employed, although some of the studies provided no information on the *E/Z* ratio of the substrates.

2.1.2.2 Organoborates

The cascade reaction reported in this chapter deliversazole-fused pyridines bearing a boronic ester functionality. Boronic acids and esters are excellent functional groups for the introduction of further structural complexity.¹⁸ They are remarkably useful and versatile substrates in organic and organometallic chemistry. Their unique combination of high stability and rich reactivity makes them exceptional substrates for a wide range of functionalization reactions, including cross-coupling reactions.^{18b}

There are a few established methods for the synthesis of heteroaromatic boronic acid derivatives, such as C-X and C-H borylation,¹⁹ annulative borylations²⁰ and cycloaddition reactions.²¹ The 6π -electrocyclization treated in this chapter represents an interesting alternative to the aforementioned approaches.

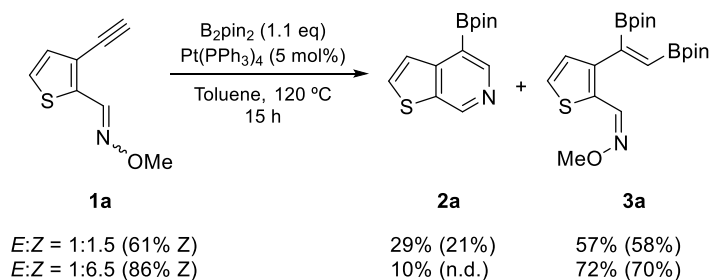
2.1.3 Experimental

The reported methodology consists in a cascade reaction in three steps (Scheme 2.3). The reaction starts with the platinum-catalyzed diboration of an alkyne using bis(pinacolato)diboron (B_2pin_2). Next, the diborylated product undergoes a 6π -electrocyclization to form a six membered ring. A final elimination occurs to aromatize the intermediate and deliver the finalazole-fused pyridine.



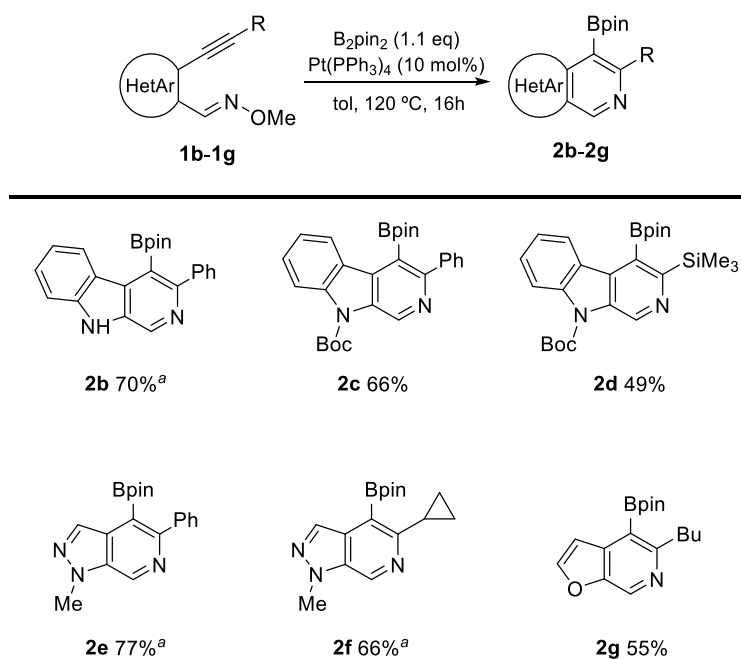
Scheme 2.3. Cascade reaction of oxime ethers for the synthesis of azole-fused pyridines.

The first substrate they subjected to the diboration-electrocyclization cascade reaction was thiophene **1a** (Scheme 2.4). The reaction in toluene of **1a** (61% of *Z*-isomer) with B_2pin_2 and $Pt(PPh_3)_4$ as catalyst provided the thienopyridine boronic ester **2a** in poor yield.

Scheme 2.4. Synthesis of borylated thienopyridines. Estimated yields obtained by 1H NMR spectroscopy with isolated yields in parentheses. n.d.: Not determined.

The remaining mass balance consisted of diborylated alkene **3a**, containing exclusively the *Z*-configuration at the oxime. When the *E*:*Z* ratio was decreased to 1:6.5, an even lower yield of **2a** was obtained, which suggests that the *Z*-isomer could undergo the diboration to generate **3a**, but was inert to electrocyclization.

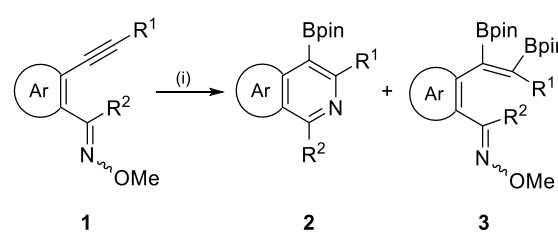
The scope of the reaction was extended by synthesizing several heterocycle-fused pyridines (Scheme 2.5). The *E*-configuration of the oxime was employed in all substrates (from **1b** to **1g**) and the achieved yields were from good to excellent.

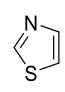
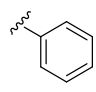
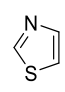
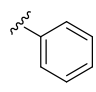
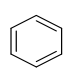
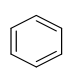
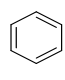
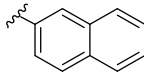
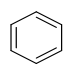
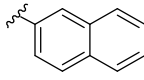


Scheme 2.5. Scope of the reaction of diboration-electrocyclization approach to heteroaryl boronates. ^aThe reaction was further heated at 200 °C in 1,2-dichlorobenzene for 16 h.

They performed more reactions with *E/Z* oximes to check whether *Z*-oximes were unreactive regardless of the substrate (Table 2.1). That was indeed the case, as *E*-oximes provided good yields of the desired product (entries 1, 3 and 5) while *E/Z* mixtures (entry 2) and *Z*-oximes (entries 4 and 6) provided mostly the diborylated product.

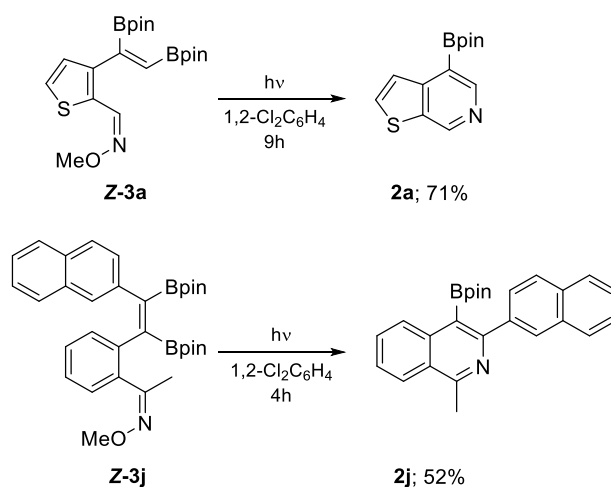
Table 2.1. Diboration-electrocyclization efficiency in relation to oxime ether stereochemistry.



Entry	1	Ar	R ¹	R ²	2	Yield (%)	3	Yield (%)
1	<i>E</i> -1h			H	2h	65	<i>E</i> -3h	<2
2	<i>E/Z</i> -1h (1:9)			H	2h	9 ^a	<i>Z</i> -3h	44 ^a
3	<i>E</i> -1i		H	Me	2i	73	<i>E</i> -3i	<2
4	<i>Z</i> -1i		H	Me	2i	<2	<i>Z</i> -3i	88
5	<i>E</i> -1j			Me	2j	95	<i>E</i> -3j	<2
6	<i>Z</i> -1j			Me	2j	2	<i>Z</i> -3j	63

(i) B₂pin₂, 10 mol% Pt(PPh₃)₄, toluene, 120 °C, 16 h; then 1,2-Cl₂C₆H₄, 200 °C, 16 h. ^aEstimated yields obtained by ¹H NMR spectroscopy.

With these results in hands, they assumed that the *Z*-oximes were essentially inert to electrocyclization. This evidence can be considered a limitation of the reaction, since significant proportions of the *Z*-isomer are usually formed during the synthesis of the substrates. Therefore, they considered exposing their substrates to UV light, in order to either promote the conrotatory cyclization reaction, or photochemically induce the isomerization of *Z*-oximes to *E*-oximes. Two of the *Z*-diborylated products, **3a** and **3j**, were subjected to UV light in 1,2-dichlorobenzene. Satisfyingly, cycle-fused pyridines **2a** and **2j** were obtained in good yields (Scheme 2.6).

Scheme 2.6. Photochemically promoted reaction conducted on diborylated *Z*-oximes.

The reaction of **3j** was monitored via LC-MS and ¹H NMR in order to determine the role of the UV light. The simultaneous formation of the *E*-oxime and product **2j** could be observed, which indicates that the reaction is proceeding through the photochemically promoted isomerization of the oxime and later thermal 6π-electrocyclization.

In conclusion, the synthesis of heterocyclic boronic acid derivatives was successfully achieved. The 6π-electrocyclization step was proved to be dependent on the configuration of the substrate's oxime ether, as *Z*-oximes were unreactive. The exposure of *Z*-oxime ethers to UV radiation promoted their photochemical isomerization, making them suitable to undergo the electrocyclization reaction. The reason for the inertness of the *Z*-oximes remained unknown and needed further investigation.

2.2 Computational approach

2.2.1 Objective

Our main objective was to computationally simulate the observed experimental selectivity. We intended to calculate the transition states of the 6π -electrocyclization to confirm the inactivity of the *Z*-oximes. But more importantly, we wanted to give a rationale for this divergent reactivity. The study of the *E* and *Z*-transition states could help in understanding whether it is a matter of hindrance or simple electronic effects. Nevertheless, if the reasons were more complex, a deeper study of the electronic charges, orbitals, etc. would be required.

2.2.2 General methods

For references and a more detailed description of the methodology, levels of theory and software, please see chapter 1.

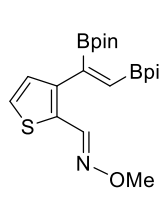
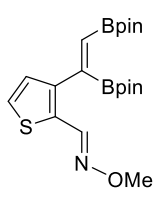
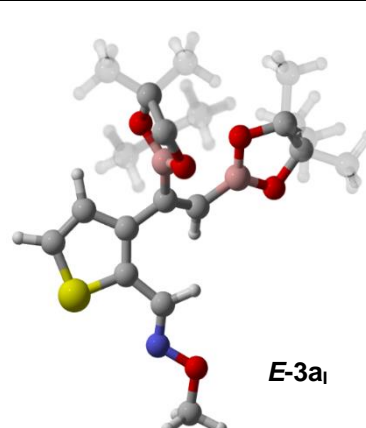
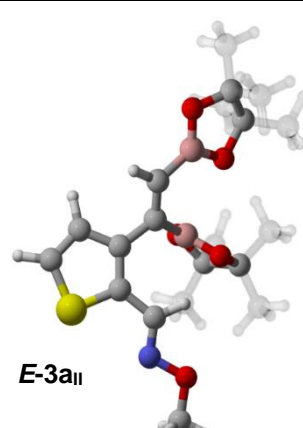
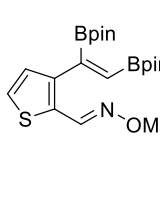
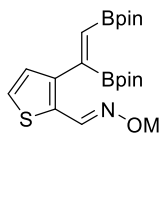
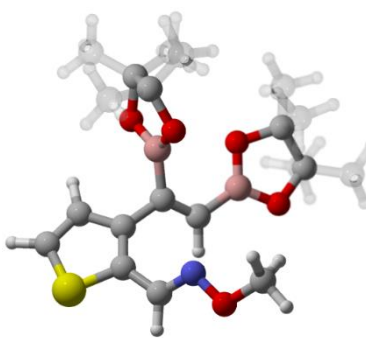
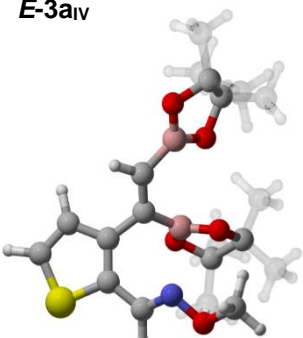
All structures were optimized using density functional theory with the M06-2X functional and the 6-311G(d,p) basis set as implemented in Gaussian09. Solvation factors were introduced with the IEF-PCM method, using toluene as indicated in the text and figures. The stationary points were characterized by frequency calculations in order to verify that they have the right number of imaginary frequencies. The electrostatic potential surfaces were mapped over the total density (density isovalue = 0.004) using the GaussView software. The remaining 3D figures were generated with the CYLview software.

2.3 Results and discussion

2.3.1 Mechanism

Because the diboration step does not seem to affect the outcome of the reaction, we focused our study on the 6π -electrocyclization reaction. Initially, the diborylated structures **E-3a** and **Z-3a** were optimized. A small conformational study was conducted on each one, to determine their most stable conformation.

Table 2.2. Conformational study conducted on **E-3a**. Relative energies (ΔG) referred to the lowest energy conformation, 0.0 kcal/mol.

 E-3a_I	 E-3a_{II}	 E-3a_I	 E-3a_{II}	
 E-3a_{III}	 E-3a_{IV}	 E-3a_{III}	 E-3a_{IV}	
Conformation	E-3a_I	E-3a_{II}	E-3a_{III}	E-3a_{IV}
ΔG (kcal/mol)	0.0	0.8	5.1	3.5

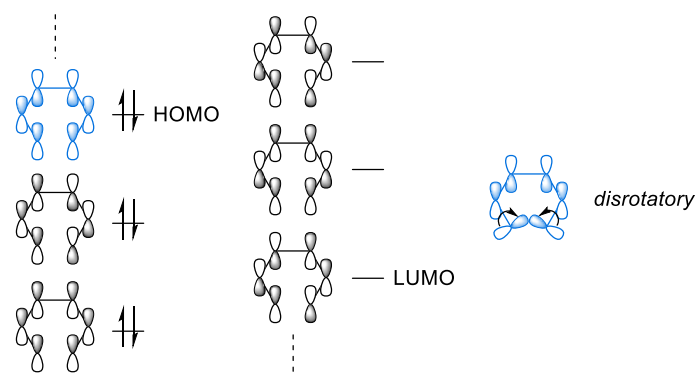
The most stable conformation of **E-3a** is **E-3a_I** (Table 2.2). Looking at the 3D structures above, it certainly seems to be the least hindered conformation. Rotating the upper C-C bond provides conformation **E-3a_{II}**, with a slightly higher free energy, 0.8 kcal/mol. Rotating the lower C-C bond, provides structures **E-3a_{III}** and **E-3a_{IV}**, which are quite higher in energy (5.1 and 3.5 kcal/mol, respectively), probably due to a stronger hindrance between the oxime and the alkene.

Table 2.3. Conformational study conducted on **Z-3a**. Relative energies (ΔG) referred to the lowest energy conformation, 0.0 kcal/mol.

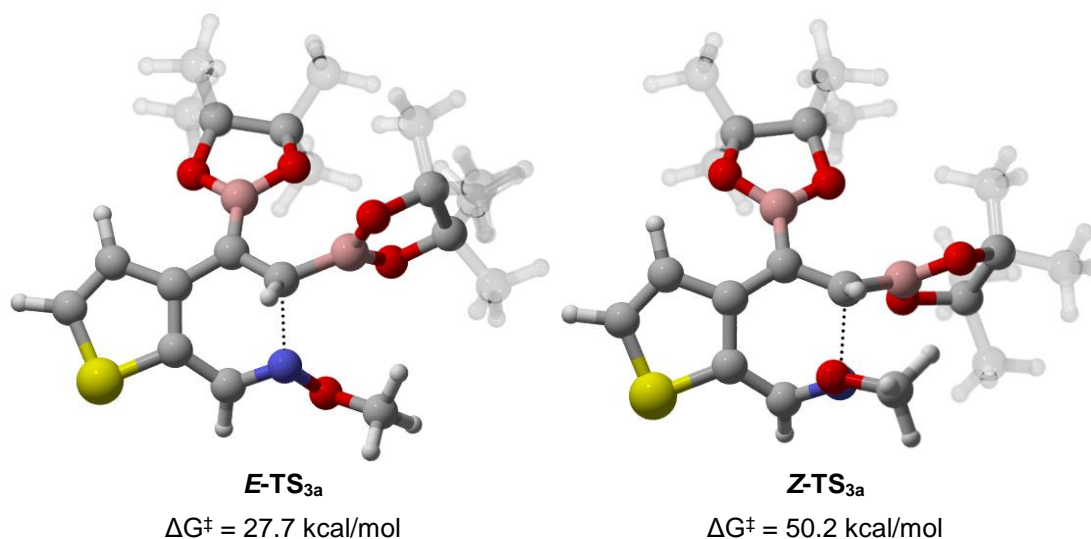
Conformation	Z-3a_I	Z-3a_{II}	Z-3a_{III}	Z-3a_{IV}
ΔG (kcal/mol)	4.1	3.7	0.0	0.0

At a glance, we can see that results for **Z-3a** (Table 2.3) are quite the opposite. The two conformations where the oxime is pointing towards the alkene, **Z-3a_{III}** and **Z-3a_{IV}**, are preferred over the apparently less sterically hindered **Z-3a_I** and **Z-3a_{II}**. This is likely due to the short distance between the sulfur and the oxygen atoms in **Z-3a_I** and **Z-3a_{II}**, which produces a destabilizing effect.

With the optimized molecules in hand, we searched for the transition states of the 6π -electrocyclization. As predicted by the Woodward-Hoffmann rules, the mechanism of the reaction is disrotatory (Figure 2.4). When the opposite orbital symmetry was attempted, no transition state could be located.

Figure 2.4. 2D Representation of the orbitals for a 6π -electrocyclization.

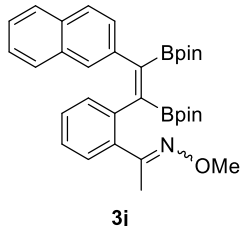
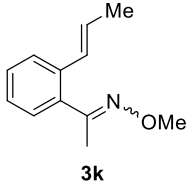
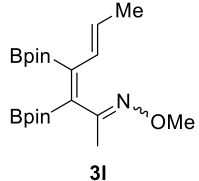
The two transition states could be located, although **Z-TS_{3a}** had a difficult convergence, as the *Z*-oxime would often isomerize prior to the optimization of the transition state. In Figure 2.5, the structures of both transition states and their activation energies are shown.

Figure 2.5. Transition states and activation energies of the 6π -electrocyclizations of **E-3a** and **Z-3a**.

The energy difference between the two activation barriers is immense. A reaction with an activation barrier of 27.7 kcal/mol should proceed, according to Eyring equation (1.6), in a few minutes (applying intense heating). Meanwhile, a barrier of 50.2 kcal/mol is unreasonably high, equivalent to a reaction time of the order of millions of years.

Before searching for the origin of this divergent reactivity, we computed a few more reactions, in order to check whether the extremely high activation energy of the *Z*-oxime was independent of the substrate. We conducted our study on three different molecules **3j**, **3k** and **3l** (Table 2.4). We employed the aforementioned **3j**, which contains a phenyl group instead of a heterocycle and carries a bulky naphthalene moiety. **3k** is also phenyl based, but lacks the boryl moiety and is not sterically hindered. Finally, we used **3l**, a non-aromatic substrate.

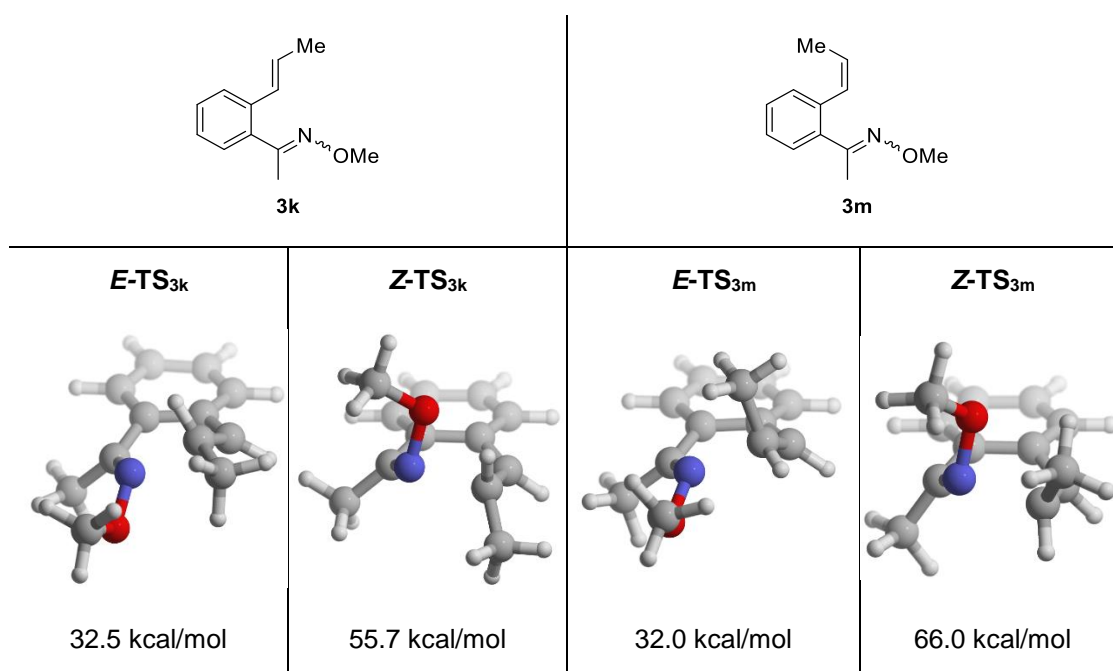
Table 2.4. Activation energies of the *E* and *Z*-transition states of the three computed structures.

						
	<i>E</i> -TS _{3j}	<i>Z</i> -TS _{3j}	<i>E</i> -TS _{3k}	<i>Z</i> -TS _{3k}	<i>E</i> -TS _{3l}	<i>Z</i> -TS _{3l}
ΔG^\ddagger (kcal/mol)	31.3	62.8	32.5	55.7	24.2	43.8

All the barriers of the *E*-transition states are feasible, since in some cases the reactions were heated up to 200 °C. On the other hand, none of the *Z*-transition states are achievable. The transition states for **3l** are lower in energy, probably because the molecule is linear and no changes in aromaticity occur during the reaction, differently from the other cases. Nonetheless, **Z-TS_{3l}**, with an activation barrier of 43.8 kcal/mol, is not affordable, and even at high temperatures it would need *ca.* one year to take place.

2.3.2 Origin of the selectivity

Because we saw that the configuration of the oxime ether was crucial for the outcome of the reaction, we wondered if the configuration of the terminal alkene would have a similar effect on the activation barrier. In spite of its slightly high activation barrier for the *E*-isomer, we chose **3k** due to its simplicity.

Figure 2.6. Activation Gibbs free energies of the 6 π -electrocyclization of **3k** and **3m**.

As we can see in Figure 2.6, the configuration of the terminal alkene does not influence the activation energy as much as the configuration of the oxime does. The activation energy of the *E*-oximes is almost the same (32.5 vs 32.0 kcal/mol), while in the case of the *Z*-oximes the activation energy of the *Z*-alkene (**3m**) is moderately higher (55.7 vs 66.0 kcal/mol), probably due to the steric hindrance between the methyl group and the methoxy group. From these results, we can infer that the *Z*-configuration of a double bond does not necessarily imply a much higher activation barrier; in fact, the activation energy of the *Z*-alkene **E-TS_{3m}** is 0.5 kcal/mol lower than that of the *E*-alkene **E-TS_{3k}**.

Next, we wondered about the reasons for such a large energy difference between the *E* and *Z*-transition states, because the mere examination of the 3D structures shown in Figure 2.6 was not informative. Thus, we decided to visualize the electrostatic potential map of the transition states, in order to compare their charge density distribution. In Figures 2.7-2.9, the electrostatic potential is mapped over the electronic density of the *E*-transition state of **3k**. The color blue represents positive charge, while red indicates negative charge. The point of view is indicated on the 2D structure on the right.

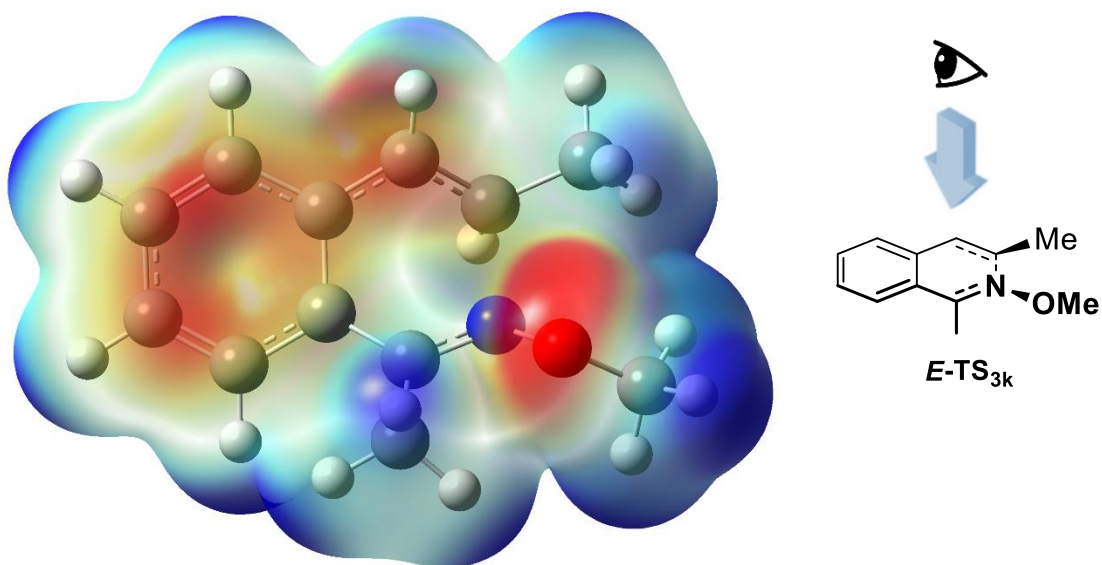


Figure 2.7. Electrostatic potential map of **E-TS_{3k}** (view from above).

On the first figure (*vide supra*), we can identify two negatively charged areas. The aromatic ring has a noticeable negative charge, which is extended to the conjugated alkene. The oxygen, on the other hand, presents a very strong negative charge, due to its two lone electron pairs. We can spot positive charge on all hydrogens, especially in those attached to the carbon adjacent to the oxygen.

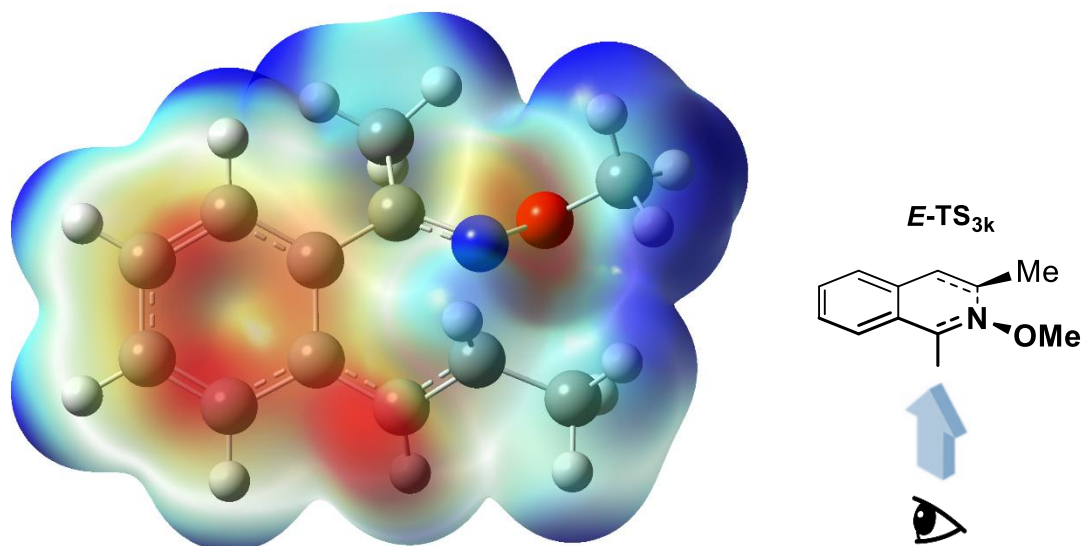


Figure 2.8. Electrostatic potential map of $E\text{-TS}_{3k}$ (view from below).

We encountered a similar situation in Figure 2.8. The conjugation of the alkene is more intense from this perspective and a dark red area can be seen around the oxygen atom. This is due to the transparency of the surface, since the lone pairs are at the other side of the molecule.

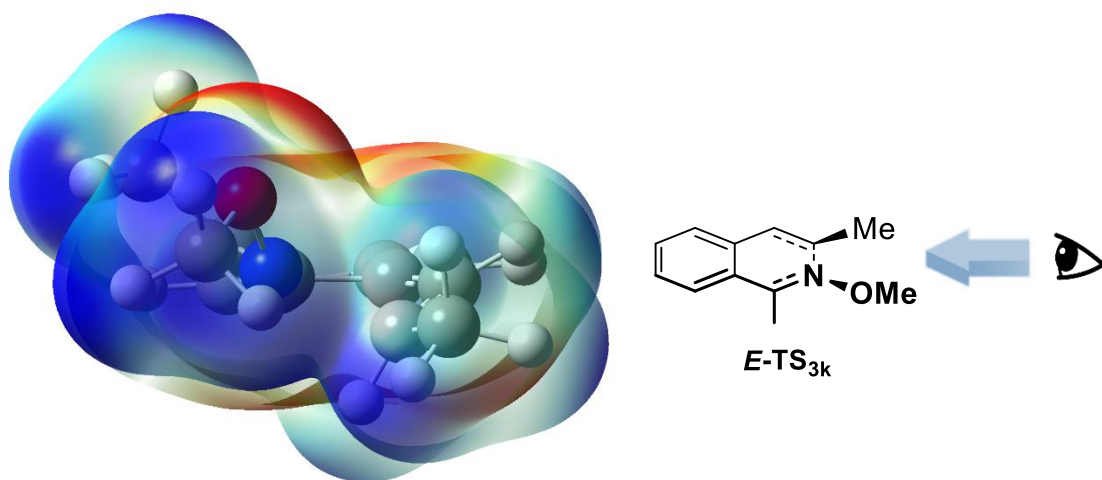


Figure 2.9. Electrostatic potential map of $E\text{-TS}_{3k}$ (view from the side).

The final perspective in Figure 2.9 does not provide more information: we can see the positive charge of the methyl group from the oxime ether and the negative charge of the lone pairs above the oxygen atom.

In Figures 2.10-2.12, the surfaces from identical perspectives of the Z -transition state of molecule **3k** are shown. Gratifyingly, we came across significant differences in the surface that exposed the reason for the divergent reactivity of the oximes.

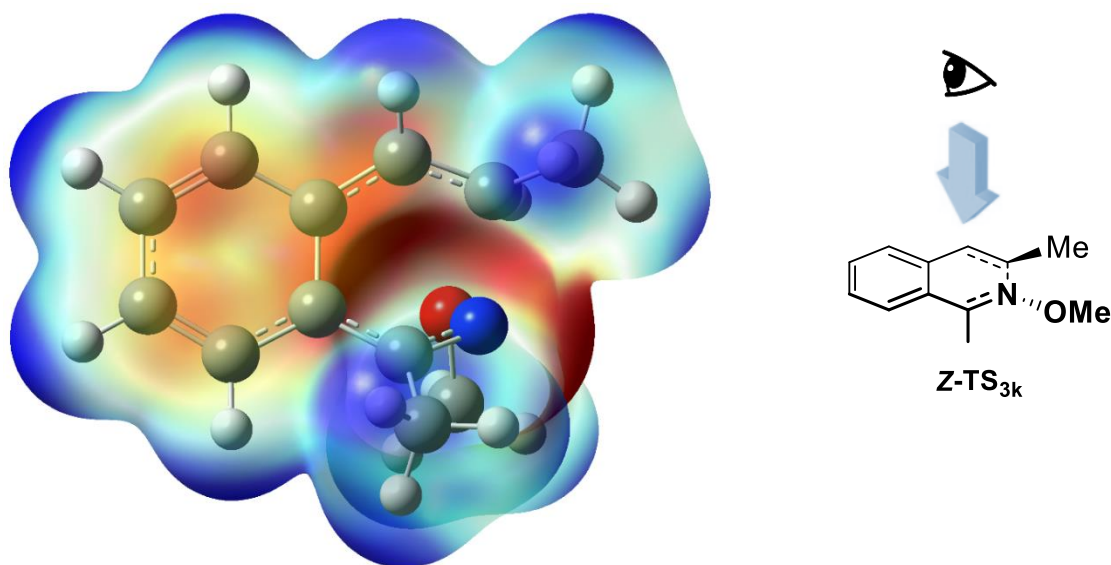


Figure 2.10. Electrostatic potential map of **Z-TS_{3k}** (view from above).

In the case of Figure 2.10, the charge of the aromatic ring is less negative; the negative charge seems to be centered on the oxygen and nitrogen atoms. From this perspective, it is not clear where the negative charge around the heteroatoms is located.

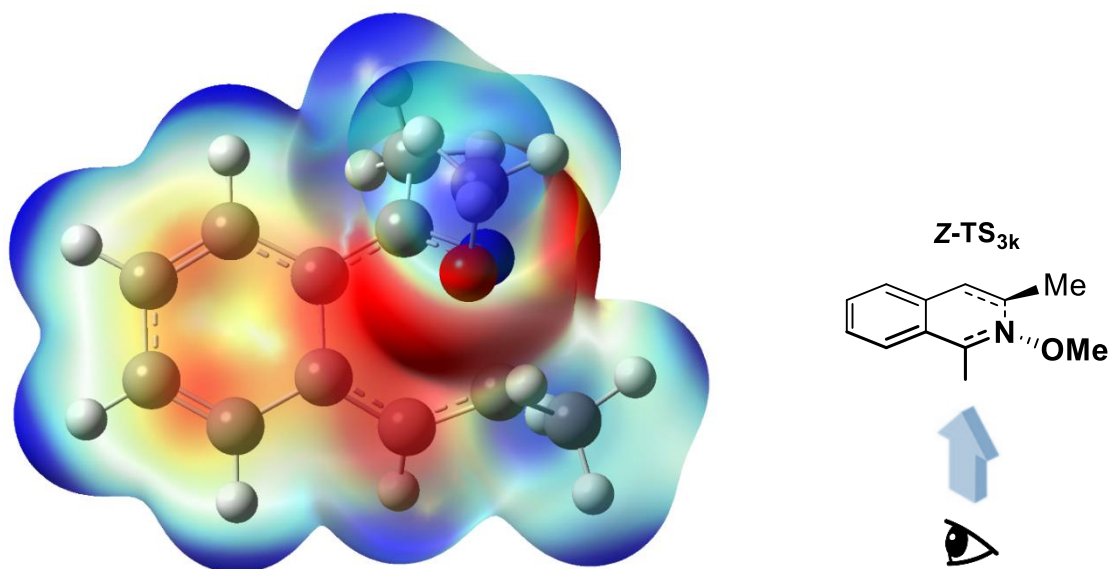


Figure 2.11. Electrostatic potential map of **Z-TS_{3k}** (view from below).

A similar picture is obtained in the perspective of Figure 2.11. The strong negative charge area under the oxygen are probably the lone pairs of the oxygen, but we can also see a small, but very intense negative charge area on the right of the nitrogen atom.

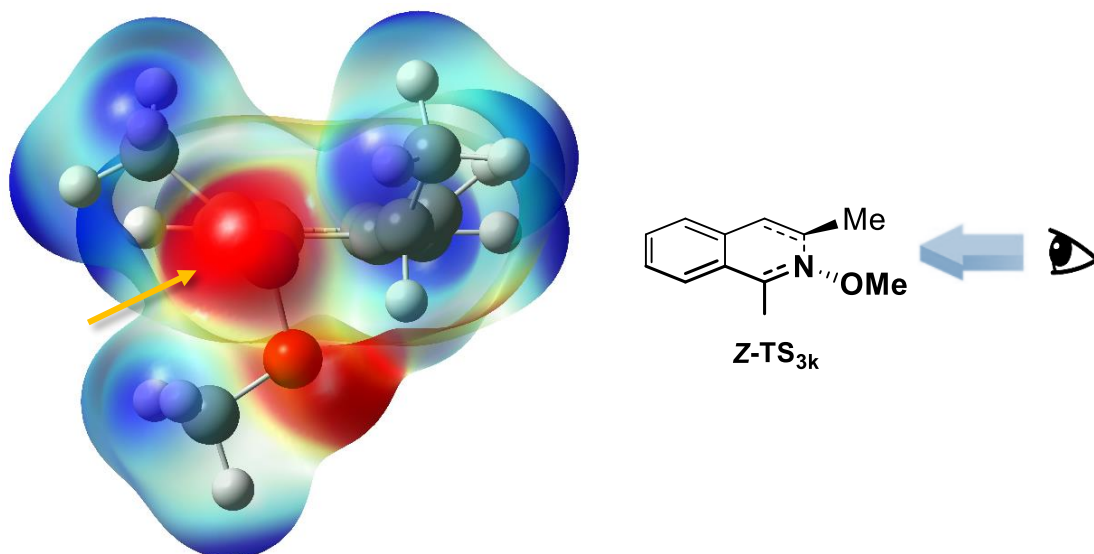


Figure 2.12. Electrostatic potential map of **Z-TS_{3k}** (view from the side).

The last perspective (Figure 2.12) is very enlightening. The negative charge of the lone pairs of the oxygen can be seen, as happened with the *E*-transition state, but we can also observe a separate area of intense negative charge (yellow arrow). This negative charge is located at the nitrogen of the oxime, and is caused by the lone electron pair of the nitrogen.

Actually, we should see the lone pair of the nitrogen in the *E*-transition state as well. The nitrogen of the oxime should have a sp^2 hybridization, where the p_z orbital is the one participating in the electrocyclization. In Figure 2.13, the theoretically expected conformation is displayed.

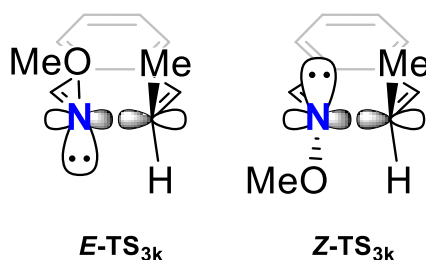


Figure 2.13. Theoretical representation of the expected symmetry for the 6π -electrocyclization of **3k**.

If we look at the *Z*-transition state in Figure 2.12, with the same perspective as the above representation, we can see that the position of the charges makes perfect sense, as the lone pair of the nitrogen is perfectly visible. However, if we examine Figures 2.7, 2.8 and 2.9, corresponding to the *E*-transition state, the lone pair of the nitrogen is nowhere to be found.

Taking these differences into consideration, we propose that the mechanisms for the *E/Z* transition states are not exactly the same. The lone pair of the nitrogen seems to

play a crucial role in the outcome of the reaction, but according to our proposal, only in the case of the *E*-conformation of the oxime (Figure 2.14).

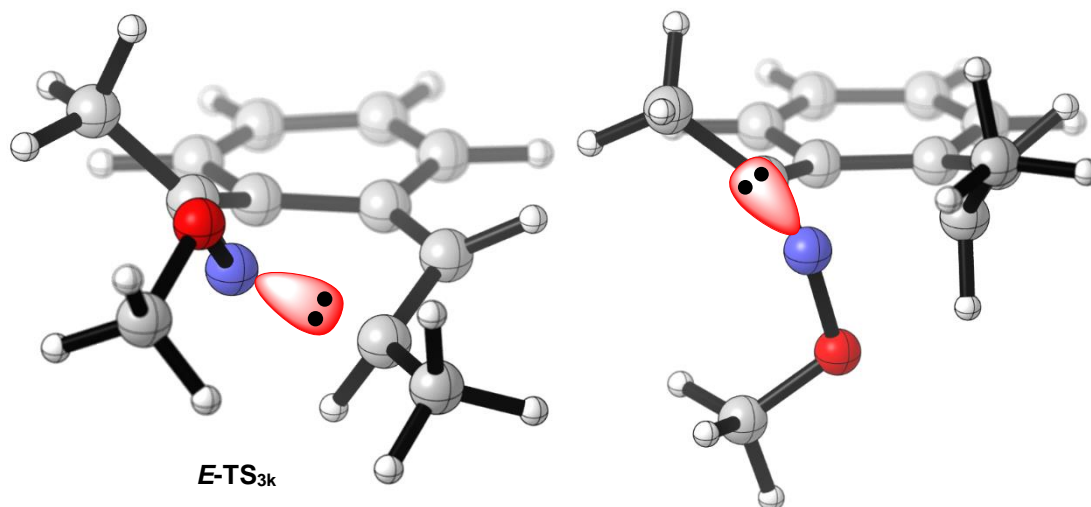


Figure 2.14. Proposed interaction of the lone pair of the nitrogen in the 6π -electrocyclizations of **3k**.

In order to strengthen our hypothesis, we decided to measure and compare further structural characteristics of *E* and *Z*-transition states (Table 2.5). Firstly, we measured the length of the σ -bond that is being formed (δ_{N-C}), expecting to find significantly different values for each configuration of the oxime. Secondly, we measured a key angle, formed by the oxygen atom, the nitrogen atom, and the carbon atom that is forming the σ -bond (θ_{O-N-C}). If our hypothesis regarding the role of the lone pair of the nitrogen is correct, the angle θ_{O-N-C} should be close to 90° in the case of the *Z*-oximes, since the nitrogen has a trigonal planar geometry, and only the p_z orbital (perpendicular to that plane) is participating in the formation of the σ -bond. On the contrary, in the case of the *E*-oximes, the angle θ_{O-N-C} should be closer to 120° , as the lone pair is embedded in the new σ -bond axis.

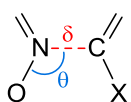


Table 2.5. Bond lengths and angles measured for different *E* and *Z*-transition states.

	3a		3j		3k		3m	
	TS_{3a}		TS_{3j}		TS_{3k}		TS_{3m}	
	<i>E</i>	<i>Z</i>	<i>E</i>	<i>Z</i>	<i>E</i>	<i>Z</i>	<i>E</i>	<i>Z</i>
$\delta_{\text{N-C}}$	1.94 Å	2.01 Å	1.91 Å	1.96 Å	1.90 Å	1.94 Å	1.90 Å	1.94 Å
$\theta_{\text{O-N-C}}$	127.7 °	93.3 °	126.7 °	95.4 °	123.8 °	90.2 °	123.4 °	95.0 °

The difference between *E* and *Z*-transition states are very consistent across the table. The bond lengths are always 0.4-0.5 Å longer in the case of the *Z*-transition states. Besides, the results obtained for $\theta_{\text{O-N-C}}$ are in perfect agreement with our hypothesis. The angles for the *E*-transition states are between 123.4 ° and 127.7 °, while the *Z*-transition states have values between 90.2 ° and 95.4 °, just as predicted.

2.4 Conclusions

The DFT calculations conducted on the 6π -electrocyclization of oximes accurately reproduced the experimentally observed stereodivergent reactivity. *Z*-oximes afforded extremely high activation barriers, while *E*-oximes proceeded through feasible activation barriers. The results were consistent through all the computed examples, from simple linear hexatrienes to bulky aromatic structures.

Our studies on the structure and charge distribution of the transition states permitted us to rationalize this behavior. Thanks to the electrostatic potential surfaces we plotted, the intervention of the lone pair of the nitrogen during the *E*-transition states could be demonstrated. The measured structural features support this hypothesis as well.

The differences found between the *E* and *Z*-configurations of oximes lead us to believe that the mechanisms they proceed through are considerably different. In the next chapter, we will further investigate this matter.

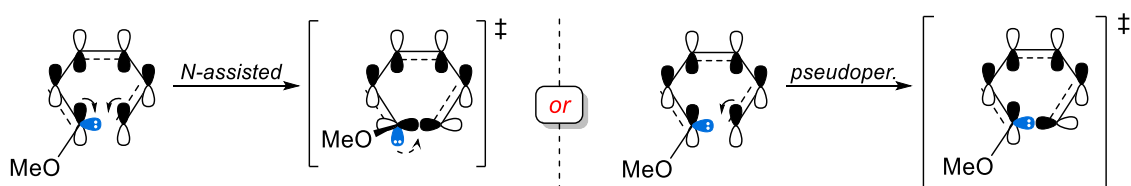
2.5 References

- (1) Mora-Radó, H.; Bialy, L.; Czechtizky, W.; Méndez, M.; Harrity, J. P. A. An Alkyne Diboration/6 π -Electrocyclization Strategy for the Synthesis of Pyridine Boronic Acid Derivatives. *Angew. Chem.* **2016**, *128*, 5928–5930.
- (2) Parsons, W. J.; Ramkumar, V.; Stiles, G. L. The New Cardiotonic Agent Sulmazole Is an A1 Adenosine Receptor Antagonist and Functionally Blocks the Inhibitory Regulator, Gi. *Mol. Pharmacol.* **1988**, *33*, 441–448.
- (3) Biesecker, L. G.; Edwards, M.; O'Donnell, S.; Doherty, P.; MacDougall, T.; Tith, K.; Kazakin, J.; Schwartz, B. Clinical Report: One Year of Treatment of Proteus Syndrome with Miransertib (ARQ 092). *Mol. Case Stud.* **2020**, *6*, 9.
- (4) Marcade, M.; Bourdin, J.; Loiseau, N.; Peillon, H.; Rayer, A.; Drouin, D.; Schweighoffer, F.; Désiré, L. Etazolate, a Neuroprotective Drug Linking GABA_A Receptor Pharmacology to Amyloid Precursor Protein Processing. *J. Neurochem.* **2008**, *106*, 392–404.
- (5) Khaybullina, D.; Patel, A.; Zerilli, T. Riociguat (Adempas): A Novel Agent for the Treatment of Pulmonary Arterial Hypertension and Chronic Thromboembolic Pulmonary Hypertension. *Drug Forecast* **2014**, *39*, 749–758
- (6) Walczyński, K.; Zuiderveld, O. P.; Timmerman, H. Non-Imidazole Histamine H₃ Ligands. Part III. New 4-N-Propylpiperazines as Non-Imidazole Histamine H₃-Antagonists. *Eur. J. Med. Chem.* **2005**, *40*, 15–23.
- (7) Thoma, G.; Veenstra, S.; Strang, R.; Blanz, J.; Vangrevelinghe, E.; Berghausen, J.; Lee, C. C.; Zerwes, H.-G. Orally Bioavailable Syk Inhibitors with Activity in a Rat PK/PD Model. *Bioorg. Med. Chem. Lett.* **2015**, *25*, 4642–4647.
- (8) Reviews on electrocyclizations: (a) Beaudry, C. M.; Malerich, J. P.; Trauner, D. Biosynthetic and Biomimetic Electrocyclizations. *Chem. Rev.* **2005**, *105*, 4757–4778. (b) Vicario, J. L.; Badia, D. Enantioselective 6 π Electrocyclizations: Pushing the Limits in Organocatalytic Pericyclic Reactions. *ChemCatChem* **2010**, *2*, 375–378. (c) Thompson, S.; Coyne, A. G.; Knipe, P. C.; Smith, M. D. Asymmetric Electrocyclic Reactions. *Chem. Soc. Rev.* **2011**, *40*, 4217–4231.
- (9) Vargas, D. F.; Larghi, E. L.; Kaufman, T. S. The 6 π -Azaelectrocyclization of Azatrienes. Synthetic Applications in Natural Products, Bioactive Heterocycles, and Related Fields. *Nat. Prod. Rep.* **2019**, *36*, 354–401.
- (10) Colabroy, K. L.; Begley, T. P. The Pyridine Ring of NAD Is Formed by a Nonenzymatic Pericyclic Reaction. *J. Am. Chem. Soc.* **2005**, *127*, 840–841.
- (11) Choshi, T.; Kumemura, T.; Nobuhiro, J.; Hibino, S. Novel Synthesis of the 2-Azaanthraquinone Alkaloid, Scorpinone, Based on Two Microwave-Assisted Pericyclic Reactions. *Tetrahedron Lett.* **2008**, *49*, 3725–3728.
- (12) Hirose, Y.; Tsuchikawa, H.; Kobayashi, T.; Katsumura, S. Total Syntheses of Zwitterionic Indole Alkaloids, Flavocarpine and Dihydrovincarpine, by Extended Method for Substituted Pyridine Synthesis through Azaelectrocyclization. *Heterocycles* **2015**, *90*, 150–156.
- (13) Tazaki, Y.; Tsuchiya, Y.; Choshi, T.; Nishiyama, T.; Hatae, N.; Nemoto, H.; Hibino, S. The First Total Synthesis of the Antiplasmodial Alkaloid (\pm)-Cassiarin C Based on

- a Microwave-Assisted Thermal Azaelectrocyclic Reaction. *Heterocycles* **2014**, *89*, 427–435.
- (14) Simonetti, S. O.; Larghi, E. L.; Bracca, A. B. J.; Kaufman, T. S. Synthesis of the Unique Angular Tricyclic Chromone Structure Proposed for Aspergillitine, and Its Relationship with Alkaloid TMC-120B. *Org. Biomol. Chem.* **2012**, *10*, 4124–4134.
- (15) Meketa, M. L.; Weinreb, S. M.; Nakao, Y.; Fusetani, N. Application of a 6π -1-Aza-triene Electrocyclization Strategy to the Total Synthesis of the Marine Sponge Metabolite Ageladine A and Biological Evaluation of Synthetic Analogues. *J. Org. Chem.* **2007**, *72*, 4892–4899.
- (16) Miyake, F. Y.; Yakushijin, K.; Horne, D. A. Biomimetic Synthesis of Grossularines-1. *Angew. Chem. Int. Ed.* **2005**, *44*, 3280–3282.
- (17) Fujita, S.; Sakaguchi, T.; Kobayashi, T.; Tsuchikawa, H.; Katsumura, S. Total Synthesis of (-)-Hippodamine by Stereocontrolled Construction of Azaphenalene Skeleton Based on Extended One-Pot Asymmetric Azaelectrocyclization. *Org. Lett.* **2013**, *15*, 2758–2761.
- (18) (a) Abu Ali, H.; Dembitsky, V. M.; Srebnik, M. *Contemporary Aspects of Boron: Chemistry and Biological Applications*; Abu Ali, H., Ed.; Studies in Inorganic Chemistry; Elsevier: Amsterdam, 2005; Vol. 22. (b) Hall, D. G. *Boronic Acids: Preparation and Applications in Organic Synthesis and Medicine*, Reprint; Wiley-VCH: Weinheim, 2006. (c) Miyaura, N. Metal-Catalyzed Reactions of Organoboronic Acids and Esters. *Bull. Chem. Soc. Jpn.* **2008**, *81*, 1535–1553.
- (19) Mkhaliid, I. A. I.; Barnard, J. H.; Marder, T. B.; Murphy, J. M.; Hartwig, J. F. C–H Activation for the Construction of C–B Bonds. *Chem. Rev.* **2010**, *110*, 890–931.
- (20) (a) Chong, E.; Blum, S. A. Aminoboration: Addition of B–N σ Bonds across C–C π Bonds. *J. Am. Chem. Soc.* **2015**, *137*, 10144–10147. (b) Faizi, D. J.; Issaian, A.; Davis, A. J.; Blum, S. A. Catalyst-Free Synthesis of Borylated Lactones from Esters via Electrophilic Oxyboration. *J. Am. Chem. Soc.* **2016**, *138*, 2126–2129.
- (21) (a) Gandon, V.; Leboeuf, D.; Amslinger, S.; Vollhardt, K. P. C.; Malacria, M.; Aubert, C. Chemo-, Regio-, and Stereoselective Cobalt-Mediated [2+2+2] Cycloaddition of Alkynyl Boronates to Alkenes: 1,3- and 1,4-Diboryl-1,3-cyclohexadienes. *Angew. Chem. Int. Ed.* **2005**, *44*, 7114–7118. (b) Wang, H.; Grohmann, C.; Nimphius, C.; Glorius, F. Mild Rh(III)-Catalyzed C–H Activation and Annulation with Alkyne MIDA Boronates: Short, Efficient Synthesis of Heterocyclic Boronic Acid Derivatives. *J. Am. Chem. Soc.* **2012**, *134*, 19592–19595.

Chapter 3.

6 π -Electrocyclizations of Oxime Ethers: Mechanistic Insights



In this chapter, we carried out further mechanistic investigations on the 6 π -electrocyclization of oxime ethers. The role of the lone pair of the nitrogen atom during the transition state has been assessed for both *E* and *Z*-oximes. The possibility of the reaction being pseudopericyclic (and not purely pericyclic) was considered. Therefore, studies on the orbitals and aromaticity of the transition states were conducted, using simple oximes and similar structures as model systems.

Chapter based on the publication:

[2] Sotorríos, L.; Harrity, J. P. A.; Gómez-Bengoia, E. Aromaticity Studies on the Electrocyclization of Imines and Oxime Ethers (Provisional title). *Manuscript in preparation*.

3.1 Context

3.1.1 Introduction

To the best of our knowledge, the mechanism of the 6 π -electrocyclization of oximes remains unexplored. Nevertheless, some mechanistic studies have been carried out on similar structures in the context of pseudopericyclic reactions. The similarity of these reactions to our oximes encouraged us to study the mechanism in more depth.

3.1.2 Pseudopericyclicity

In 1969, Robert B. Woodward and Roald Hoffman devised a set of rules to understand and predict the outcome of pericyclic processes.¹ These rules, based on the conservation of orbital symmetry, were established as a reliable method to discern whether a pericyclic reaction occurs under thermal or photochemical conditions, as well as determine the stereochemistry of the resulting product.

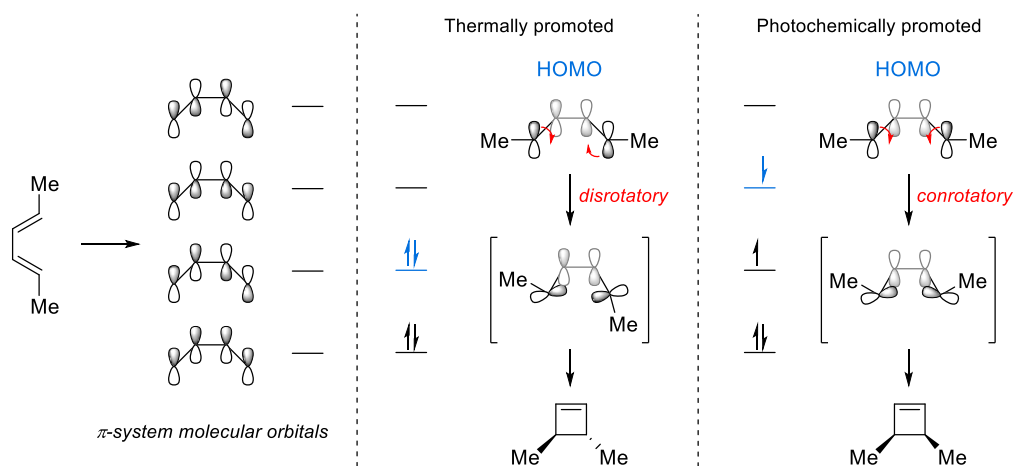


Figure 3.1. Illustration of the Woodward-Hoffmann rules for the thermal and photochemical electrocyclization of methyl substituted 1,3-butadiene.

In 1976, Lemal et al. discovered an automerization reaction that seemed to disobey the Woodward-Hoffman rules.² Their experimental study was focused on the mechanism of the walk rearrangement of perfluorotetramethyl (Dewar thiophene) *exo-S*-oxide, PFDTSO (Figure 3.2); a [1,3] sigmatropic rearrangement observed at temperatures as low as -95 °C.

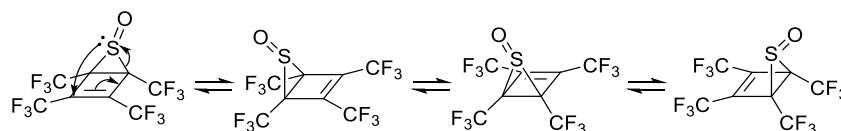


Figure 3.2. Walk rearrangement of PFDTSO.

To explain the high reactivity of this substrate, they proposed the mechanism in Figure 3.2, defining a new type of process, the pseudopericyclic reaction; “A *pseudopericyclic reaction* is a concerted transformation whose primary changes in bonding encompass a cyclic array of atoms, at one (or more) of which nonbonding and bonding atomic orbitals exchange their roles. (...) the role interchange means a “disconnection” in the cyclic array of overlapping orbitals because the atomic orbitals switching functions are mutually orthogonal”.² Although the reaction used by Lemal to define pseudopericyclicity was later proved pericyclic,³ his initial definition remains.

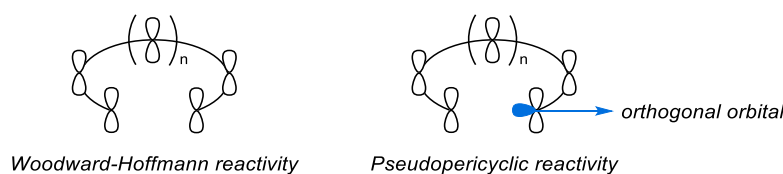


Figure 3.3. Graphical representation of the orbitals participating in purely pericyclic reactions vs pseudopericyclic reactions. Adapted from ref. 15.

The transition states of pericyclic reactions are aromatic due to the π -orbital array. On the other hand, the orthogonal orbital of pseudopericyclic systems causes a “disconnection” in this orbital array. This prevents the electrons from circulating through the π -system of the ring, making the transition state non-aromatic (Figure 3.4).

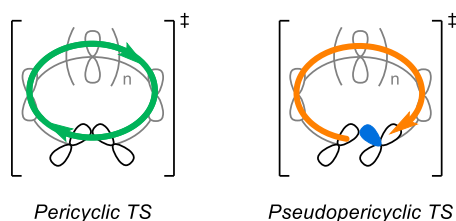
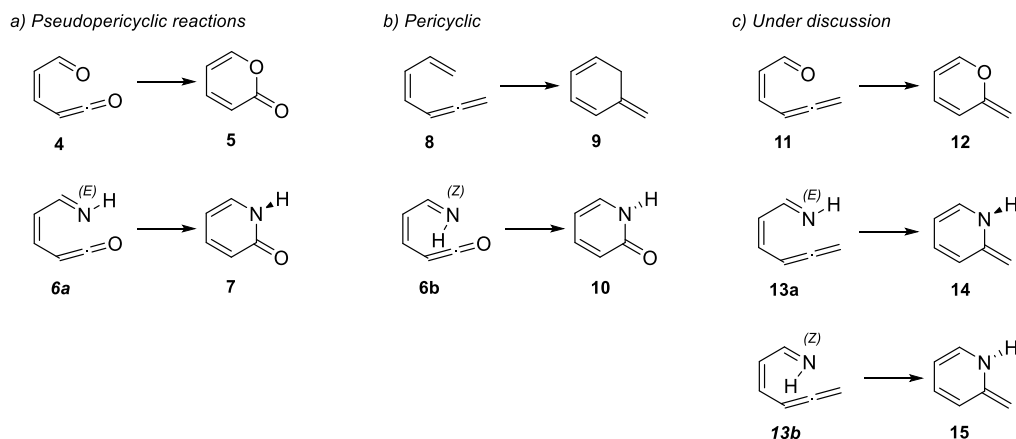


Figure 3.4. Transition states of a pericyclic and pseudopericyclic reaction. The arrows represent the circulating electrons.

3.1.3 Electrocyclization of allenes and ketenes

For almost twenty years, the work of Lemal et al. remained unnoticed, until Birney⁴ and other authors⁵⁻⁸ discovered and described several pseudopericyclic reactions. Some of the explored reactions drew our attention, as their computational studies delivered differences between *E*- and *Z*-configurations, similarly to our oximes.^{9c} A set of allenes and ketenes have been studied by Rodríguez-Otero and Cabaleiro-Lago,⁹ Cossío and de

Lera,¹⁰ Duncan¹¹ and others,¹²⁻¹⁵ with considerable differences in terms of geometric structures, orbital interactions and activation energies.



Scheme 3.1. Previously related reactions studied by means of computational methods.

The case of ketene-imine **6** is very significant (Scheme 3.1). While the *E*-isomer (**6a**) proceeds through a pseudopericyclic transition state, the mechanism of the *Z*-isomer (**6b**) is pericyclic, just as its all carbon counterpart **8**.^{9c} We speculate that this could also be the case of our oxime ethers.

In the case of allenes, four orbital interactions are possible (left, Figure 3.5). Model A would correspond to a purely pericyclic reaction, as the participating orbitals are both π -orbitals. The remaining models B, C and D correspond to a pseudopericyclic array, since at least one of the participating orbitals is orthogonal. In our case, the only orbital that could produce an orthogonal interaction is the lone pair of the nitrogen (right, Figure 3.5). In the previous chapter, we concluded that due to its apparent position and orientation, the lone pair was possibly participating in the reaction in the case of *E*-oximes. Therefore, we believe that the pseudopericyclic array is fairly plausible.

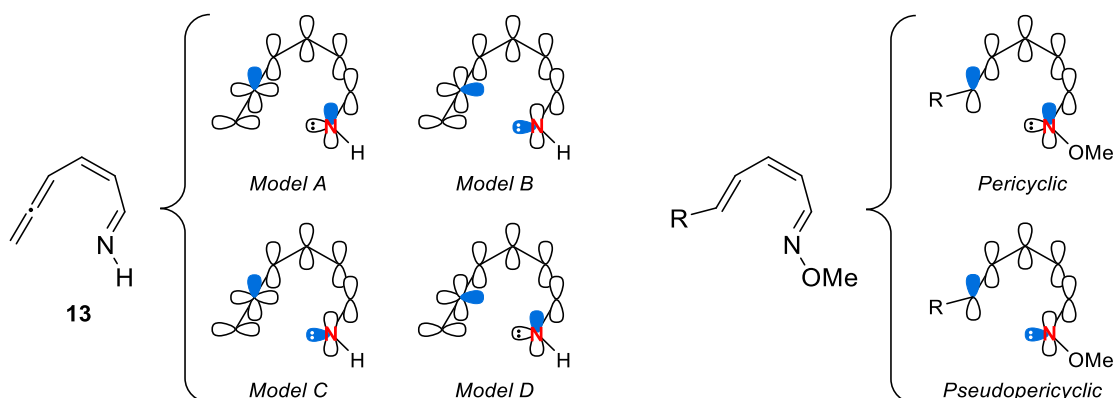
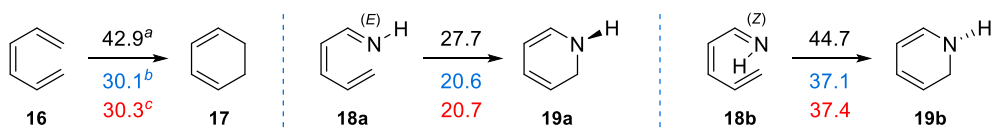


Figure 3.5. Graphical representation of the possible orbital interactions for allene **13** (left, adapted from ref. 11a) and oxime ethers (right). The orbitals in blue represent the participating orbitals for each model. Model A is the only pericyclic alternative for allenes; models B, C and D correspond to pseudopericyclic mechanisms.

3.1.4 6π -electrocyclization of nitrogen containing hexatrienes; pericyclic or pseudopericyclic?

The only electrocyclization of a nitrogen containing hexatriene that has been computationally studied is that of (*Z*)-penta-2,4-dien-1-imine (**18**, Scheme 3.2). In the nineties, experimental evidences showed that the reaction of 1-azatrienes was faster than that of hexatrienes,¹⁶ and a couple of computational investigations on the matter were carried out.^{17,18} These computational studies revealed big differences between the activation energies of *E* and *Z*-imines (Scheme 3.2). The reaction of **16** presents somewhat high barriers, while the barriers of the reaction of *E*-imine **18a** are considerably lower. Interestingly, the barriers of *Z*-imine **18b** were remarkably higher, even more than those of **16**. According to the authors, the low barriers of **18a** were caused by the participation of the lone pair of the nitrogen, as we suggested in the previous chapter.



Scheme 3.2. Activation barriers obtained by various authors in kcal/mol. ^aActivation potential energies by Houk et al., B3LYP/6-31G(d). ^bZero-point energy (ZPE) corrected energies by Rodríguez-Otero, B3LYP/6-31G(d). ^cZPE corrected enthalpies by Duncan et al., B3LYP/6-31G(d).

The pseudopericyclicity of the reaction was never mentioned by Houk et al.,¹⁸ while Rodríguez-Otero¹⁷ stated that the reaction was non-pseudopericyclic, due to the lack of planarity of the transition state (common characteristic of pseudopericyclic reactions, as proved by Birney). Years later, Duncan et al.^{11a} performed complete active space self-consistent field (CASSCF) calculations on the cyclizations of **13a**, **13b**, **16**, **18a** and **18b** (Figure 3.6). From his study on the molecular orbitals, he concluded that the reactions of imine **18a** and allene **13a** were likely to proceed in a somewhat pseudopericyclic manner. To his understanding, the planarity of the reaction can only be achieved when the mechanism follows Model B (Figure 3.6); this is impossible for imine **18a** (there is no orthogonal orbital available) and not the case for allene **13a**, whose transition state resembled that of Model C. Actually, the mechanism corresponding to Model A could be achieved by fixing the structure, but the transition state was 6.8 kcal/mol higher in energy than that of Model C, meaning that the reaction would not proceed through it.

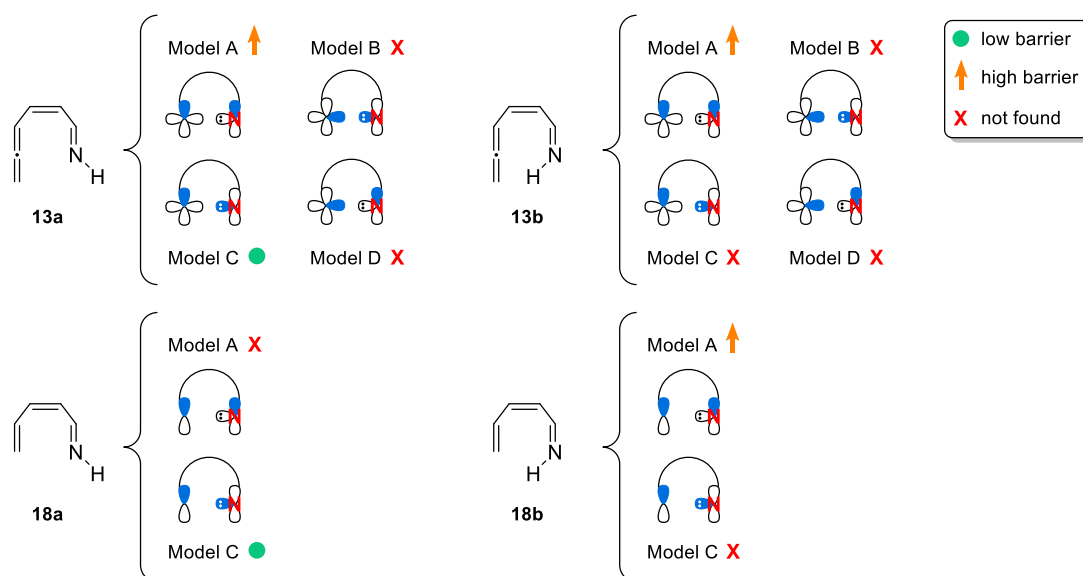


Figure 3.6. Models for the electrocyclization of *E* and *Z*-isomers of ketene-imine **13** and imine **18**, as described by Duncan.^{11a}

On the other hand, the transition state of *Z*-configurations **13b** and **18b** resembled their all-carbon counterparts more than they resembled the *E*-configurations. Thus, they followed Model A, and were considered purely pericyclic.

The classification of these and similar reactions still remains a controversial matter. Besides, none of the mentioned studies were ever applied to oximes and/or oxime ethers.

3.2 Computational approach

3.2.1 Objective

The reactivity of oxime ethers has never been considered in the works mentioned in the introduction, nor has the aromaticity of imines been explored. We believe that studying the aromaticity of our oxime ethers could help us discern the reaction mechanism and shed some light into the experimentally observed selectivities regarding the configuration of the substrate's oxime ether. In this regard, we applied a few methodologies previously used in the analysis of pseudopericyclic reactions as the aforementioned alkenes and ketenes. These methods were: calculation of the Natural Localized Molecular Orbitals (NLMO), study of the Nucleus-Independent Chemical Shifts (NICS) indexes, and representation of the electron delocalization with the Anisotropy of the Induced Current Density (AICD or ACID) method.

3.2.2 Computational methods

For references and a more detailed description of the methodology, levels of theory and software please see chapter 1.

All the structures shown in the present work were optimized using DFT as implemented in Gaussian09. When necessary, conformational studies were performed in both starting materials and transition states. The stationary points were characterized by frequency calculations in order to verify that they have the right number of imaginary frequencies. Most of the calculations were carried out in the level of theory M06-2X/6-311+G(d,p). Solvation factors were introduced with the IEF-PCM method, using toluene as solvent.

Since the pseudopericyclic reaction of **4** proceeded without energy barrier, the transition state could not be located in the aforementioned theory level. Around 20 different combinations of functionals and basis sets were tested, but only the Hartree-Fock method with the basis set 6-31G(d,p) delivered the transition state **TS_{4,5}**, as found in the bibliography.^{9b}

Reaction **6a** was also barrierless for all the tested theory levels; therefore, no transition state could ever be located.

3.2.2.1 Natural Localized Molecular Orbitals (NLMO)

The analysis of the NLMO was performed with the 3.1 version of the NBO package, as implemented in Gaussian09. The employed theory level was M06-2X/6-311+G(d,p), with toluene as solvent.

3.2.2.2 Nucleus-Independent Chemical Shifts (NICS)

NMR shielding tensors were calculated using the gauge-independent atomic orbital (GIAO) method, as implemented in Gaussian09, after performing intrinsic reaction coordinate (IRC) calculations. The utilized level of theory was M06-2X/6-311+G(d,p), using the implicit solvent model IEF-PCM (solvent = toluene).

The NICS index was originally computed at the center of the ring, as described by Schleyer.¹⁹ Nowadays the NICS index is preferably computed at the ring critical point (3,+1) as defined by Bader's "*Theory of Atoms in Molecules*".²⁰ Due to the lack of computational software to calculate the ring critical point, the geometrical center of the molecule was chosen. Nevertheless, the NICS indexes obtained with this methodology for the reaction of **4** were identical to those found in the literature.^{9b} Therefore, this methodology was employed for all the remaining substrates.

The NICS indexes calculated correspond to NICS(0)_{iso}. Since the analyzed structures were not planar, defining the Z-axis in order to calculate the anisotropic shielding was a complicated matter. For this reason, and to be able to compare our data with the literature, we decided to use the isotropic shielding values.

Because the transition state of **6a** could not be located, no IRC could be computed either. In order to calculate the NICS indexes, several optimizations were carried out fixing the distance between the atoms involved in the new σ -bond (N1 and C6). Then, the NICS indexes were calculated in the center of each structure.

3.2.2.3 Anisotropy of the Induced Current Density (ACID)

The ACID software was used in several transition states to visualize the delocalized electron density as an isosurface (version 2.0.0). The necessary input for the ACID software was obtained calculating the NMR shielding tensors using continuous set of gauge transformations (CSGT) method as implemented in Gaussian09 (using the Internal Option IOp(10/93=1)).

The magnetic field was always perpendicular to the plane of the figures. Two types of representations will be displayed; the density isosurface on its own and the isosurface plus the current density vectors. The pictures only displaying isosurface were plotted at

an isovalue of 0.05 with 40 000 gridpoints. The pictures contacting vectors were plotted at the same isosurface value, but with 160 000 gridpoints. In order to visualize the vectors more clearly, the isosurface was smoothed and the option `maxarrow=1.5` was used, to prevent the representation of exceedingly long isolated vectors.

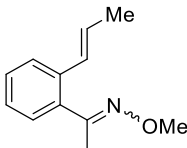
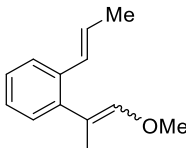
Pictures were generated with the Persistence of Vision Ray Tracer (POV-Ray).

3.3 Results and discussion

3.3.1 Preliminary studies

Since our previous calculations suggest that the lone pair of the nitrogen is critical for the reactivity, we investigated the reaction with a carbon atom instead of a nitrogen (**3n**). With no lone pair taking part in the reaction, we envisaged a bigger resemblance between the *E* and *Z*-transition states.

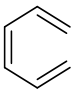
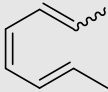
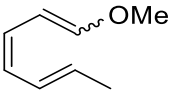
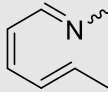
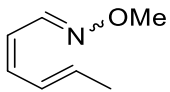
Table 3.1. Activation barriers obtained for oxime **3k** and his carbon-containing counterpart, **3n**.

	 3k		 3n	
	<i>E</i> -TS _{3k}	<i>Z</i> -TS _{3k}	<i>E</i> -TS _{3n}	<i>Z</i> -TS _{3n}
ΔG^\ddagger (kcal/mol)	32.5	55.7	40.0	42.9

Indeed, the activations energies of **E-3n** and **Z-3n** are very close in energy. While the energy gap between the two configurations of **3k** was of 23.2 kcal/mol, the energy difference between **E-TS_{3n}** and **Z-TS_{3n}** is of only 2.9 kcal/mol. Nevertheless, both *E* and *Z*-activation energies of **3n** are very high in energy, with their reaction times being of the order of years, highlighting the crucial role of the nitrogen atom.

We decided to compute a few more examples, with simpler molecules, in order to strengthen our hypothesis. We searched for the *E* and *Z*-transition states for simple hexatrienes with different functionalities, and compared their activation Gibbs free energies in Table 3.2.

Table 3.2. Models used for the study of the mechanism. Activation energies in kcal/mol.

	 16	 20		 21		 22		 23	
	TS ₁₆	<i>E</i> -TS ₂₀	<i>Z</i> -TS ₂₀	<i>E</i> -TS ₂₁	<i>Z</i> -TS ₂₁	<i>E</i> -TS ₂₂	<i>Z</i> -TS ₂₂	<i>E</i> -TS ₂₃	<i>Z</i> -TS ₂₃
ΔG^\ddagger	30.4	32.0	35.9	30.6	37.5	22.4	47.4	25.4	48.1

The most basic hexatriene (**16**) has a fairly high activation energy of 30.4 kcal/mol. Adding one methyl group to each terminal alkene (**20**) increases the energy barrier, especially in the case of the *Z*-transition state, **Z-TS₂₀**. The energy difference between the *E* and *Z*-transition states of **20** is of 3.9 kcal/mol, while in the methoxy containing substrate **21** this difference is slightly larger, of 6.9 kcal/mol. In both cases, the energies for the *Z*-transition states are considerably high and require substantial heating to proceed in reasonable times. Nevertheless, the differences between each configuration are not as large as those of our previously studied oximes were.

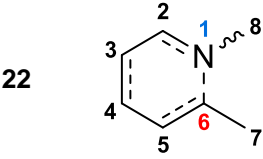
When a nitrogen atom was added to the substrates, the difference between the *E* and *Z*-substrates became remarkably higher. In the case of imine **22**, the *Z*-configuration lead to an activation barrier 25.0 kcal/mol higher. Similarly, the activation energy difference between the two configurations of oxime ether **23** was of 22.7 kcal/mol. Both *E*-transition states are feasible while the *Z*-transition states are too high to proceed even with heating. This suggests that steric or electronic effects alone are not causing the large energy differences and supports our hypothesis of two different mechanisms for each oxime configuration.

In view of these results, it is clear that the presence of nitrogen is key for the feasibility of the electrocyclizations. We decided to investigate further into the participation of the lone pair of the nitrogen by performing an NLMO analysis.

3.3.2 NLMO

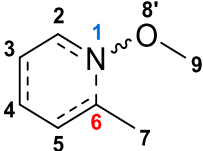
A quick NLMO calculation was performed on imine **22** and oxime **23** in order to check the delocalization of the lone pair of the nitrogen atom in the *E* and *Z*-transition states. In Table 3.3, the first three atoms with larger contributions to the NLMO of the lone pair of imine **22** are shown.

Table 3.3. Atomic contributions for the NLMO of the lone pair of the nitrogen atom, imine **22**.

		Atomic hybrid contributions (lone pair of N1)	
		<i>E</i> -transition state	<i>Z</i> -transition state
		1 : 87.526%	1 : 96.450%
		6 : 5.432%	2 : 0.942%
		5 : 2.156%	8 : 0.578%
	
			6 : 0.097%

The results are very informative and concur with our postulate on the role of the nitrogen's lone pair on the *E*-transition states. In the case of the *E*-transition state of imine **22**, the orbital mostly consists of N1 (87.526%). Nevertheless, the contribution of C5 (2.156%) and especially C6 (5.432%) cannot be neglected. These values mean that the orbital is partially delocalized through the new σ -bond, and thus contributing on its formation. This is in clear opposition with the *Z*-transition state **Z-TS₂₂**, where almost the entirety of the orbital is located at N1 (96.450%). Only small contributions are observed in the two carbon atoms adjacent to N1, C2 (0.942%) and C8 (0.500%). This is a clear indicative of the null participation of the lone electron pair during the transition state of the reaction. As a matter of fact, the contribution of C6 to the orbital during the transition state is of only 0.097%.

Table 3.4. Atomic contributions for the NLMO of the lone pair of the nitrogen atom, oxime ether **23**.

		Atomic hybrid contributions (lone pair of N1)	
		<i>E</i> -transition state	<i>Z</i> -transition state
23		1 : 91.056%	1 : 97.836%
		6 : 4.025%	2 : 0.718%
		5 : 1.838%	3 : 0.393%
	
			6 : 0.246%

Similar conclusions arise from the results of oxime **23** (Table 3.4). The lone pair of N1 is much more delocalized during the *E*-transition state (91.056% **E-TS₂₃** vs 97.836% **Z-TS₂₃**). Nevertheless, the delocalization of the orbital in **E-TS₂₃** is less pronounced than it was on the imine (91.056% **E-TS₂₃** vs 87.526% **E-TS₂₂**). The minor delocalization obtained for **Z-TS₂₃** is distributed differently, as the orbital is not shared with O8', but with C2 and C3. The contribution of C6 is slightly higher than that of imine **Z-TS₂₂** (0.246%), but still negligible when compared to **E-TS₂₃**, where its contribution is 16 times stronger.

After performing the NLMO analysis, we started to investigate the pseudopericyclicity of the reaction analyzing the aromaticity of the transition states. We started computing the NICS indexes.

3.3.3 NICS

3.3.3.1 NICS of imines

Since the delocalization of the nitrogen was more intense in the case of the imines, we decided to start by calculating the NICS indexes of our imine models, **E-22** and **Z-22** (Figure 3.7). We computed the indexes of the purely pericyclic reaction of **16** to later carry out a comparison between them. We also chose substrate **4**, as its cyclization has been previously defined as pseudopericyclic.^{4b}

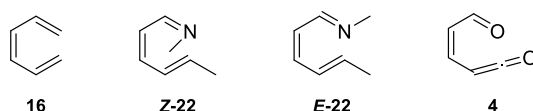


Figure 3.7. Substrates subjected to the calculation of NICS indexes.

As illustrated in the computational methods section, the NICS index was calculated in the transition state as well as through the intrinsic reaction coordinate (IRC) points. The resulting curves are presented in Figure 3.8.

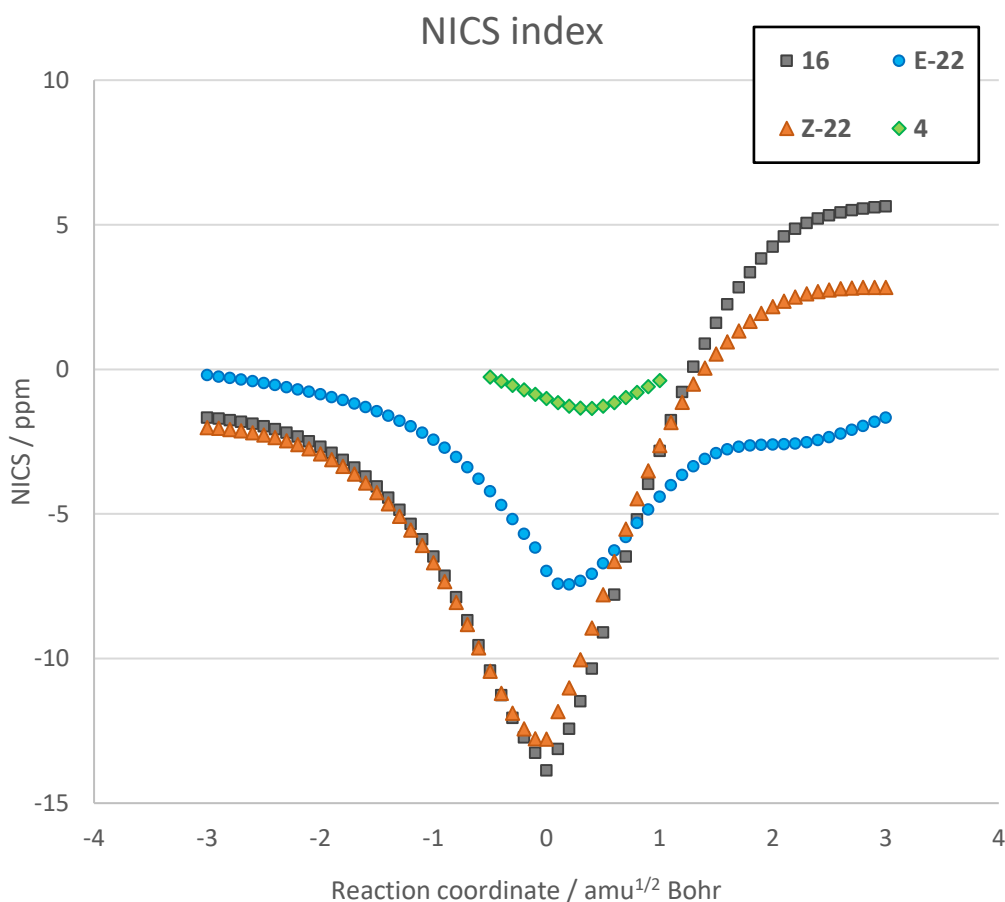


Figure 3.8. Variation of the NICS index through the reaction coordinate, from the reactant (left) towards the product (right). The transition states are located at 0 $\text{amu}^{1/2}$ Bohr. Negative NICS values indicate aromaticity, while positive values stand for antiaromaticity.

Firstly, we will analyze the NICS index profile of the pericyclic reaction of **16** (grey squares, Figure 3.8). The reaction begins with almost no aromaticity, quickly becoming aromatic as the transition state ($0 \text{ amu}^{1/2} \text{ Bohr}$) is approached. The strongest aromaticity is observed at the transition state, with a value of -13.88 ppm . As the reaction proceeds, the aromaticity is lost, reaching a somewhat antiaromatic product.

Now we will look into the pseudopericyclic reaction of **4** (green diamonds). The reaction lacks aromaticity, with its minimum NICS value being -1.35 ppm . This value does not correspond to the transition state, as happened with the pericyclic reaction of **16**, but it is partially shifted towards the product, at a reaction coordinate value of $0.4 \text{ amu}^{1/2} \text{ Bohr}$. It is worth mentioning that, as explained in the computational methods section, the transition state and IRC calculations of this reaction had to be performed in the level of theory HF/6-31G(d,p), as the reaction was barrierless in all the other tested theory levels.

Next, we will analyze the profile of our model imine **Z-22** (orange triangles). The similarity with the profile of **16** is evident; the reaction is slightly less aromatic at the minimum (-12.78 ppm) and the product is less antiaromatic, but the rest of the profile is almost identical. From this, we can infer that the mechanism of both reaction is essentially the same.

Finally, **E-22** was found to bear the most intriguing profile (blue circles). The reaction starts with null aromaticity, just as the pseudopericyclic reaction of **4**, and proceeds to a minimum of -7.44 ppm . This value is obviously much higher than that of **4**, but is also half of that of the pericyclic reaction of **16** and *Z*-imine **Z-22**. In addition, the minimum is not located at the transition state, this is, at $0 \text{ amu}^{1/2} \text{ Bohr}$, but at $0.2 \text{ amu}^{1/2} \text{ Bohr}$, which is again halfway between the pericyclic reaction of **16** ($0 \text{ amu}^{1/2} \text{ Bohr}$) and the pseudopericyclic reaction of **4** ($0.4 \text{ amu}^{1/2} \text{ Bohr}$). Finally, the product is less antiaromatic, and shows a “shoulder” near the end, which was never detected in the other profiles.

A perhaps more fitting comparison could have been done by taking into account the NICS indexes of our model imine with those of molecule **E-6** (right, Figure 3.9) instead of **4**, since it contains a nitrogen atom in the same position as our substrates. As explained in the computational methods, the transition state, and thus, the IRC structures, could not be computed. The NICS indexes had to be computed differently, and a direct comparison could not be made. Nevertheless, a few optimizations were performed, with different N1-C6 distances (which were fixed during the optimization). The resulting graph of the NICS index is displayed in Figure 3.9, along with the relative free energy of each structure.

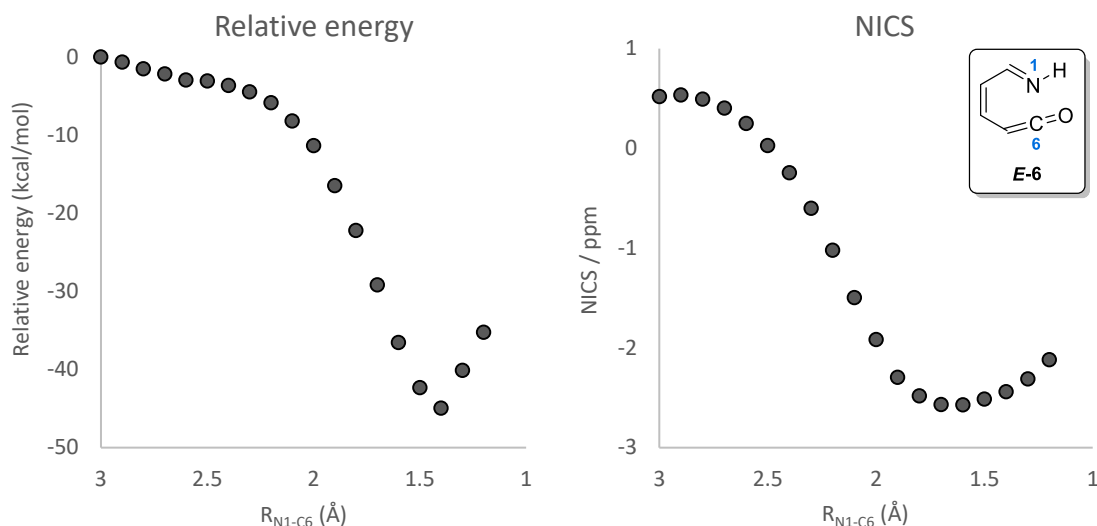


Figure 3.9. Gibbs free energy of the computed structures, related to the structure with $R_{N1-C6} = 3 \text{ \AA}$ (left) and NICS index values (right).

As can be seen in Figure 3.9 (left), there is no energy maximum, and therefore, no transition state. When looking into the NICS index (right), we can observe a minimum value of -2.57 ppm at a $N1-C6$ distance of 1.7 \AA . Thus, we can assume that the reaction of **E-6** is slightly more aromatic than that of **4**, whose NICS index minimum was of -1.35 ppm .

From the results obtained by the study of the NICS index, we can conclude that there is a significant difference in the aromaticity of the *E* and *Z*-transition states of imines. While **Z-22** displays an aromaticity profile almost identical to that of an ordinary pericyclic reaction, the **E-22** shows a very different profile, with a much less aromatic transition state. The profile of **E-22** does not correspond to that of the pseudopericyclic reaction of **4** either, but seems to be somewhere in between both profiles. Actually, since the transition state of the imine containing ketene **E-6** is more aromatic than **4**, the profile of **E-22** would be closer to that of a pseudopericyclic reaction, rather than that of the pericyclic reaction of **16**. Thus, we should consider the reaction of **E-22** to be a hybrid of a pericyclic and a pseudopericyclic process or, at least, a pericyclic process with a very strong pseudopericyclic character. Similar conclusions were reached by Duncan et al. during their work.^{11a}

3.3.3.2 NICS of oximes

The results of the NLMO study showed that the delocalization of the lone pair of the nitrogen was less pronounced in the case of oxime ethers. Thus, we expect a different NICS profile.

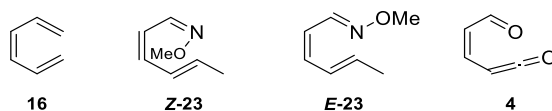


Figure 3.10. Substrates subjected to the calculation of NICS indexes.

We applied the same procedure to the reaction of oximes **E-23** and **Z-23**, comparing them again with substrates **16** and **4** (Figure 3.10). The results are shown in Figure 3.11.

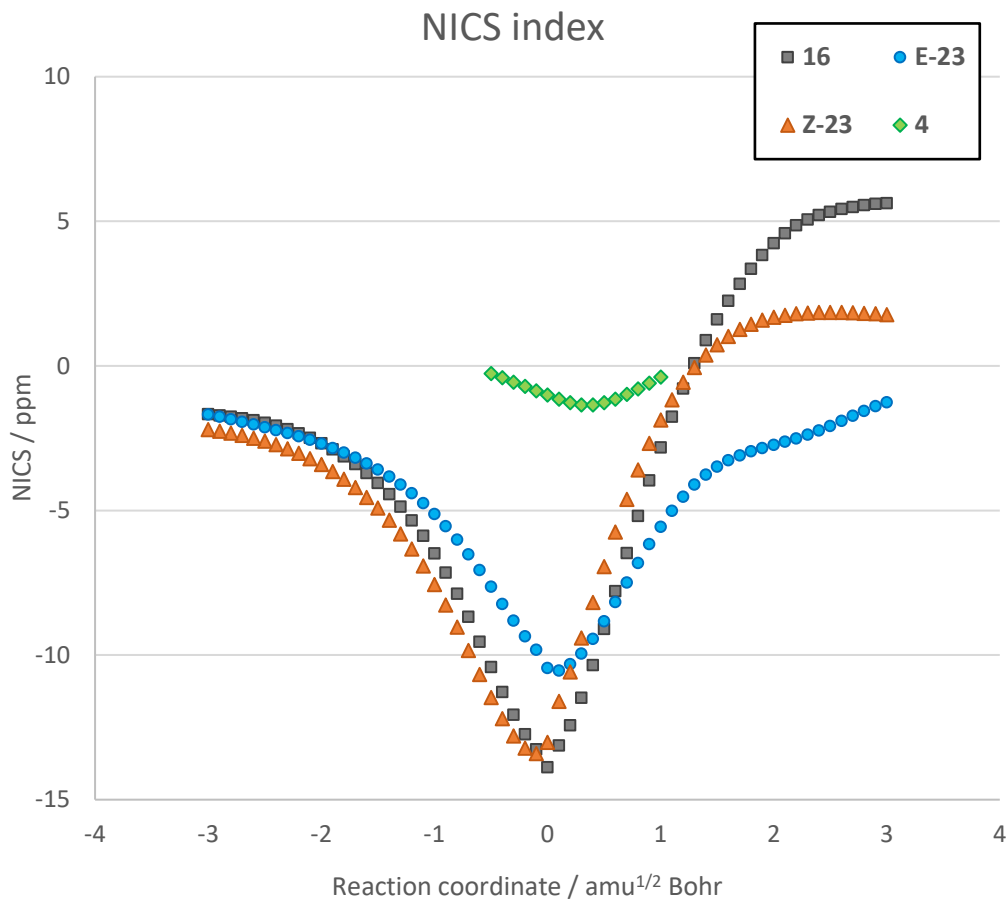


Figure 3.11. Variation of the NICS index through the reaction coordinate, from the reactant (left) towards the product (right). The transition states are located at $0 \text{ amu}^{1/2} \text{ Bohr}$. Negative NICS values indicate aromaticity, while positive values stand for antiaromaticity.

The case of oxime **Z-23** is very similar to that of imine **Z-22**. The profile is almost identical to that of the pericyclic reaction of **16**, except for the lower antiaromaticity of the product. On the other hand, the reaction of **E-23** seems to be considerably less pseudopericyclic than imine **E-22**. The starting material is now to some extent aromatic, just as the *Z*-isomer and the pericyclic reaction. The index minimum lays at $0.1 \text{ amu}^{1/2} \text{ Bohr}$ instead of 0.2 , and has a bigger value of -10.58 ppm . The aromaticity of the product is still similar to that of **E-22**.

The classification of the mechanism of oximes is far more complex than that of imines. In the case of the *Z*-isomer, **Z-23**, the NICS profile is close enough to that of hexatriene **16** to be considered pericyclic. While a clear difference between the *E* and *Z*-

isomers can be observed, it is not so clear whether the mechanism of **E-23** should be considered pseudopericyclic or not.

We believe that for the classification of the reaction as pseudopericyclic, the lack of π -orbital overlapping is a question to be investigated. For this, we decided to use the software ACID, in order to visualize the orbital disconnection and shed some light into this issue.

3.3.4 ACID

As introduced earlier in this chapter, the delocalized electron density and the density current of aromatic rings can be studied and visualized with the software ACID. We intended to apply this method to the already computed transition states, in order to study the nature of the reaction mechanism.

The simplest 6π -electrocyclization (hexatriene **16**) was selected initially. First, the delocalized electron density was plotted, without displaying the current density vectors. We expected to visualize the π -density delocalized through the whole ring.

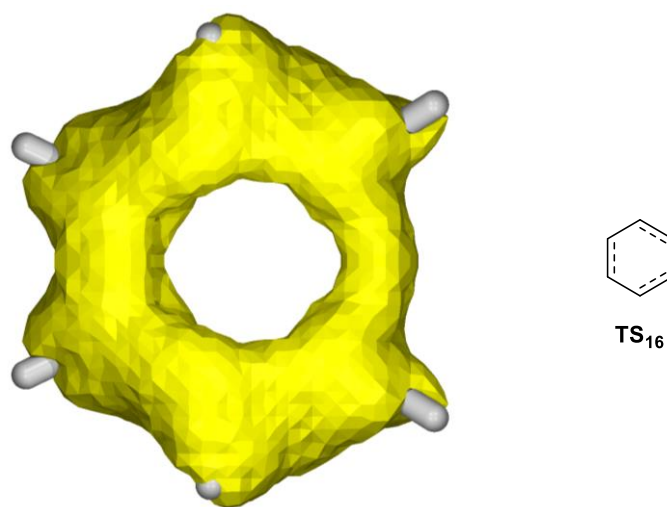


Figure 3.12. ACID plot for the transition state of **16**. Only isosurface is displayed, in yellow. 2D representation on the right.

We can indeed observe the delocalized electron density through the whole system (Figure 3.12), although in the area of the new sigma bond the surface is slightly thinner. In Figure 3.13, the same transition state is displayed, this time including the current density vectors and with the isosurface of the delocalized electron density smoothed.

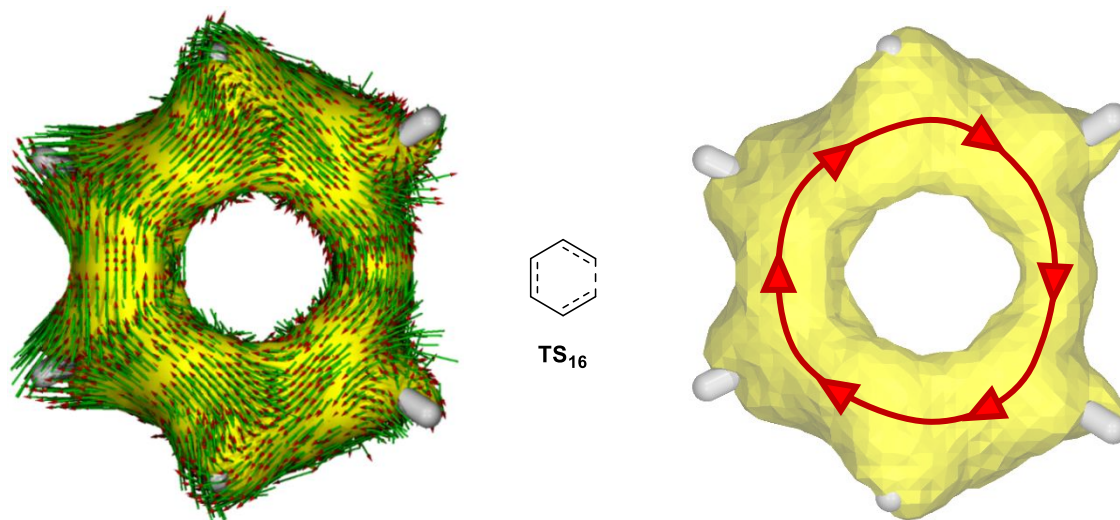
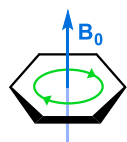


Figure 3.13. ACID plot for the transition state of **16**. Isosurface (smoothened) in yellow and vectors in green, with red arrowheads. Qualitative representation of the observed pattern in the current density vectors on the right (it is only an illustration, it does not correspond to the sum of the vectors).

At first glance, the resulting Figure 3.13 can be a bit confusing, but a circular pattern can be observed in the vectors. In this case, a clockwise pattern is detected. This pattern follows the left hand rule illustrated on the left since the magnetic field was applied coming out of the screen. Because of this, we can affirm that the transition state is aromatic.



Next, we applied the same methodology to the transition states of **E-20** and **Z-20** (Figure 3.14). Since the difference in activation energy of both substrates is very small ($\Delta G^\ddagger = 3.9$ kcal/mol), we also expect very similar ACID plots.

In Figure 3.14, underneath the two-dimensional representation of the transition states, the isosurfaces of the delocalized electron density are displayed. The only appreciable difference between them is the small density decrease that can be observed in the forming bond for the *Z*-transition state. They are both very similar to the isosurface obtained for the pericyclic transition state of **16**.

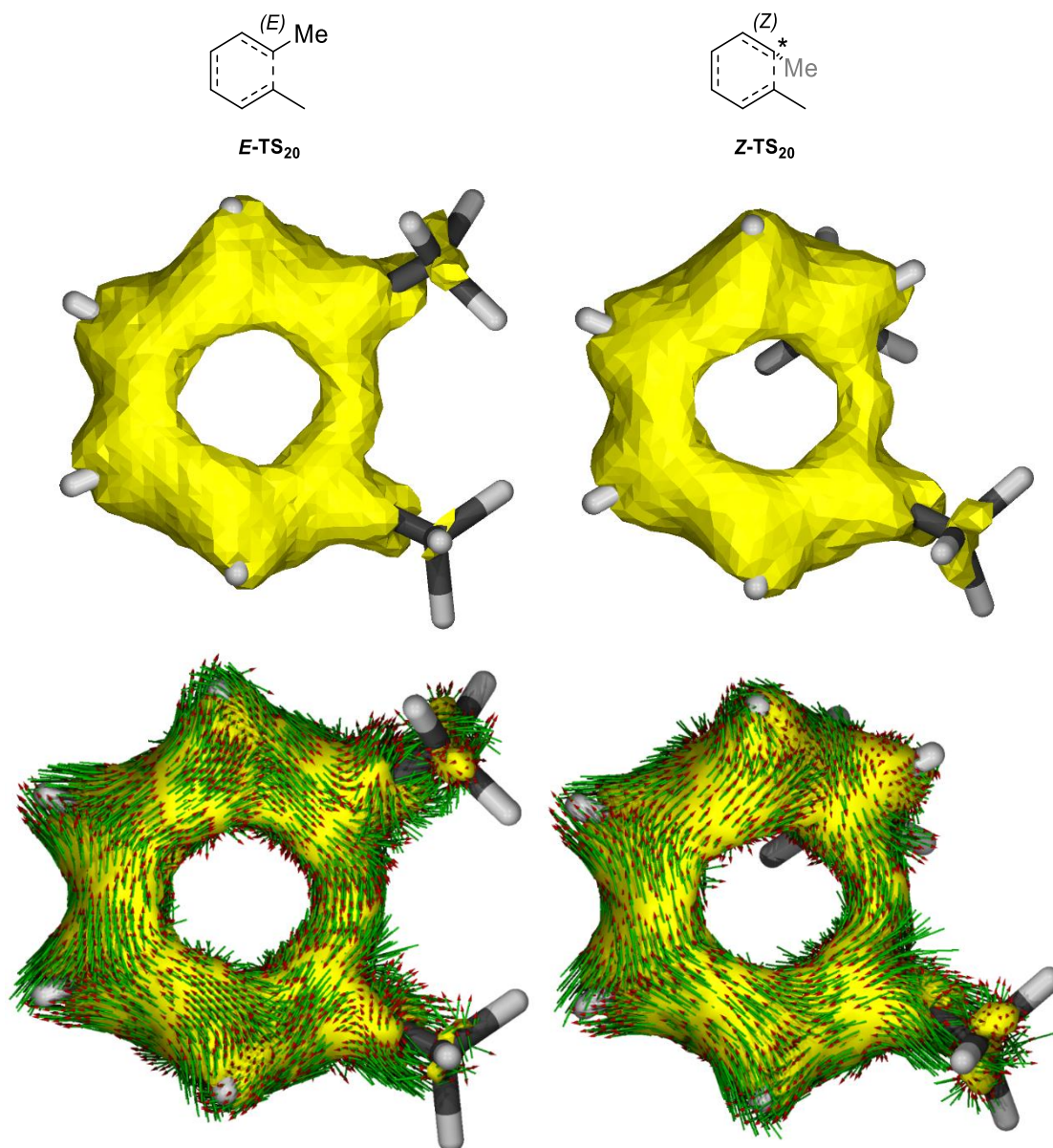


Figure 3.14. ACID isosurface plot of the delocalized electron density (middle) and isosurface and vectors (bottom) of transition states of **E-20** (left) and **Z-20** (right).

The obtained representation of the vectors of **E-TS₂₀** (bottom left, Figure 3.14) shows a clear clockwise pattern, almost identical to that of the pericyclic reaction of **16**. The vectors of the Z-transition state, **Z-TS₂₀** (bottom right, Figure 3.14), also present a clockwise cyclic pattern, although there seems to be some kind of distortion around the carbon atom labeled with a star, indicating a partial loss of aromaticity. Nevertheless, we can conclude that the mechanism of the cyclization of **20** (both *E* and *Z*-isomers) is pericyclic.

We also performed ACID calculations on the *E* and *Z*-transition states of **21**, where the hexatriene contains a methoxy functional group. The obtained plots were almost identical to those of transition states **E-TS₂₀** and **Z-TS₂₀**; therefore, their mechanism was considered pericyclic (ACID pictures available in the appendix).

Next, we performed ACID calculations on the transition states of imine **22**. As explained in the introduction, if the reaction was pseudopericyclic, the participating orbitals would be a π -orbital and an orthogonal orbital (in our study case, the lone pair of nitrogen atom). Because of this, the cyclic array of π -orbitals would be discontinued, and therefore the electron delocalization would be stopped at the point where those two orbitals interact. In the ACID pictures, this should translate into a disconnection if the electron delocalization surface.

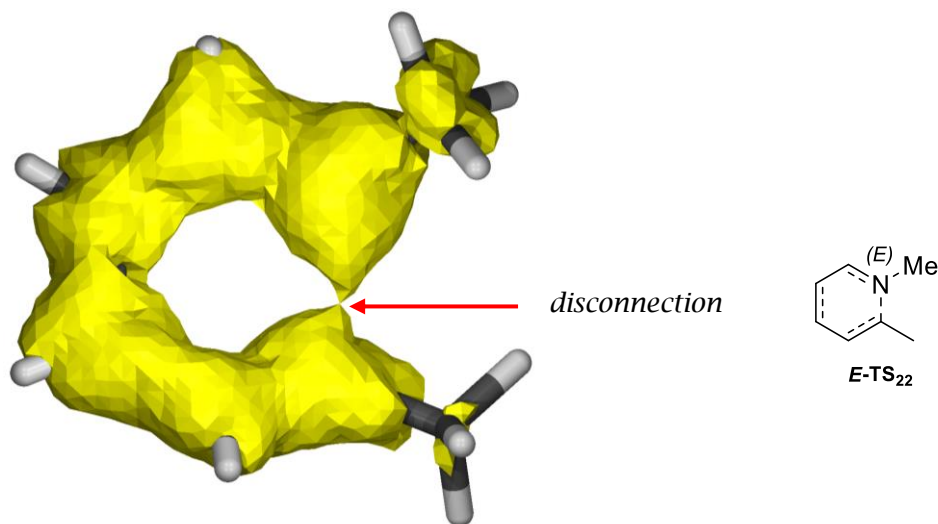


Figure 3.15. ACID plot of the isosurface of $E\text{-TS}_{22}$.

Satisfyingly, a clear disconnection was found in $E\text{-TS}_{22}$ (Figure 3.15). The isosurface between the N1 and C6 atoms shrinks around the middle, interrupting the delocalized electron density. This concurs with our hypothesis the lone pair of the nitrogen being active during the transition state. We also plotted the current density vectors on the surface, as shown in Figure 3.16.

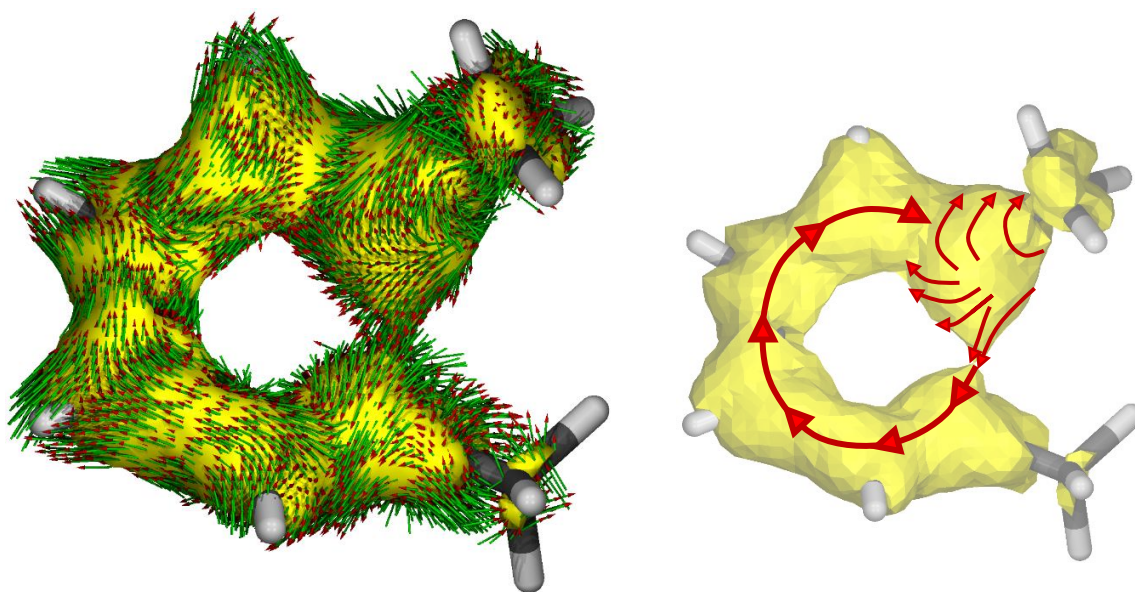


Figure 3.16. ACID isosurface plot and vectors of $E\text{-TS}_{22}$ (left) and visual representation of the pattern observed in the vectors (right).

Although the circular pattern of the vectors seems to be disrupted around the nitrogen, a few vectors can still be seen from the N1 to the C6 bond. We presume that this small density current is responsible for the aromaticity detected during the NICS study.

We turned our attention to the *Z*-isomer of this transition state, **Z-TS₂₂**. The NICS indexes suggested that the mechanism of this reaction is that of a normal pericyclic reaction; thus, we expected to visualize the delocalized electronic density through the whole molecule, without any disconnection. Gratifyingly, that was the case, as no disconnection can be observed in the isosurface of the delocalized electron density (left, Figure 3.17). The current density vector of **Z-TS₂₂** are similar to the previous *Z*-transition states, except for the bigger distortion around the N1 atom (right, Figure 3.17).

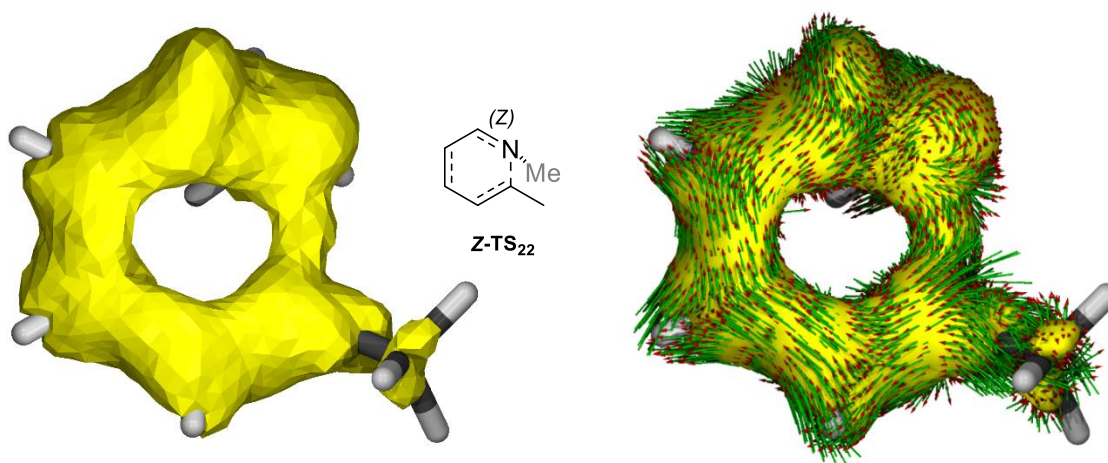


Figure 3.17. ACID plot of the isosurface (left) and isosurface plus vectors (right) of **Z-TS₂₂**.

The same procedures were applied to the transition states of oxime **23**. The obtained ACID surface of the electron density of transition state **E-TS₂₃** (left, Figure 3.18) showed no disconnection, as opposition to imine **E-TS₂₂**. Nevertheless, a narrowing in the density can be observed at the point where the disconnection of the N1-C6 bond was detected in the imine. The direction of the vectors is similar to that of **E-TS₂₂**, except for the higher vector density through the N1-C6 bond.

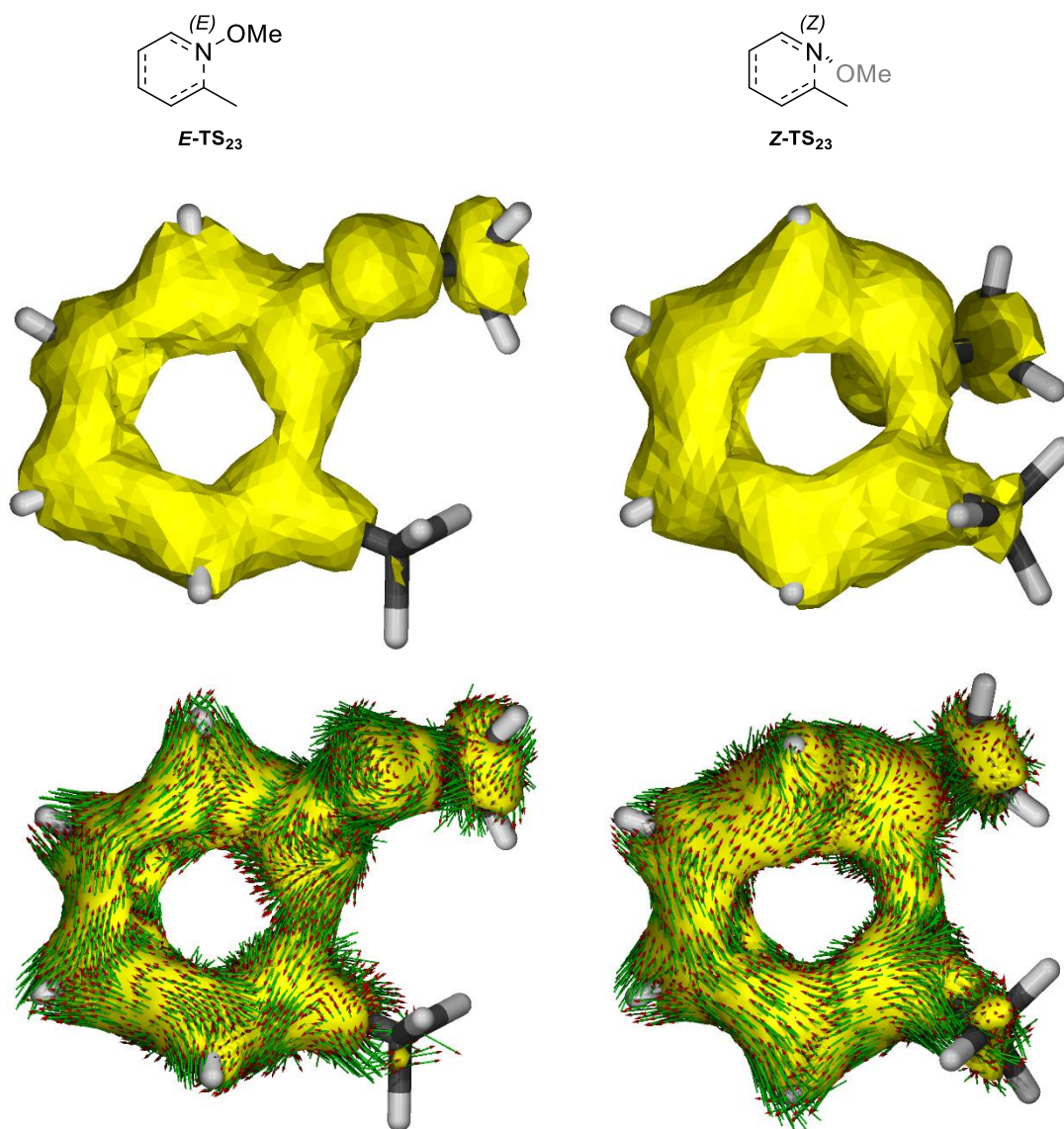


Figure 3.18. ACID plotted isosurface of the delocalized electron density (middle) and isosurface and vectors (bottom) of transition states of **E-23** (left) and **Z-23** (right).

The transition state of the Z -oxime, **Z-TS₂₃** (right, Figure 3.18), is very similar to that of imine **Z-22**. The delocalized electron density can be observed through the C1-N6 bond, while the same distortion in the direction of the vectors is present at the nitrogen atom.

From the results of the ACID calculations, it is not perfectly clear whether the reaction of the E and Z -isomers of imine **22** and oxime ether **23** can be classified as pseudo-pericyclic or pericyclic. For a discussion on the matter, see conclusions.

We also applied this methodology to one of the experimentally studied oxime ethers, **3k**, in order to verify the adequacy of our model systems. The results were almost identical to those of our model oxime **23** and are available in the appendix.

3.4 Conclusions

Two of the most commonly used criteria used to identify a pseudopericyclic reaction are the planarity of the transition state and the extremely low (or non-existent) activation barrier. If we take into account the orbitals participating in the reaction, these two phenomena occur due to the orthogonality of both orbitals. Transition states are completely planar because no rotation of the terminal atoms is needed for the orbitals to interact (Figure 3.19).

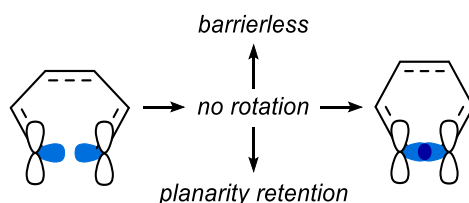


Figure 3.19. Orbital representation of a pseudopericyclic reaction with two orthogonal orbitals.

Nevertheless, the definition used for the description of the pseudopericyclic reaction, by Lemaire, states “A pseudopericyclic reaction is a concerted transformation whose primary changes in bonding encompass a cyclic array of atoms, at one (or more) of which nonbonding and bonding atomic orbitals exchange their roles”. In the transition state showed above, both of the orbitals are orthogonal to the cyclic array; however, a transition state with only one orthogonal orbital would still fall within the definition of pseudopericyclicity. Such reaction will not be planar nor barrierless, as a rotation of the non-orthogonal participating orbital would still be needed for a constructive orbital overlap to occur (Figure 3.20).

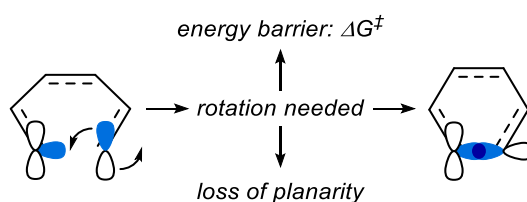


Figure 3.20. Orbital representations of a pseudopericyclic reaction with one orthogonal orbital.

Theoretically, this could be the case of the 6π -electrocyclization of imines, as one of the participating orbitals could be the lone pair of the nitrogen, while the other orbital can only be the p_z orbital of the C6 carbon. The mentioned reaction would not be planar, as C6 would have to rotate. In the same way, the reaction would not be barrierless; however, while on pericyclic reactions both terminal atoms must rotate, in this case only one of them would be rotating, which would translate into a somewhat lower energy barrier.

The results of the NICS indexes we obtained for the *E*-transition state of imine **22** were clearly in the boundary between an ordinary pericyclic reaction and the completely

pseudopericyclic reaction of **16** (which bears two orthogonal orbitals). There has been controversy of whether this mixed behavior should be considered pseudopericyclic or not (as explained in the introduction). It is our belief that the NICS indexes and the clear disconnection observed in the delocalized electron density of the ACID calculations are clear signs of the reaction proceeding through a transition state equivalent to that of Figure 3.20, and thus being pseudopericyclic.

On the other hand, the results of the *E*-transition state of oxime **23** are not so obvious. ACID calculations showed no disconnection, only a slight narrowing in the electron density isosurface. The transition state was fairly more aromatic than that of **E-TS₂₂**, as proved by the NICS indexes. We therefore believe that it is more adequate to talk about pseudopericyclic character, instead of defining reactions as either pericyclic or pseudopericyclic.

Nonetheless, it is evident that the mechanism for *E* and *Z*-oximes is not the same. The results of both NICS indexes and ACID calculations show that the mechanism of *Z*-oximes (and *Z*-imines) are identical to those of purely pericyclic reactions.

To sum up, we consider the reaction of *E*-imines to be, in our opinion, fairly pseudopericyclic. On the other hand, *E*-oximes proceed through a pericyclic mechanism with a strong pseudopericyclic character, enough to lower the activation barrier from over 50 kcal/mol (of *Z*-oximes) to feasible barriers of *ca.* 30 kcal.

3.5 References

- (1) Woodward, R. B.; Hoffmann, R. The Conservation of Orbital Symmetry. *Angew. Chem. Int. Ed.* **1969**, *8*, 781–853.
- (2) Ross, J. A.; Seiders, R. P.; Lemal, D. M. An Extraordinarily Facile Sulfoxide Automerization. *J. Am. Chem. Soc.* **1976**, *98*, 4325–4327.
- (3) Rodríguez-Otero, J.; Cabaleiro-Lago, E. M.; Peña-Gallego, Á. Theoretical Study of the Walk Rearrangement in Perfluorotetramethyl (Dewar Thiophene) Exo-S-oxide. *Tetrahedron* **2007**, *63*, 2191–2198.
- (4) Pseudopericyclic reactions studied by Birney: (a) Birney, D. M.; Wagenseller, P. E. An *Ab Initio* Study of the Reactivity of Formylketene. Pseudopericyclic Reactions Revisited. *J. Am. Chem. Soc.* **1994**, *116*, 6262–6270. (b) Birney, D. M. Further Pseudopericyclic Reactions: An *Ab Initio* Study of the Conformations and Reactions of 5-Oxo-2,4-pentadienal and Related Molecules. *J. Org. Chem.* **1996**, *61*, 243–251. (c) Ham, S.; Birney, D. M. Imidoylketene: An *Ab Initio* Study of Its Conformations and Reactions. *J. Org. Chem.* **1996**, *61*, 3962–3968. (d) Birney, D. M.; Ham, S.; Unruh, G. R. Pericyclic and Pseudopericyclic Thermal Cheletropic Decarbonylations: When Can a Pericyclic Reaction Have a Planar, Pseudopericyclic Transition State?. *J. Am. Chem. Soc.* **1997**, *119*, 4509–4517. (e) Birney, D. M.; Xu, X.; Ham, S. [1,3], [3,3], and [3,5] Sigmatropic Rearrangements of Esters Are Pseudopericyclic. *Angew. Chem. Int. Ed.* **1999**, *38*, 189–193. (f) Zhou, C.; Birney, D. M. A Density Functional Theory Study Clarifying the Reactions of Conjugated Ketenes with Formaldimine. A Plethora of Pericyclic and Pseudopericyclic Pathways. *J. Am. Chem. Soc.* **2002**, *124*, 5231–5241.
- (5) Luo, L.; Bartberger, M. D.; Dolbier, W. R. Kinetic and Computational Studies of a Novel Pseudopericyclic Electrocyclization. The First Evidence for Torquoselectivity in a 6- π System. *J. Am. Chem. Soc.* **1997**, *119*, 12366–12367.
- (6) Liu, R. C.-Y.; Luszytk, J.; McAllister, M. A.; Tidwell, T. T.; Wagner, B. D. 6-Oxocyclohexa-2,4-dienylideneketene: A Highly Reactive α -Oxoketene. *J. Am. Chem. Soc.* **1998**, *120*, 6247–6251.
- (7) (a) Fabian, W. M. F.; Bakulev, V. A.; Kappe, C. O. Pericyclic versus Pseudopericyclic 1,5-Electrocyclization of Iminodiazomethanes. An *Ab Initio* and Density Functional Theory Study. *J. Org. Chem.* **1998**, *63*, 5801–5805. (b) Fabian, W. M. F.; Kappe, C. O.; Bakulev, V. A. *Ab Initio* and Density Functional Calculations on the Pericyclic vs Pseudopericyclic Mode of Conjugated Nitrile Ylide 1,5-Electrocyclizations. *J. Org. Chem.* **2000**, *65*, 47–53.
- (8) Alajarín, M.; Vidal, A.; Sánchez-Andrada, P.; Tovar, F.; Ochoa, G. Conversion of *N*-Acyl-4-Acyloxy- β -Lactams into 1,3-Oxazin-6-Ones: Two Consecutive Pseudopericyclic Processes. *Org. Lett.* **2000**, *2*, 965–968.
- (9) (a) Rodríguez-Otero, J.; Cabaleiro-Lago, E. Electrocyclization of (*Z*)-1,2,4,6-Heptatetraene and Its Heterosubstituted Analogues: Pericyclic or Pseudopericyclic? *Angew. Chem. Int. Ed.* **2002**, *41*, 1147–1150. (b) Rodríguez-Otero, J.; Cabaleiro-Lago, E. M. Criteria for the Elucidation of the Pseudopericyclic Character of the Cyclization of (*Z*)-1,2,4,6-Heptatetraene and Its Heterosubstituted Analogues: Magnetic Properties and Natural Bond Orbital Analysis. *Chem. Eur. J.* **2003**, *9*, 1837–1843. (c) Cabaleiro-Lago, E. M.; Rodríguez-Otero, J.; Varela-Varela, S. M.; Peña-Gallego, A.; Hermida-Ramón, J. M. Are Electrocyclization Reactions of (3*Z*)-1,3,5-Hexatrienone

- and Nitrogen Derivatives Pseudopericyclic? A DFT Study. *J. Org. Chem.* **2005**, *70*, 3921-3928.
- (10) (a) de Lera, A. R.; Alvarez, R.; Lecea, B.; Torrado, A.; Cossío, F. P. On the Aromatic Character of Electrocyclic and Pseudopericyclic Reactions: Thermal Cyclization of (*Z*)-Hexa-2,4,5-trienals and Their Schiff Bases. *Angew. Chem. Int. Ed.* **2001**, *40*, 557-561. (b) Reply to ref. 9a: de Lera, A. R.; Cossío, F. P. Reply. *Angew. Chem. Int. Ed.* **2002**, *41*, 1150-1152. (c) López, C. S.; Faza, O. N.; Cossío, F. P.; York, D. M.; de Lera, A. R. Ellipticity: A Convenient Tool To Characterize Electrocyclic Reactions. *Chem. Eur. J.* **2005**, *11*, 1734-1738.
- (11) (a) Duncan, J. A.; Calkins, D. E. G.; Chavarha, M. Secondary Orbital Effect in the Electrocyclic Ring Closure of 7-Azahepta-1,2,4,6-tetraene—A CASSCF Molecular Orbital Study. *J. Am. Chem. Soc.* **2008**, *130*, 6740-6748. (b) Forte, L.; Lafortune, M. C.; Bierzynski, I. R.; Duncan, J. A. CASSCF Molecular Orbital Calculations Reveal a Purely Pseudopericyclic Mechanism for a [3,3] Sigmatropic Rearrangement. *J. Am. Chem. Soc.* **2010**, *132*, 2196-2201.
- (12) Chamorro, E. E.; Notario, R. Nature of Bonding in the Thermal Cyclization of (*Z*)-1,2,4,6-Heptatetraene and Its Heterosubstituted Analogues. *J. Phys. Chem. A* **2004**, *108*, 4099-4104.
- (13) Reply to ref. 12: Matito, E.; Solà, M.; Duran, M.; Poater, J. Comment on the “Nature of Bonding in the Thermal Cyclization of (*Z*)-1,2,4,6-Heptatetraene and Its Heterosubstituted Analogues.” *J. Phys. Chem. B* **2005**, *109*, 7591-7593.
- (14) Sakai, S. Criteria for Pericyclic and Pseudopericyclic Character of Electrocyclization of (*Z*)-1,2,4,6-Heptatetraene and (*Z*)-2,4,5-Hexatriene-1-imine. *Theor. Chem. Acc.* **2008**, *120*, 177-183.
- (15) Review on the topic plus further investigations: López, C. S.; Faza, O. N.; Freindorf, M.; Kraka, E.; Cremer, D. Solving the Pericyclic-Pseudopericyclic Puzzle in the Ring-Closure Reactions of 1,2,4,6-Heptatetraene Derivatives. *J. Org. Chem.* **2016**, *81*, 404-414.
- (16) Maynard, D. F.; Okamura, W. H. 6 π -Electrocyclization of 1-Azatrienes to 1,2-Dihydropyridines. *J. Org. Chem.* **1995**, *60*, 1763-1771.
- (17) Rodríguez-Otero, J. Study of the Electrocyclization of (*Z*)-Hexa-1,3,5-triene and Its Heterosubstituted Analogues Based on *Ab Initio* and DFT Calculations. *J. Org. Chem.* **1999**, *64*, 6842-6848.
- (18) Walker, M. J.; Hietbrink, B. N.; Thomas, B. E.; Nakamura, K.; Kallel, E. A.; Houk, K. N. Torquoselectivity Induced by Lone-Pair Conjugation in the Electrocyclic Reactions of 1-Azapolyenes. *J. Org. Chem.* **2001**, *66*, 6669-6672.
- (19) Schleyer, P. von R.; Maerker, C.; Dransfeld, A.; Jiao, H.; Hommes, N. J. R. van E. Nucleus-Independent Chemical Shifts: A Simple and Efficient Aromaticity Probe. *J. Am. Chem. Soc.* **1996**, *118*, 6317-6318.
- (20) Bader, R. F. W. *Atoms in Molecules: A Quantum Theory*, New Ed.; International Series of Monographs on Chemistry; Clarendon Press: Oxford, 1994.